HIGH-ENERGY GAMMA RAYS IN HEAVY-ION COLLISIONS

By

Anna Rosa Lampis

A DISSERTATION

Submitted to

Michigan State University

in partial fulfillment of the requirements

for the degree of

DOCTOR OF PHILOSOPHY

Department of Physics

1988

ABSTRACT

HIGH-ENERGY GAMMA RAYS IN HEAVY-ION COLLISIONS

By

Anna Rosa Lampis

The production of high-energy gamma rays ($E_\gamma > 20$ MeV) in intermediate-energy heavy-ion collisions was studied in the following reactions: N + C, N + Zn and N + Pb for beam energies of E/A=20, 30 and 40 MeV. The double differential cross sections are exponentially decreasing with energy, and the value of the inverse slope is only weakly dependent on the target mass and ranges between 8 and 14 MeV for beam energies between 20 and 40 MeV. The angular distributions are slightly forward peaked and can be associated with an isotropic emission in a frame moving with velocity close to the nucleon-nucleon center of mass velocity.

The coincidence between light fragments (^{1}H, ^{2}H, ^{3}H) and high-energy gamma-rays in the reaction N + Zn at E/A=40 MeV was studied to investigate the impact-parameter dependence of the high-energy gamma-ray production. Energy spectra and angular distributions of protons in coincidence with gamma rays were found to be very similar to those of inclusive measurements. The ratio of the coincidence cross-section to the product of the singles cross sections as a function of both proton

and gamma-ray energy and angle was found to be fairly constant with an average value of 0.6 $barn^{-1}$. A comparison between the charged-particle multiplicity associated with the emission of a gamma-ray and the charged-particle multiplicity associated with the emission of a charged-particle does not indicate any substantial difference in the impact parameter dependence of the two processes.

With two Monte Carlo codes we simulated the gamma-ray production respectively as a product of first chance n-p collision and as a product of secondary collisions. The ratios calculated with the first model decrease slowly with energy, showing an anticorrelation in the energy of the two particles as a consequence of the limited energy available in the interaction. Such a limitation is removed in the second model which offers a better agreement with the experimental results and suggests that gamma-ray emission might not be limited to first n-p collision.

ACKNOWLEDGEMENTS

I wish to thank Prof. John Stevenson, my research advisor, for his guidance and support during the last two years of my graduate career. The helpful suggestions and patience at the weekly meetings to discuss the status of my research are gratefully acknowledged.

Many thanks go to Prof. Walter Benenson for providing critical comments on the content of this thesis and to Prof. George Bertsch for the many helpful discussion on the results of the coincidence experiment.

To Dr. Robin Smith I am indebted for answering my endless questions about experimental physics. His friendship made long hours of data analysis not only bearable but pleasant.

Appreciation is extended to Dr. Dan Fox for taking care of the electronics set-up of the charged-particle detectors for the coincidence experiment and to Ken Wilson for his work on the analysis of the charged particle detector calibration data.

The help provided by Dr. John Winfield on the road to understanding and modifying pieces of the data analysis software was greatly appreciated.

It is with deep gratitude that I wish to thank my husband, Jon Slaughter, for it is his love and understanding that sustained me during

the difficult moments of this enterprise. His critical comments and careful reading of the thesis were most welcomed and appreciated.

Many hearty thanks go to my office-mates Wen Tsae Chou and Mary Wilson, to Silvana Angius and Aldo Bonasera. Their friendship made long hours of work more pleasant and their help solved many practical problems.

Last but surely not least, I would like to thank my parents, for their constant love and support were never diminished by the distance. A special thanks goes to my mother: her beliefs in the value of higher education and self-discipline were instrumental in my education.

TABLE OF CONTENTS

LIST OF TABLES

LIST OF FIGURES

INTRODUCTION

A. MOTIVATION

In 1982 Budiansky et al.[Bu 82] studied at Berkeley, 40-500 MeV gamma rays emitted in 2 GeV/nucl. collisions of Ne and Ar with Ca and Pb targets. The production of gamma rays by nucleus-nucleus bremmstrahlung was suggested to explain the deviation of the experimental spectra from the spectra expected by adding the contributions of the decays of particles like π_o, η and Δ.

High-energy gamma rays ($E_\gamma > 20$ MeV) in intermediate energy heavy ion reactions were observed for the first time in 1984 by two independent experimental groups. Grosse et al. [Gr 85] at GSI observed large yields of single gamma rays while studying neutral pion production with a lead-glass detector. Beard et al. [Be 86] at MSU were puzzled by the large number of positrons and electrons present in a charged pion experiment until they found that the leptonic background was associated with the pair conversion of gamma rays in the collimator of the pion spectrometer.

From a theoretical view point, in heavy ion physics, gamma rays were first suggested by Eisberg et al. [Ei 60] in 1960 as a tool to distinguish between compound nucleus reactions and direct interactions. The gamma-ray spectrum was expected to be sensitive to the time delay between the cessation of the current associated with the incident particle and the initiation of the current associated with the product particle. Theoretical predictions were made although only for photons

the wavelength of which is large compared to the nuclear radii and hence for energies lower than the ones of interest here.

J. I. Kapusta [Ka 77], in an article published in 1977, used the fireball model [We 76] to study the nucleus-nucleus bremsstrahlung mechanism for the production of high-energy gamma rays with energies below 10 MeV. In the same paper he suggested studying gamma rays in the energy range between 10 and 140 MeV.

In 1985 D. Vasak et al. [Va 85] proposed a nucleus-nucleus bremsstrahlung model for gamma rays above 10 MeV. Such a mechanism, if found to reproduce the experimental data, would be able to supply information about the dynamics of the collision and about physical quantities such as the deceleration time and the compressibility of nuclear matter.

The aim of this thesis is to contribute to the determination of the characteristics of the high-energy gamma-ray yield and to try, through the analysis of a coincidence experiment between photons and protons, to obtain information about the high-energy gamma-ray production mechanism.

B. THESIS ORGANIZATION.

Chapter I contains inclusive double differential cross sections, angular distributions and rapidity plots for high-energy gamma rays emitted in the nine reactions: N + Pb, Zn and C at E/A=20, 30 and 40 MeV. Details of the experimental setup, detector calibration, electronics and data reduction are also included.

Chapter II contains a comparison with experimental results obtained by other groups and a brief outline of the theories proposed to interpret the experimental results.

In chapter III is a description of the experimental setup, electronics, data reduction and detector calibration for a coincidence experiment between high-energy gamma rays and protons in the reaction N + Zn at E/A=40 MeV. The results include a qualitative comparison between inclusive proton spectra and exclusive spectra of protons in coincidence with high-energy gamma rays. The same comparison is also presented for gamma-ray spectra. The ratio of the gamma ray - proton coincidence cross section to the product of the single proton and gamma ray cross sections is studied as a function of proton angle, gamma-ray angle (only 60° and 120°), gamma-ray energy and proton energy. Multiplicity histograms for protons and protons in coincidence with gamma rays are also included in this chapter.

In chapter IV the results of the coincidence experiment are discussed and compared with the results of a Monte Carlo calculation based on a n-p bremsstrahlung model and on a thermal model.

A summary and conclusions end this thesis.

CHAPTER I

HIGH-ENERGY GAMMA RAYS

A. EXPERIMENTAL SET-UP

After a short test run produced promising results [Be 86] a more comprehensive experiment investigating the target, angle and energy dependence of the high-energy gamma-ray emission was performed at the National Superconducting Cyclotron Laboratory. It employed a ^{14}N beam and three targets: C(34.8 mg/cm^2), Zn(33.7 mg/cm^2), and Pb(62.8 mg/cm^2). The energies used were E/A=20, 30 and 40 MeV.

Two high-energy gamma-ray detectors were positioned 50 cm from the target. The first detector (D1) was used for the most forward angles: 30, 60 and 90°. The second detector (D2) collected data at 90, 120 and 150°. Comparison of the data collected at 90° allowed a check of the relative efficiency of the two detectors.

1. High-energy gamma-ray detectors

An active CsI converter (10.2 x 10.2 x 0.3 cm for detector 1 and 10.2 x 11.4 x 0.6 cm for detector 2) was followed by a stack of eight Cherenkov elements. The Cherenkov elements (Bicron BC-480) were made of lucite ($C_5H_8O_2$) with a wave shifter for better and more uniform light collection. The first element was 1.27 cm, the second was 2.54 cm and the rest were 5.08 cm thick. All the elements had the same surface dimensions of 22.9 x 22.9 cm. The stack (Figure I-1) was enclosed with

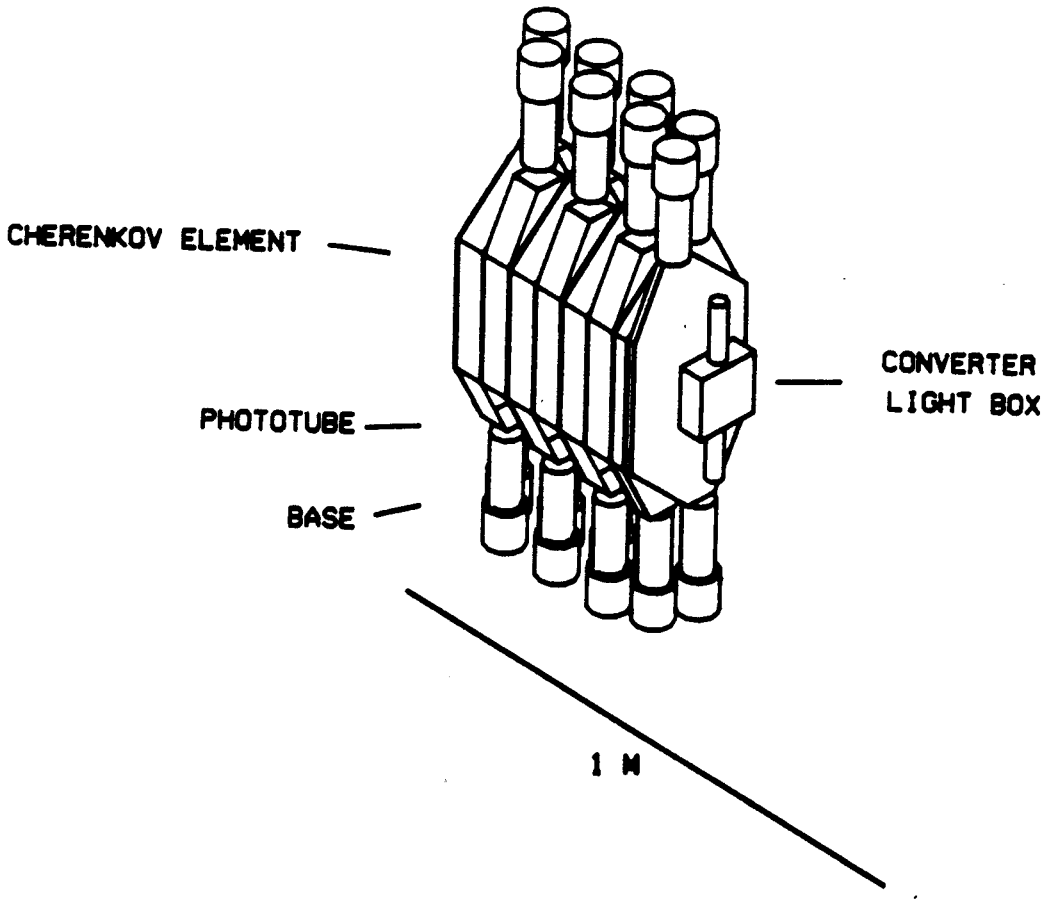

Figure I-1 High-energy gamma-ray detector.

anticoincidence shields: the sides and the top were made of plastic scintillator while the front was a plastic Cherenkov detector able to withstand higher rates of charged particles than the scintillator material. Since the surface of the crystal was not smooth enough to allow total internal reflection, each converter crystal was enclosed in a fiberglass-aluminum box painted white to allow the light to undergo many reflections before being collected by the two photomultiplier tubes at the top and the bottom of the box.

The top and the bottom of each Cherenkov element extended vertically to form light guides to converge the light towards the respective photomultiplier tube (5.04 cm Hamamatsu R329). The front shield also had two photomultiplier tubes attached to the top and the bottom through light guides. The remaining shields had only one phototube.

One 5.08 cm graphite absorber was positioned between the target and the front shield of each detector to absorb most of the charged particles produced in the reaction to reduce singles rates in the converter and in the anticoincidence shields. Protons with energies up to 100 MeV were completely stopped by the absorber reducing the rate by 99%.

B. ELECTRONICS

The master trigger for each gamma-ray detector consisted of an "and" of six signals: the two phototube signals from the converter and the two phototube signals each from the first and the second Cherenkov elements. When the conditions for the master trigger were satisfied and

the computer signal "not busy" was also present, the pulse height and the time information was recorded for each photomultiplier tube using LeCroy 2249 charge integrating ADC and LeCroy 2228 TDC's.

The timing of the master gate with respect to the cyclotron RF was also recorded.

The electronic circuit for a gamma-ray detector element is shown in Figure I-2a. This basic circuit was repeated 24 times for each detector. The master trigger circuit is shown in Figure I-2b

C. CALIBRATION

A complete analysis of the calibration results is beyond the aim of this thesis and it will be discussed elsewhere [St 88]. What follows is a brief description of the experimental technique used to calibrate the gamma-ray detectors and an explanation of how the experimental results presented here were accordingly corrected.

The calibration of a gamma-ray detector was performed with the photon-tagging spectrometer of the University of Illinois. An electron beam generated bremsstrahlung photons by interacting with a 25 μm. Al foil. The electron-beam energies used were: 99, 77, 56 and 35 MeV. These beams provided tagged photons of 74-82 Mev, 53-61 MeV, 37-43 MeV, and 17-23 MeV respectively. While the primary electron beam was deviated into a beam dump, the electron that generated the bremsstrahlung was bent through 180 degrees and detected in an array of 32 scintillator elements. By knowing which scintillator fired, the bremsstrahlung energy could be determined within about 200 KeV.

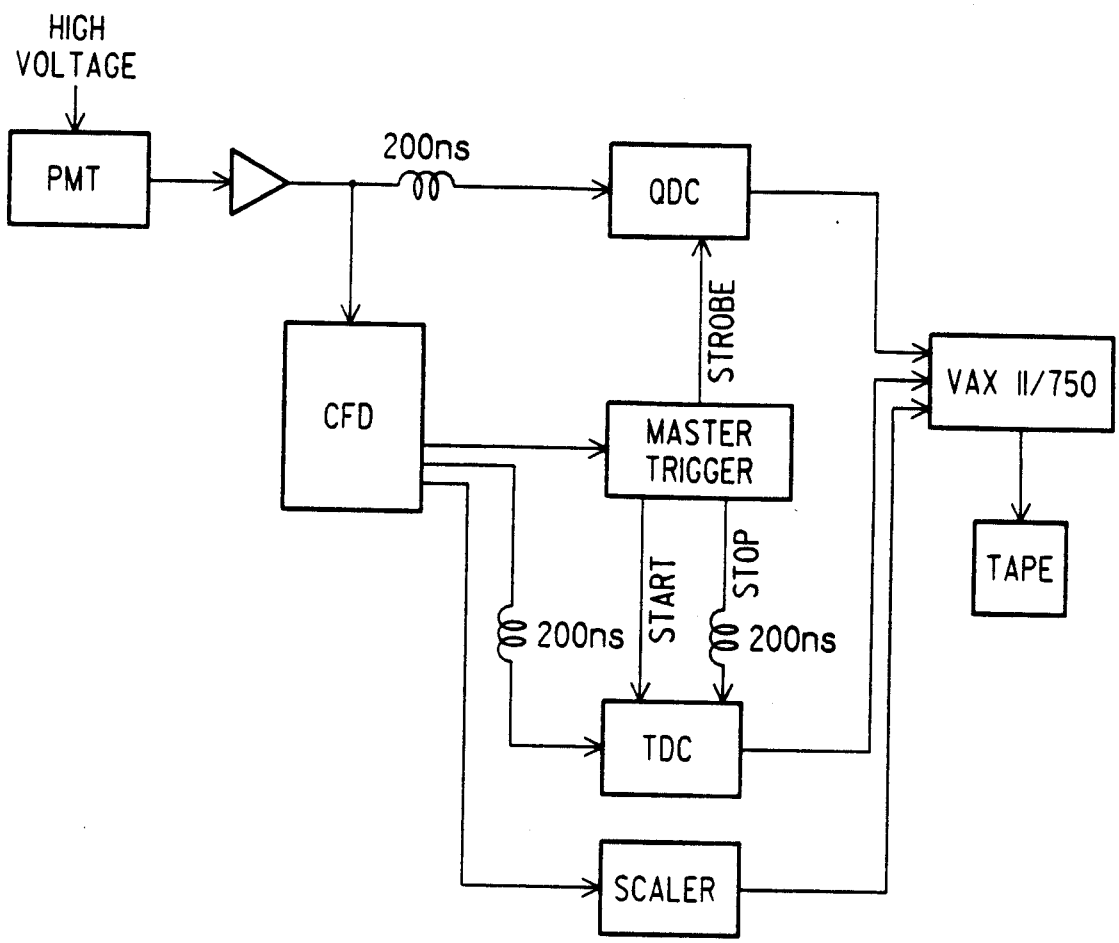

Figure I-2a Electronic circuit for a gamma-ray detector element.

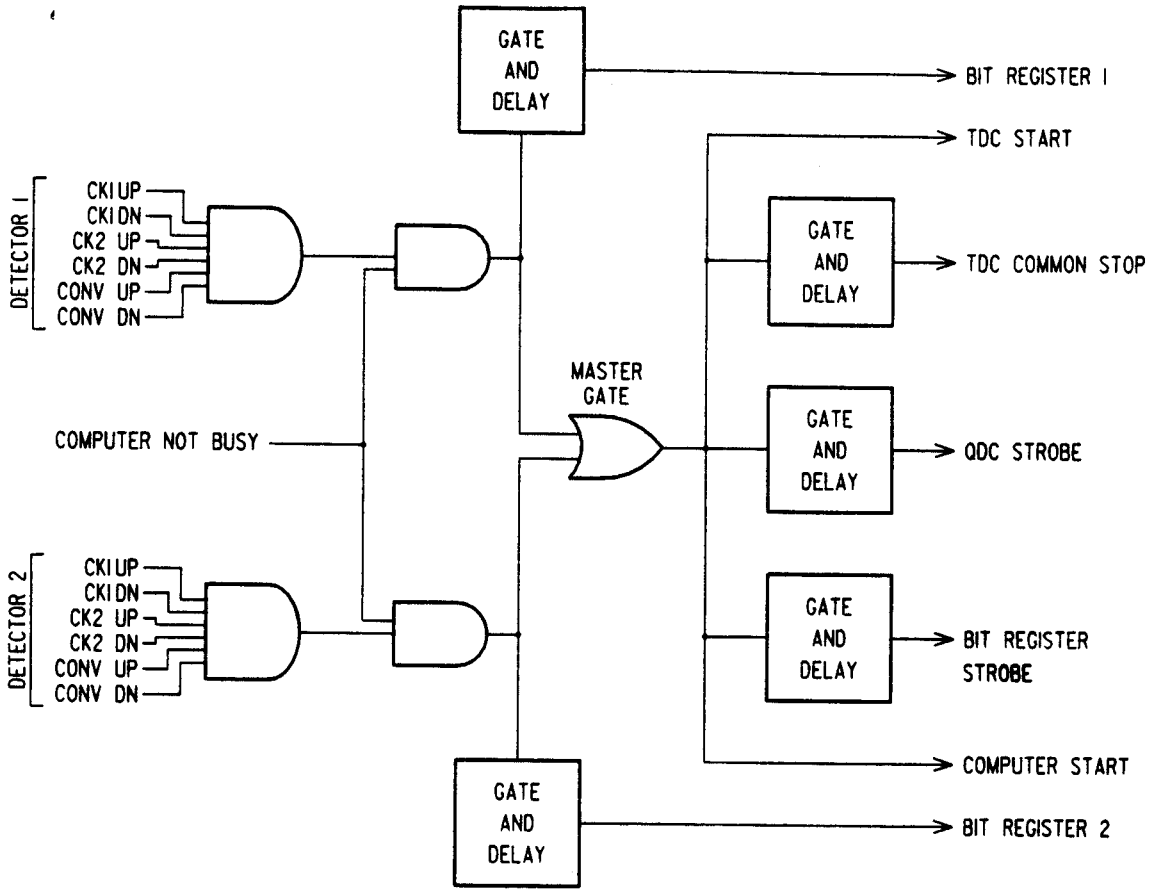

Figure I-2b Master trigger circuit.

The only difference between the gamma-ray detector calibrated at the University of Illinois and the ones used in the experiment described here is in the type of converter used: BaF_2 in the first case and CsI in the last. This difference is expected to affect only the detector efficiency determined by the pair production cross section in the converter. The absolute efficiency of the detector was measured by comparing it with the efficiency of a large cylindrical (30 cm diameter X 36 cm. length) NaI detector, provided by the University of Illinois, and assumed to be 100% efficient. We defined $\sum$ as the ratio between the number of gamma detector - tag counter coincidences and the total number of times the tag counter fired. The ratio $\sum$ can also be written as the product of the detector efficiency ε_{det} and the efficiency of the spectrometer ε_{spec}(equation I-1).

$$\text{I-1} \qquad \sum = \frac{N_{\gamma\text{-tag}}}{N_{tag}} = \varepsilon_{det}\, \varepsilon_{spec}$$

Measuring $\sum$ for both the large NaI and the Cherenkov telescope it was possible to determine the efficiency of our detector relative to the NaI (equation I-2).

$$\text{I-2} \qquad \frac{\sum_{cherenkov}}{\sum_{NaI}} = \frac{\varepsilon_{cherenkov}}{\varepsilon_{NaI}} = \varepsilon_{cherenkov}$$

since ε_{NaI} is assumed to be equal to 1

The spectrometer efficiency ε_{spec} was found to be electron-beam energy dependent varying from about 30% for the 35 MeV beam to 60% for the 99 Mev beam. It was, therefore, necessary to make a comparison with the NaI detector at each beam energy. In Figure I-3 the Cherenkov detector efficiency, as a function of photon energy, is compared to the efficiency calculated with the pair production cross section and with the Stanford electron-gamma shower code EGS4 [Ne 85]. Both calculations are in reasonable agreement with the measured efficiency.

In Figure I-4 the response function of the gamma-ray detector is presented both for the case in which the light generated by the pair in the converter is and is not taken in account to calculate the total gamma-ray energy. The addition of the energy loss in the converter yields a good agreement between the calculated and the bremsstrahlung photon energy. Since in the experiment described here the energy loss in the converter was not considered, all the energy spectra had to be corrected to account for it. The corrected spectra were found to be still exponential with an unchanged slope but the magnitude of the yield was found to increase by a factor ranging from 2.0 at 40 MeV to 2.5 at 20 MeV. All the results presented in this chapter have been corrected using the multiplicative factors presented in Table I-1.

The energy resolution of the detector with and without the contribution of the energy loss in the converter is presented in Figure I-5.

D. DATA REDUCTION

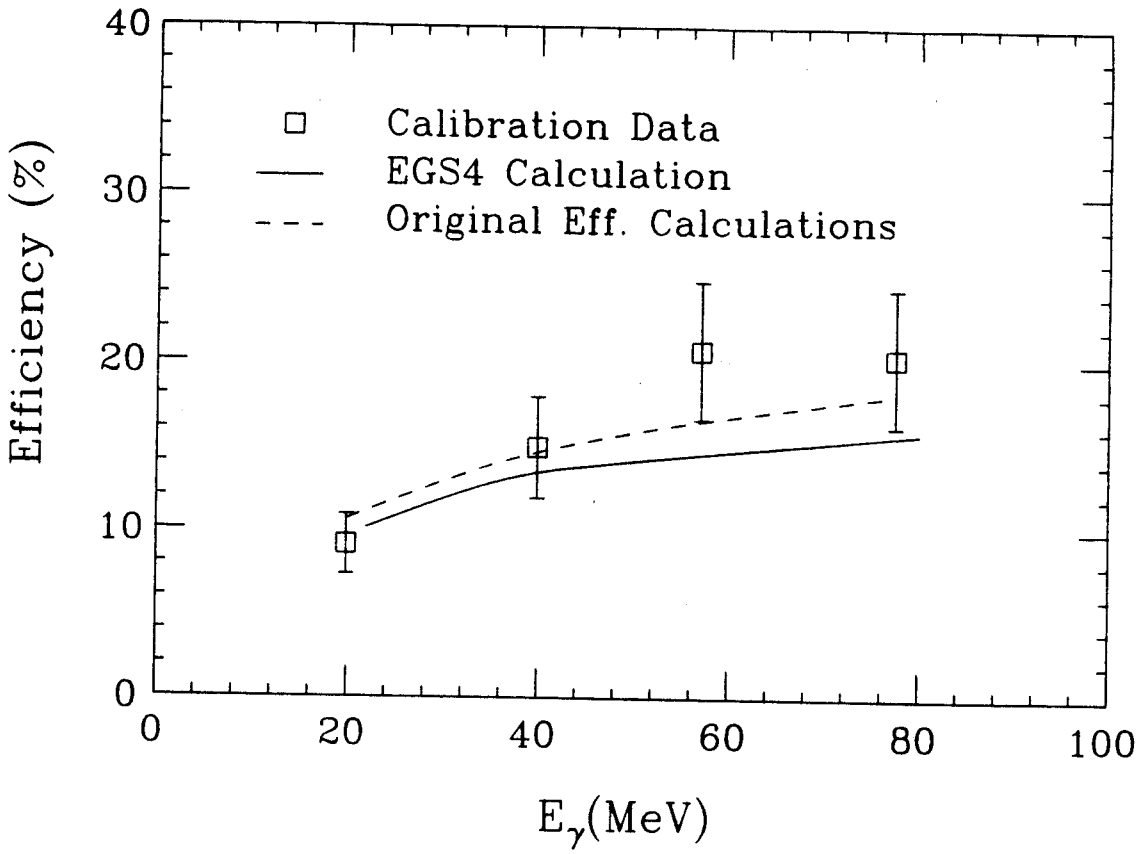

Figure I-3 Gamma-ray detector efficiency.

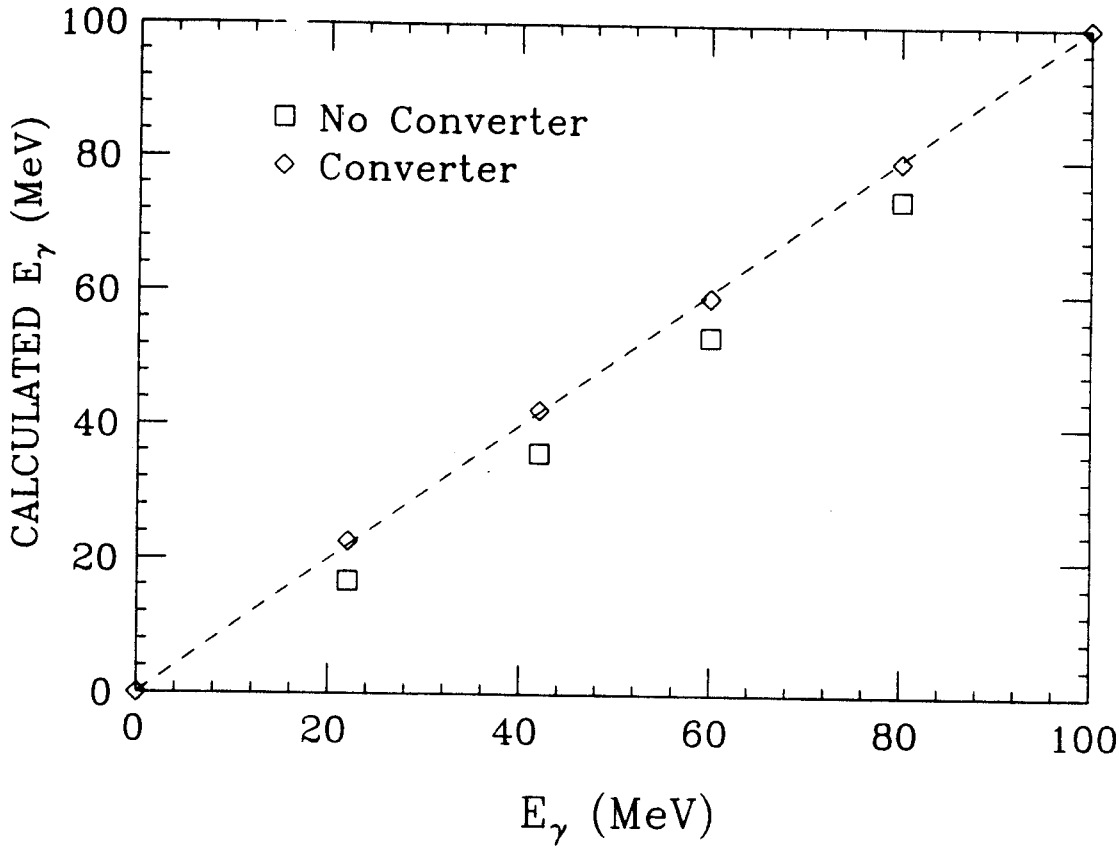

Figure I-4 Gamma-ray detector response function.

TABLE I-1 Calibration-correction factors for $\frac{d^2\sigma}{d\Omega\, dE_\gamma}$.

E/A	20 MeV	30 MeV	40 MeV
	2.5	2.2	2.0

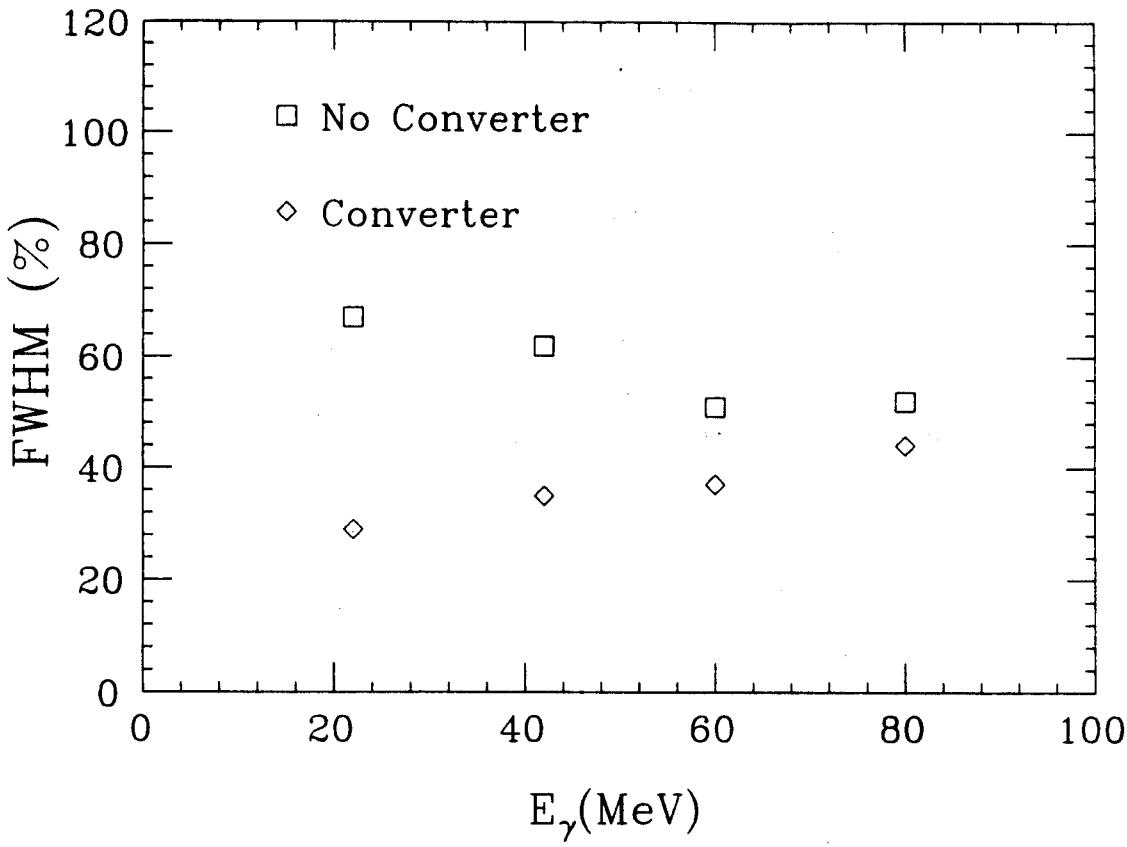

Figure I-5 Gamma-ray detector energy resolution.

The gamma-ray transmission $e^{-\mu x}$, due to the attenuation in the absorber, is 0.8418 for 20 MeV gamma rays and 0.8569 for gamma rays above 60 MeV. The average value of 0.8525 was used to correct the experimental cross-sections.

The CsI efficiency in converting a gamma ray into a positron-electron pair, which was incorporated in the cross-section calculations, varies from 12 to 25% for gamma rays in the 20-120 MeV range [Be 86]. In this range both Compton scattering and photoelectric effect are negligible (Figure I-6).

The comparatively larger area of the Cherenkov elements with respect to the converter dimensions allows for multiple scattering of the electrons and positrons. The response of each single Cherenkov element was equalized using cosmic muons passing through the detector in straight lines from front to back. This condition was achieved by requiring a signal to be present both in the converter and in a plastic scintillator located after the last Cherenkov element.

The light generated by each component of the pair in each element is proportional to the distance the particle traveled in the element. Using energy-range (Figure I-7) relations it was possible to reconstruct the gamma-ray energy as the sum of the energy of the electron-positron pair.

$$E_\gamma = \sum_{l=0}^{8} (\text{light})_l \, \Delta E_l \qquad \text{I-3}$$

The quantity $(\text{light})_l$ is the average of the Cherenkov light collected by the two opposite photomultiplier tubes of the detector element l divided

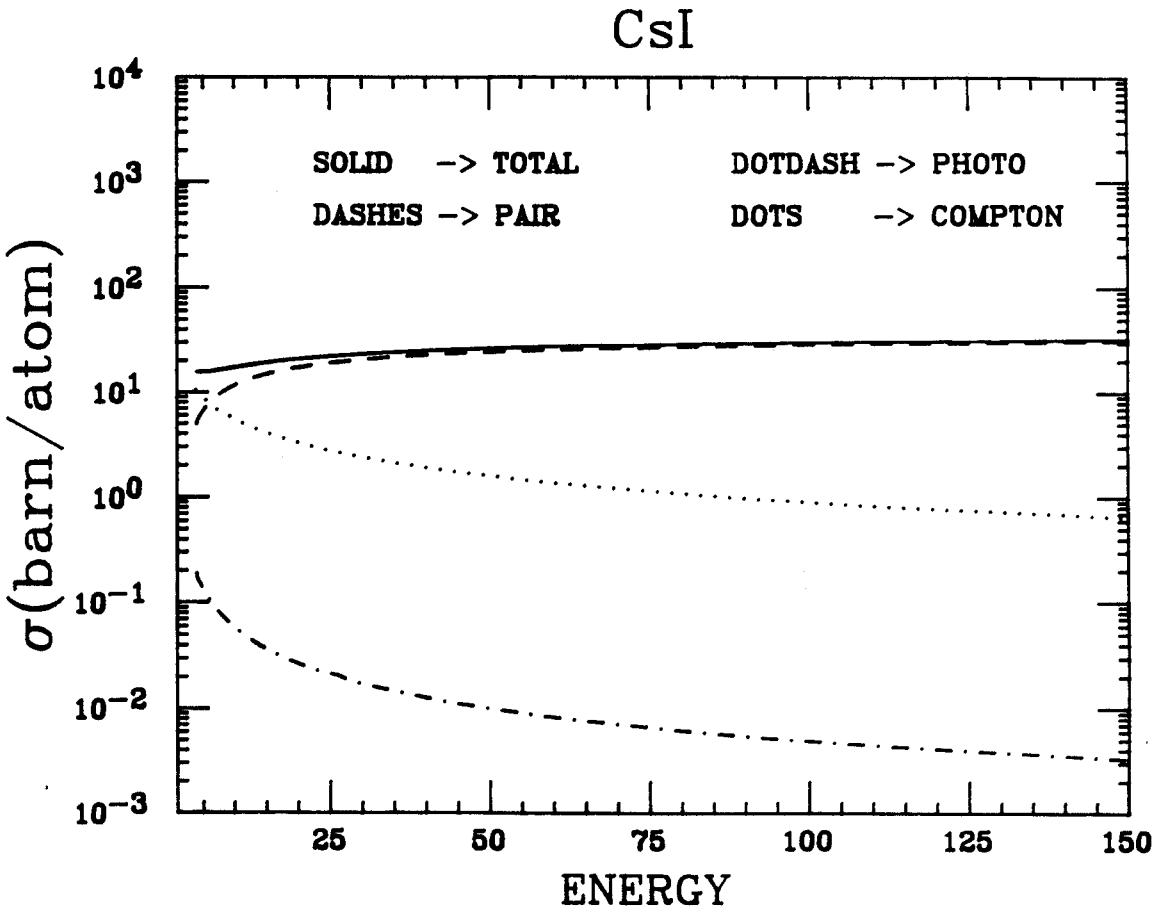

Figure I-6 Compton scattering, photoelectric effect and pair production for CsI

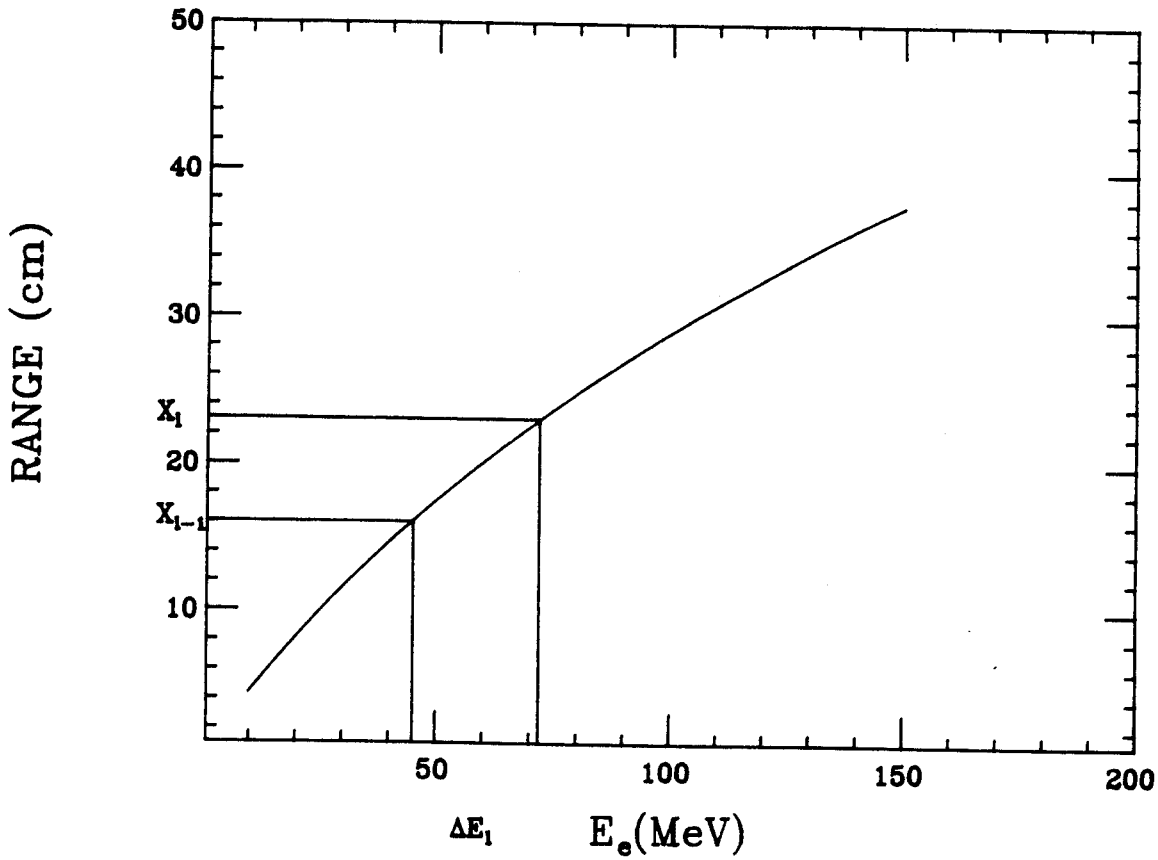

Figure I-7 Energy-range correlation for electrons in lucite ($C_5H_8O_2$).

by the amount of light characteristic of an electron passing through that element. ΔE_l is the energy related to an increment in range equal to the difference between the detector thickness up to element l (x_l) and the detector thickness up to element l-1 (x_{l-1}) as shown in Figure I-7. As an example, (see Table I-2) if a gamma ray of 78 MeV is transformed into an electron of 56 MeV (which stops at the back of the fifth detector) and in a positron of 22 MeV (which stops at the back of the third detector) the expression in equation I-3, in an ideal case, becomes:

I-4 $$E_\gamma = \{2 \times [2.89+5.78+13.35] + 1 \times [15.60+18.08]\}\ \text{MeV} = 78\ \text{MeV}$$

since both the electron and the positron will travel through the first three elements but the electron will also travel through the fourth and the fifth elements.

The on-line triggering conditions for the acceptance of a gamma-ray event were the presence of a signal in the converter and in the first two Cherenkov elements. In the off-line analysis more restrictive conditions were added to reduce the cosmic muon contamination of the gamma-ray spectra. Since a gamma ray would not create a signal in the front plastic shield while a charged muon would, a condition rejecting all the events leaving a signal in the front plastic was applied during data analysis. Likewise, all the events passing through the top and the side shields were eliminated. When all these conditions were applied, the muon rate of about 30 counts per minute decreased to about 0.3 counts per minute. This information was obtained by applying the muon

TABLE I-2 Energy loss of an electron going through the elements of the gamma-ray detector.

Element #	Thickness (cm)	E_{front} (MeV)	E_{back} (MeV)	ΔE (MeV)
1	1.27	0.	2.89	2.89
2	2.54	2.89	8.67	5.78
3	5.08	8.67	22.02	13.35
4	5.08	22.02	37.62	15.60
5	5.08	37.62	55.70	18.08
6	5.08	55.70	76.68	20.98
7	5.08	76.68	100.9	24.22
8	5.08	100.9	129.0	28.15

rejection conditions to a muon run, in which the same triggering conditions as for a gamma-ray run where required, and observing the residual muon rate.

The flux of charged particles produced in the reaction could create a coincidence between a charged particle and a gamma ray with a subsequent elimination of the event. We measured this effect (accidentals) by looking at the adjacent RF bursts. The worst accidental rate we observed was for the lead target at 40 MeV when it reached the value of 4.1%. On average the accidental rate was 1.8% for D1 and 0.6% for D2.

Gamma rays produced by neutron capture were found to have an energy lower than 20 MeV and therefore did not represent a problem in the analysis of the data.

E. RESULTS

The double differential cross-sections taken at 30, 60, 90, 120 and 150° for the three systems and for the three energies under study are shown in Figures I-8 to I-16. The spectra are exponentially decreasing with energy, and two components can easily be discriminated. The first, for $E_\gamma < 20$ MeV, is dominated by statistical gamma rays and is much steeper than the second. When parameterized with a function of the form $ae^{-E/\tau}$, it gives an approximately constant value for the inverse slope parameter τ, of about 2 MeV. The second portion of the spectra, $E_\gamma > 35$ MeV, can be parameterized in terms of an isotropic emission from a

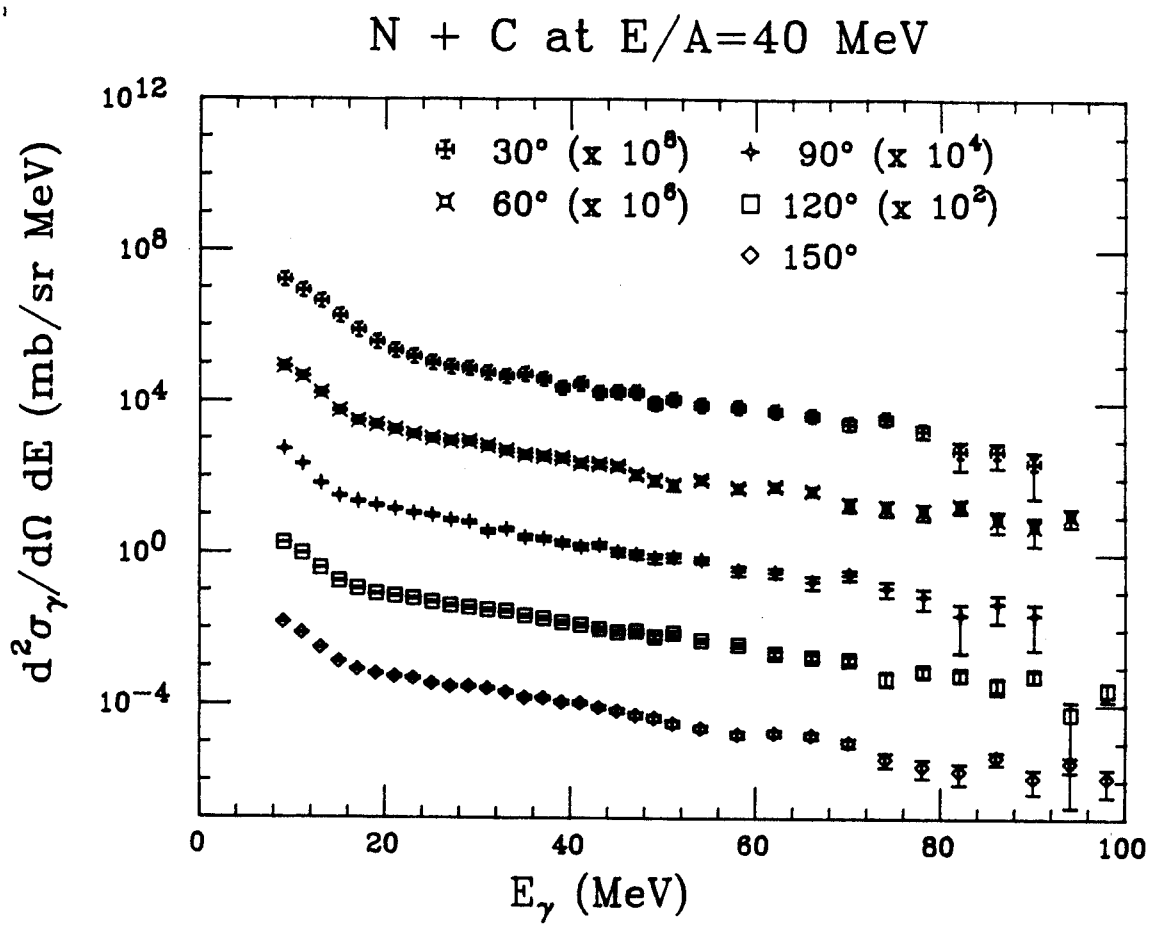

Figure I-8 Double-differential cross section N + C at E/A=40 MeV.

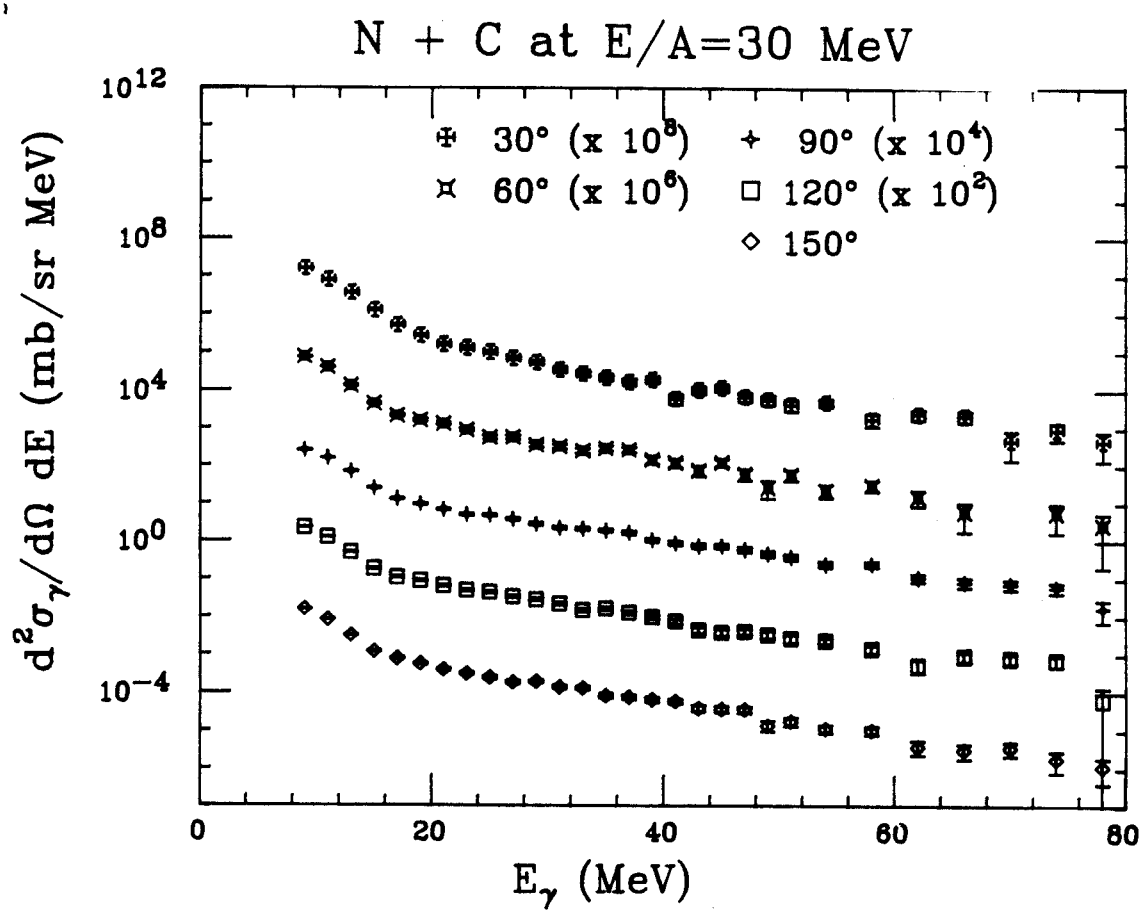

Figure I-9 Double-differential cross section N + C at E/A=30 MeV.

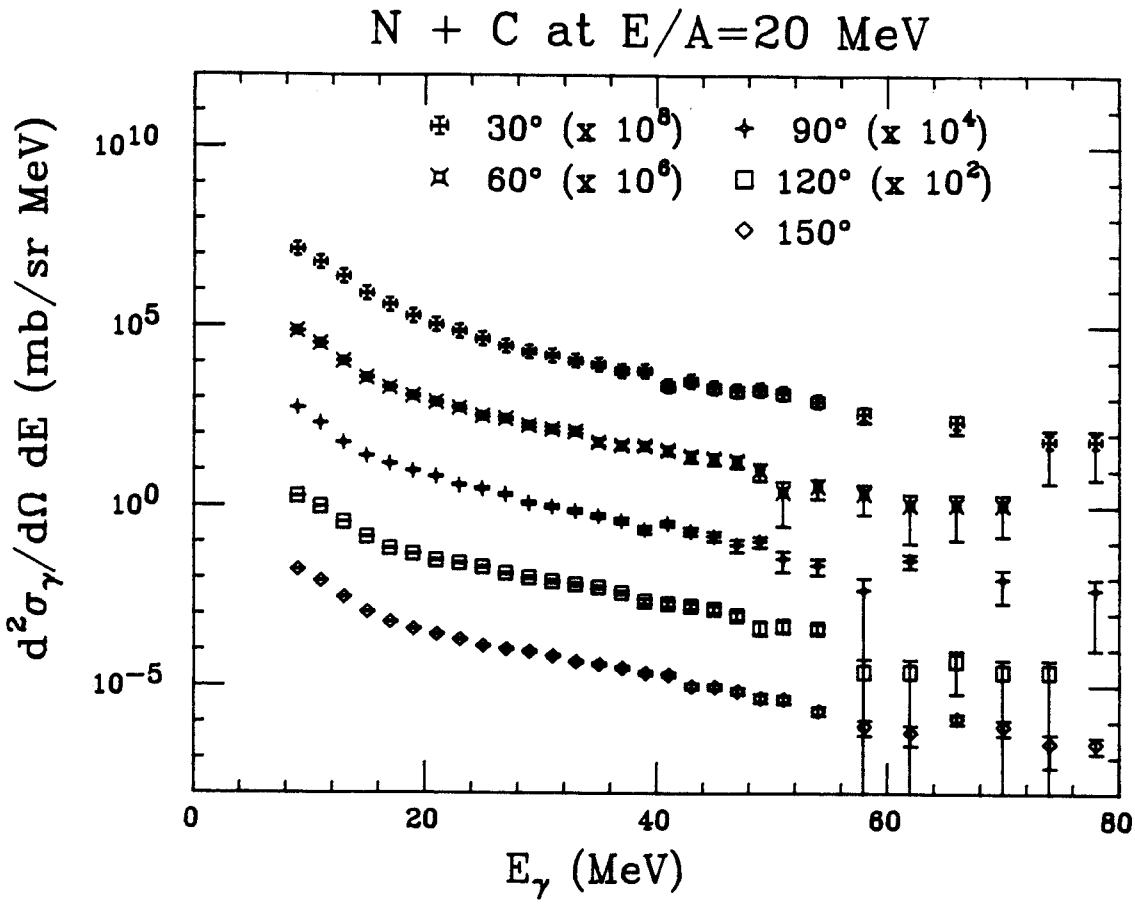

Figure I-10 Double-differential cross section N + C at E/A=20 MeV.

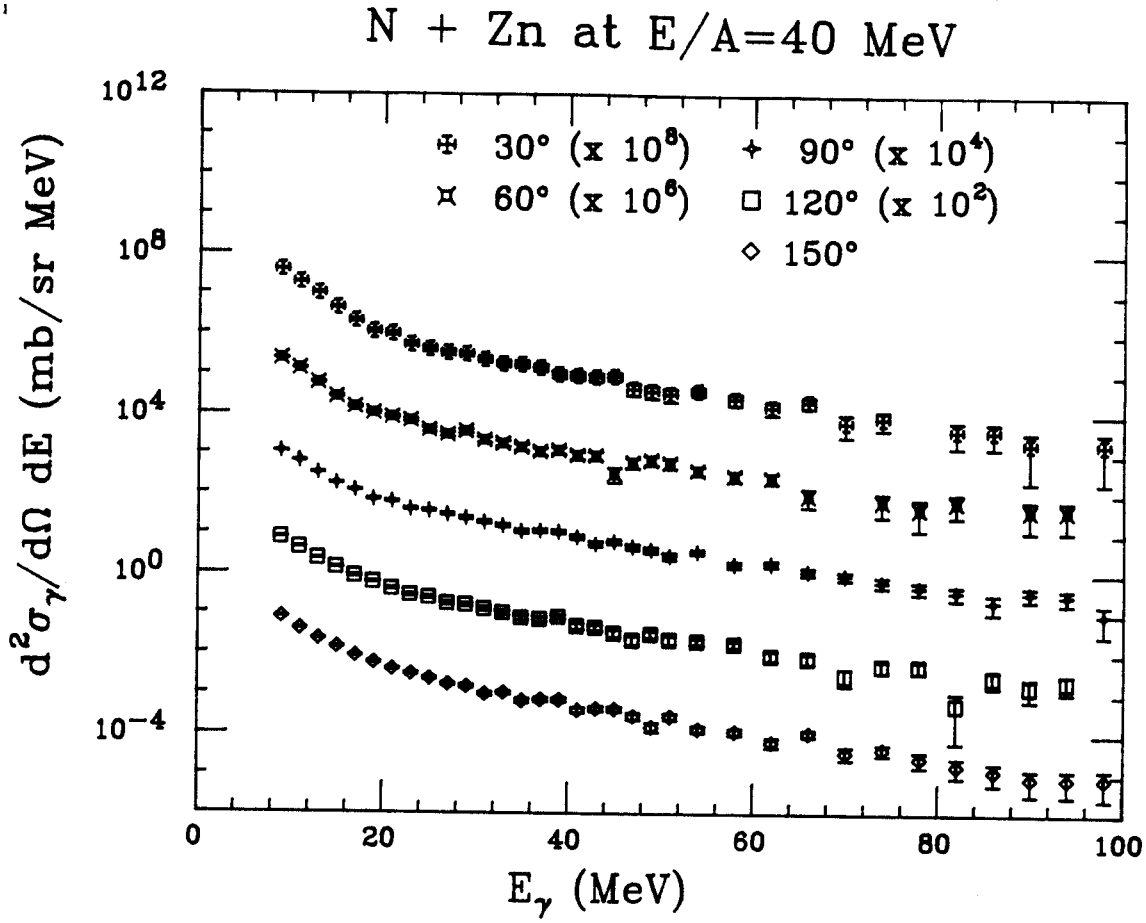

Figure I-11 Double-differential cross section N + Zn at E/A=40 MeV.

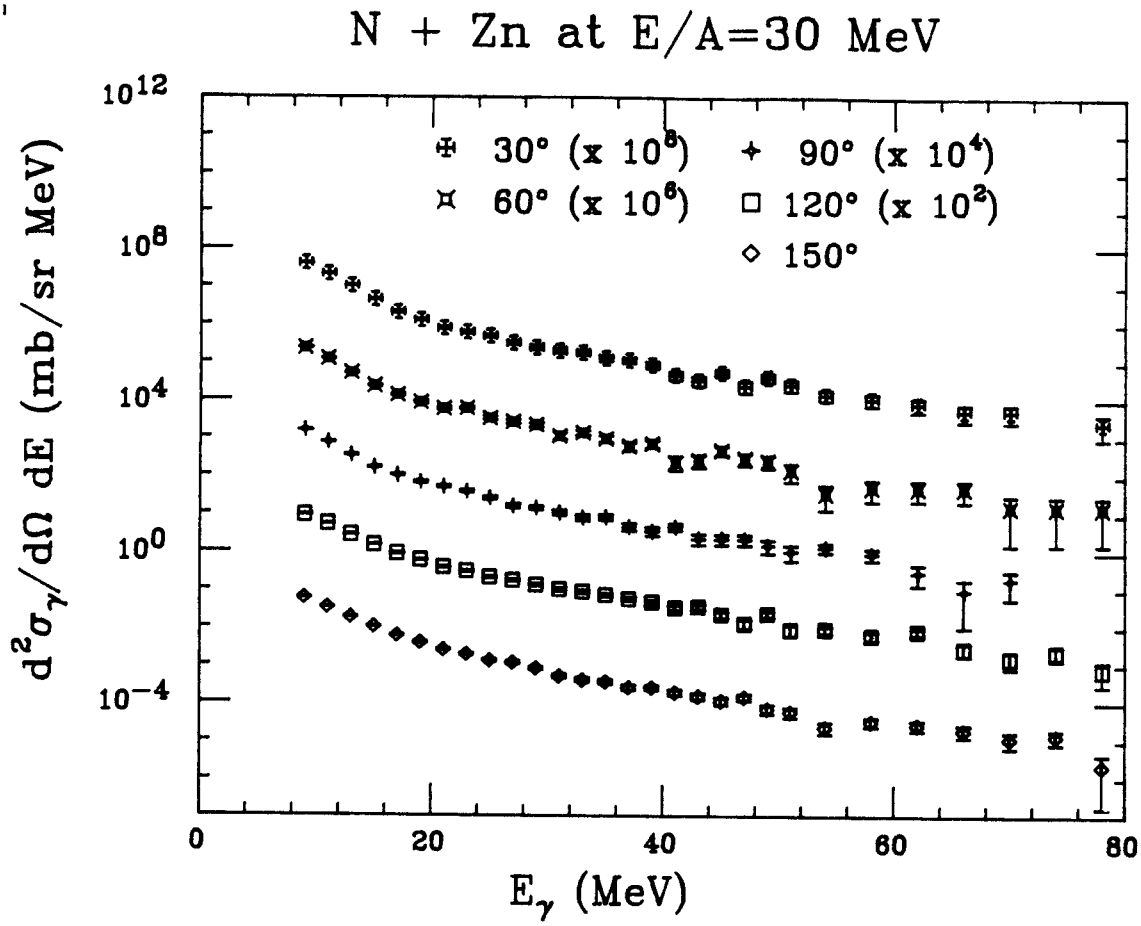

Figure I-12 Double-differential cross section N + Zn at E/A=30 MeV.

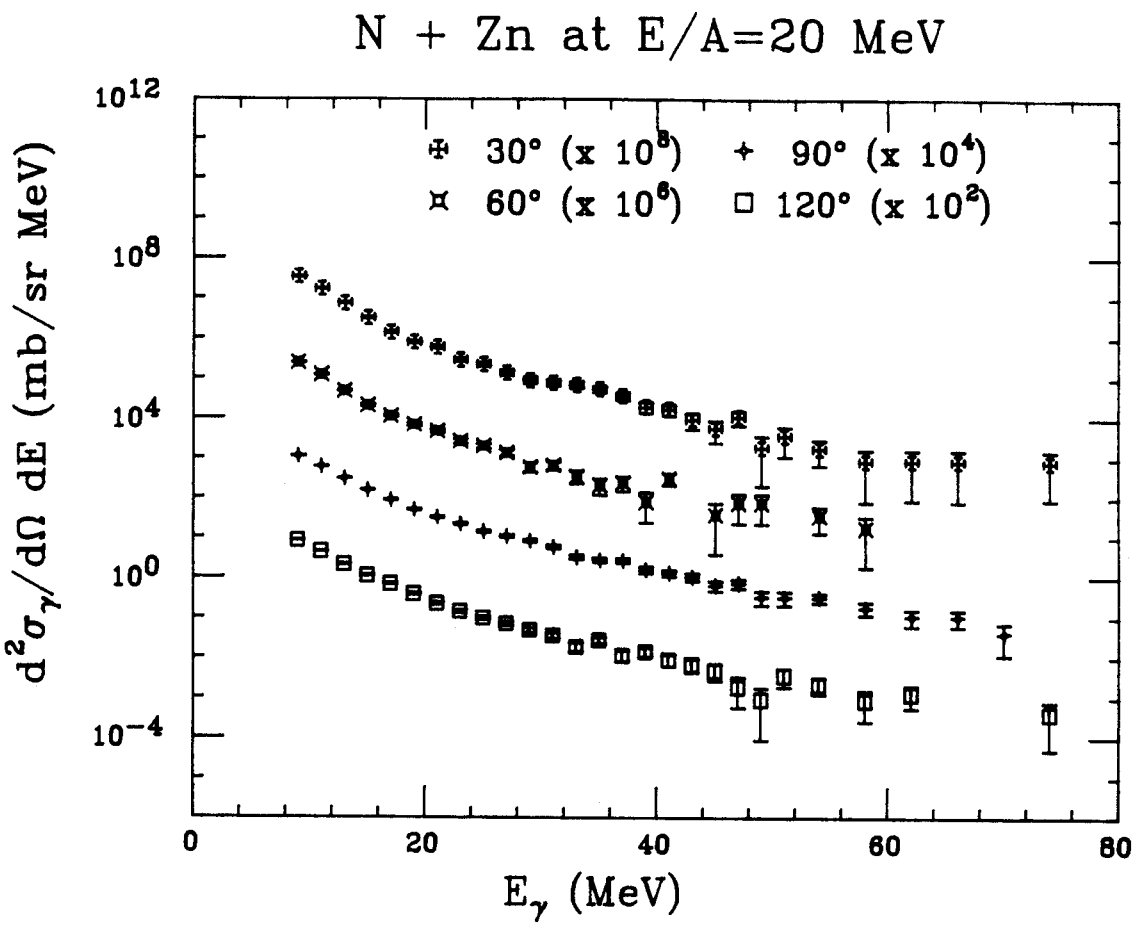

Figure I-13 Double-differential cross section N + Zn at E/A=20 MeV.

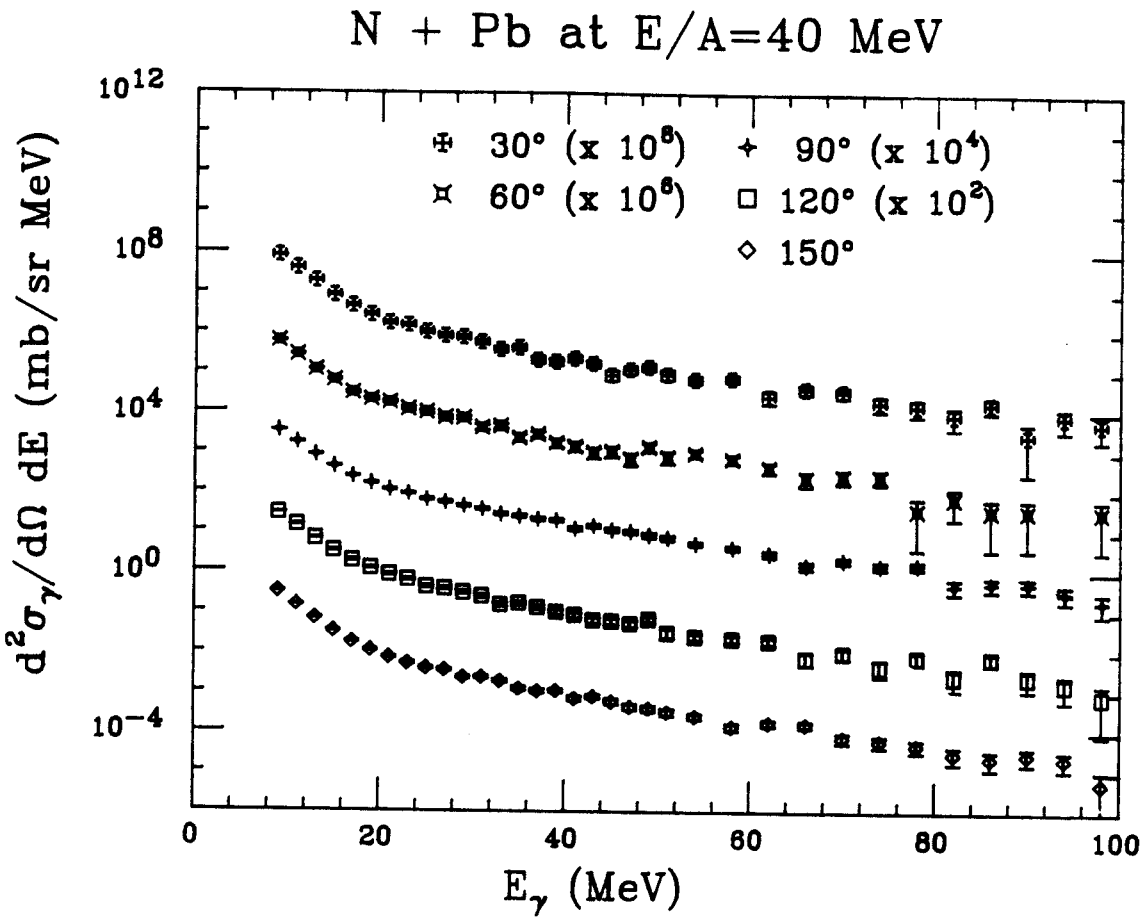

Figure I-14 Double-differential cross section N + Pb at E/A=40 MeV.

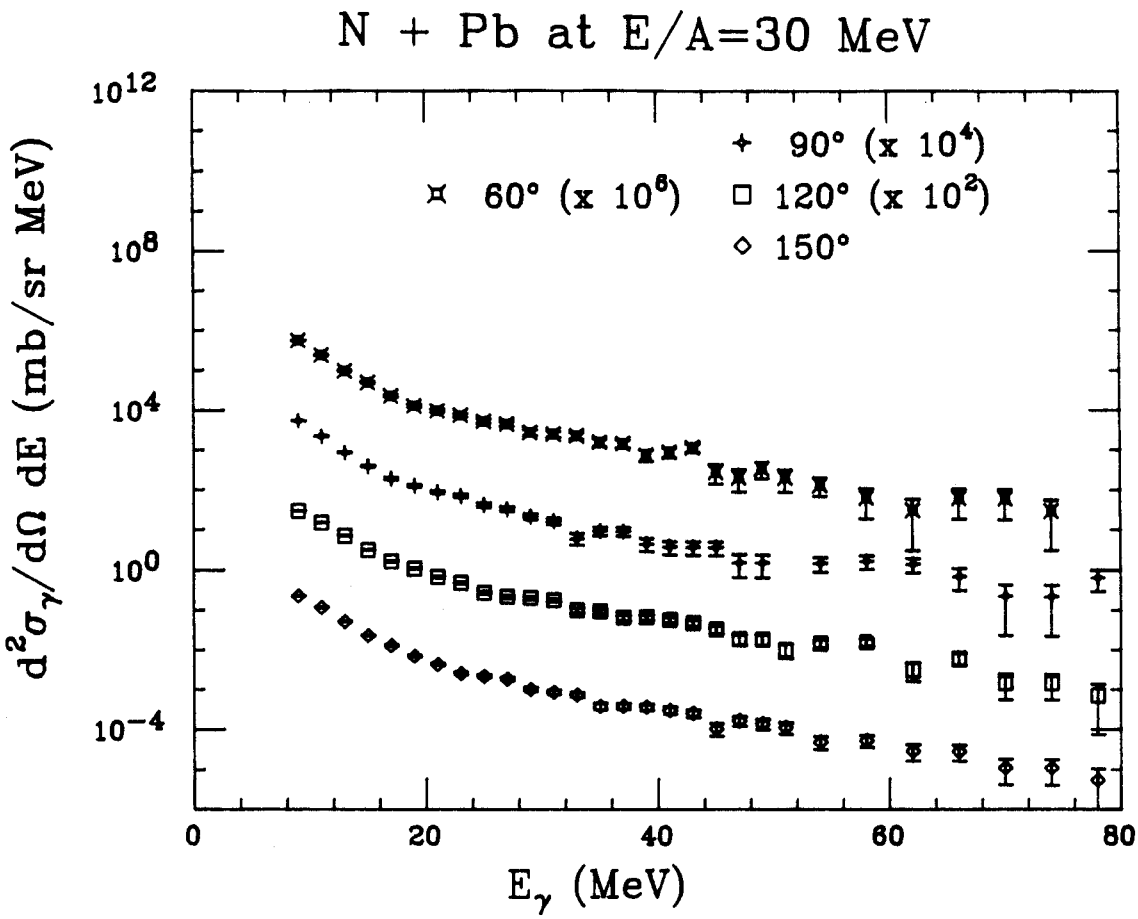

Figure I-15 Double-differential cross section N + Pb at E/A=30 MeV.

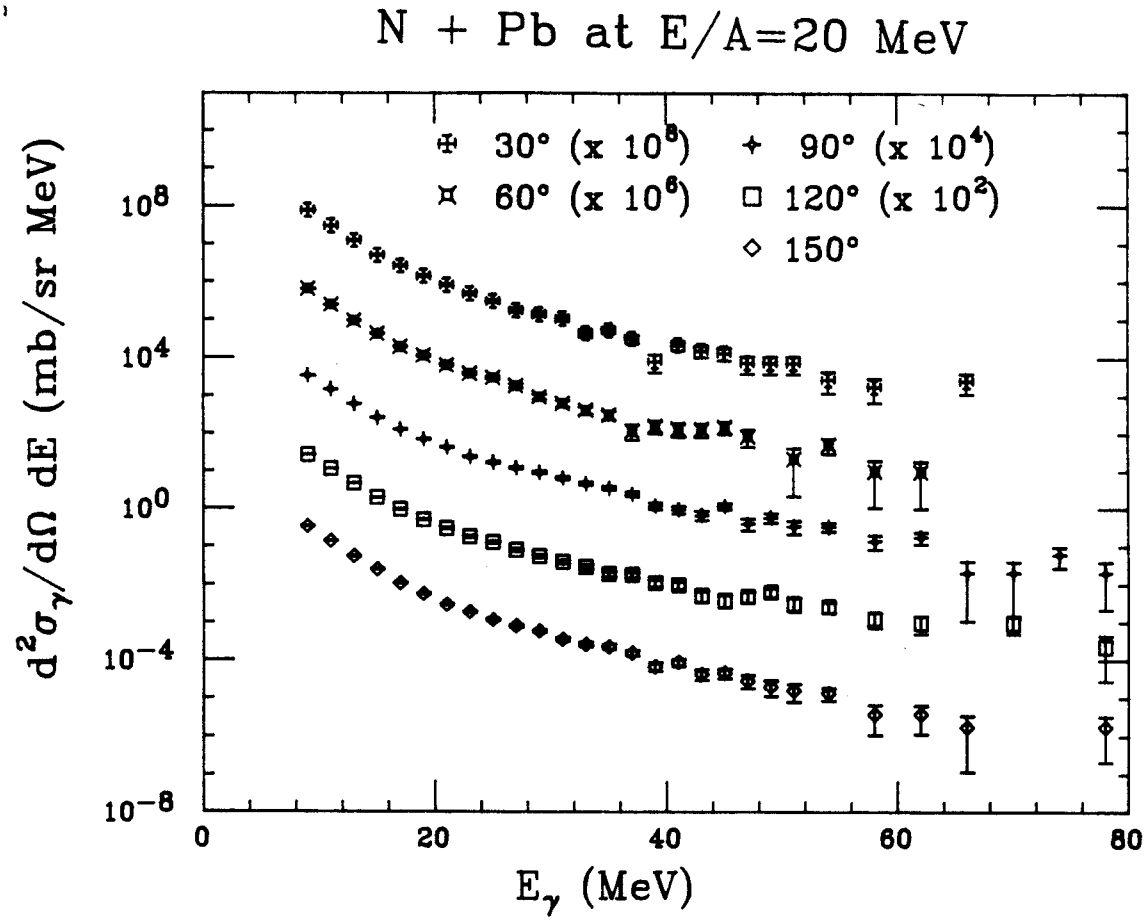

Figure I-16 Double-differential cross section N + Pb at E/A=20 MeV.

recoiling source with an exponential function b^{-E/τ_2}. The values of the inverse slope parameter τ_2 are reported in Table I-3.

The cross-section (equation I-5) was calculated at different angles as function of β, the source velocity/c.

$$\text{I-5} \qquad \left.\frac{d\sigma^2}{dEd\Omega}\right|_{\text{source}} = \left.\frac{d\sigma^2}{dEd\Omega}\right|_{\text{lab}} \frac{E_{\text{source}}}{E_{\text{lab}}}$$

$$E_{\text{source}} = \sqrt{E^2_{\text{lab}}\sin^2\theta + \gamma^2(E_{\text{lab}}\cos\theta - \beta E_{\text{lab}})^2}$$

$$\gamma = \frac{1}{\sqrt{1-\beta^2}}$$

The value of β, for each system and for each energy, corresponding to the frame in which the emission is nearly isotropic, is reported in Table I-3. The source velocity values are fairly close to the nucleon-nucleon system velocities. Both source velocities and slope parameters appear to be nearly independent of the target chosen and increase with increasing energy.

The alternate method of making rapidity plots, to test the idea of isotropic emission and to obtain information about the source velocity, was also employed. In general, the rapidity y of a particle of energy E and momentum p moving along a direction characterized by an angle θ, is defined as in equation I-6.

TABLE I-3 Parameters from the best fit to the high-energy gamma-ray data for $E_\gamma > 35$ MeV.

Target	E/A(MeV)	τ_2(MeV)	β_{exp}	β_{n-n}	$\beta_{nucleus-nucleus}$
Pb	20	10.0	0.08	0.104	0.013
Pb	30	12.0	0.11	0.127	0.016
Pb	40	14.2	0.10	0.145	0.019
Zn	20	8.3	0.05	0.104	0.037
Zn	30	11.8	0.11	0.127	0.045
Zn	40	13.7	0.10	0.145	0.052
C	20	7.7	0.08	0.104	0.111
C	30	11.1	0.10	0.127	0.135
C	40	13.3	0.12	0.145	0.156

I-6 $$y = \frac{1}{2}\ln\left(\frac{E + p_{\parallel}}{E - p_{\parallel}}\right) = \frac{1}{2}\ln\left(\frac{1 + \beta_{\parallel}}{1 - \beta_{\parallel}}\right) = \frac{1}{2}\ln\left(\frac{1+\beta\cos\theta}{1-\beta\cos\theta}\right)$$

In the laboratory frame a particle with velocity β" has an associate rapidity y". In a frame moving with velocity β with respect to the lab frame, the same particle will have velocity β' and rapidity y'. The relation between the three velocities β, β', and β" is shown in equation (I-7)

I-7 $$\beta'' = \frac{\beta + \beta'}{1 + \beta\beta'}$$

Equation I-8 shows the additive propriety of the rapidity.

I-8 $$y'' = \frac{1}{2}\ln\left(\frac{1 + \beta}{1 - \beta}\right) = \frac{1}{2}\ln\left(\frac{1 + \frac{\beta + \beta'}{1 + \beta\beta'}}{1 - \frac{\beta + \beta'}{1 + \beta\beta'}}\right) =$$

$$y'' = \frac{1}{2}\ln\left(\frac{(1 + \beta)(1 + \beta')}{(1 - \beta)(1 - \beta')}\right) = \frac{1}{2}\ln\left(\frac{1 + \beta}{1 - \beta}\right) + \frac{1}{2}\ln\left(\frac{1 + \beta'}{1 - \beta'}\right)$$

$$y'' = y + y'$$

If a frame where the emission is isotropic exists, the plots will be symmetric and the abscissa of the center of symmetry will represents the rapidity of the source (equation I-9).

I-9 $$y_{cen} = \frac{1}{2}\log\left(\frac{1+\beta}{1-\beta}_{source}\right)$$

In order to take advantage of the general properties of the rapidity we used the experimental cross-section data to generate invariant cross-section (equation I-10) versus energy plots.

I-10 $$\frac{d^2\sigma}{dp_{\parallel}} = \frac{1}{p}\frac{d^2\sigma}{dE\,d\Omega}$$

The curve for each angle was fitted with a function of the form $y=Ae^{-Bx}$. The intersection between three constant values of the invariant cross section and each of the fitted curves defined energy values on the abscissa. For each of the three invariant cross-section values, the rapidity (equation I-6) was plotted against the quantity $p_{\perp} = E\sin\theta$. Figures I-17 through I-19 show the rapidity plots for the three systems and the three energies under consideration. The curved line connecting the five data points is obtained with a cubic spline fit. The rapidity for a nucleon-nucleon system is also indicated. The general features of the plots are consistent with the idea of the existence of an emitting source moving with a velocity close to the nucleon-nucleon center of mass velocity.

In Figures I-20 through I-28 the angular distributions for N+Pb, Zn and C at 20, 30 and 40 MeV/n are shown for three different lower energy cuts on the gamma-ray energy at 20, 40 and 60 MeV. The angular distributions are all slightly forward peaked. At 40 MeV/n the angular

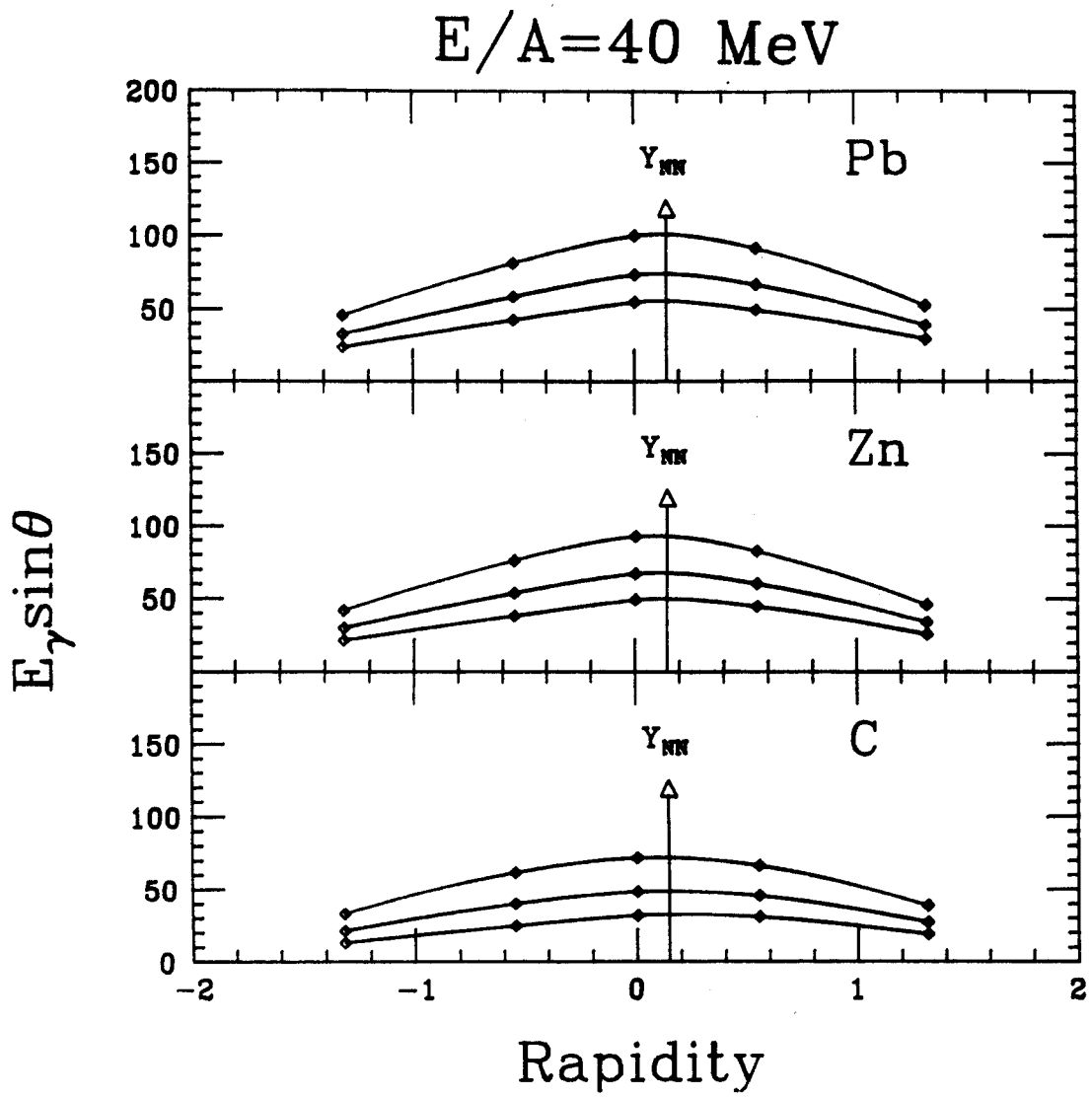

Figure I-17 Rapidity plot for Pb, Zn and C at E/A=40 MeV.

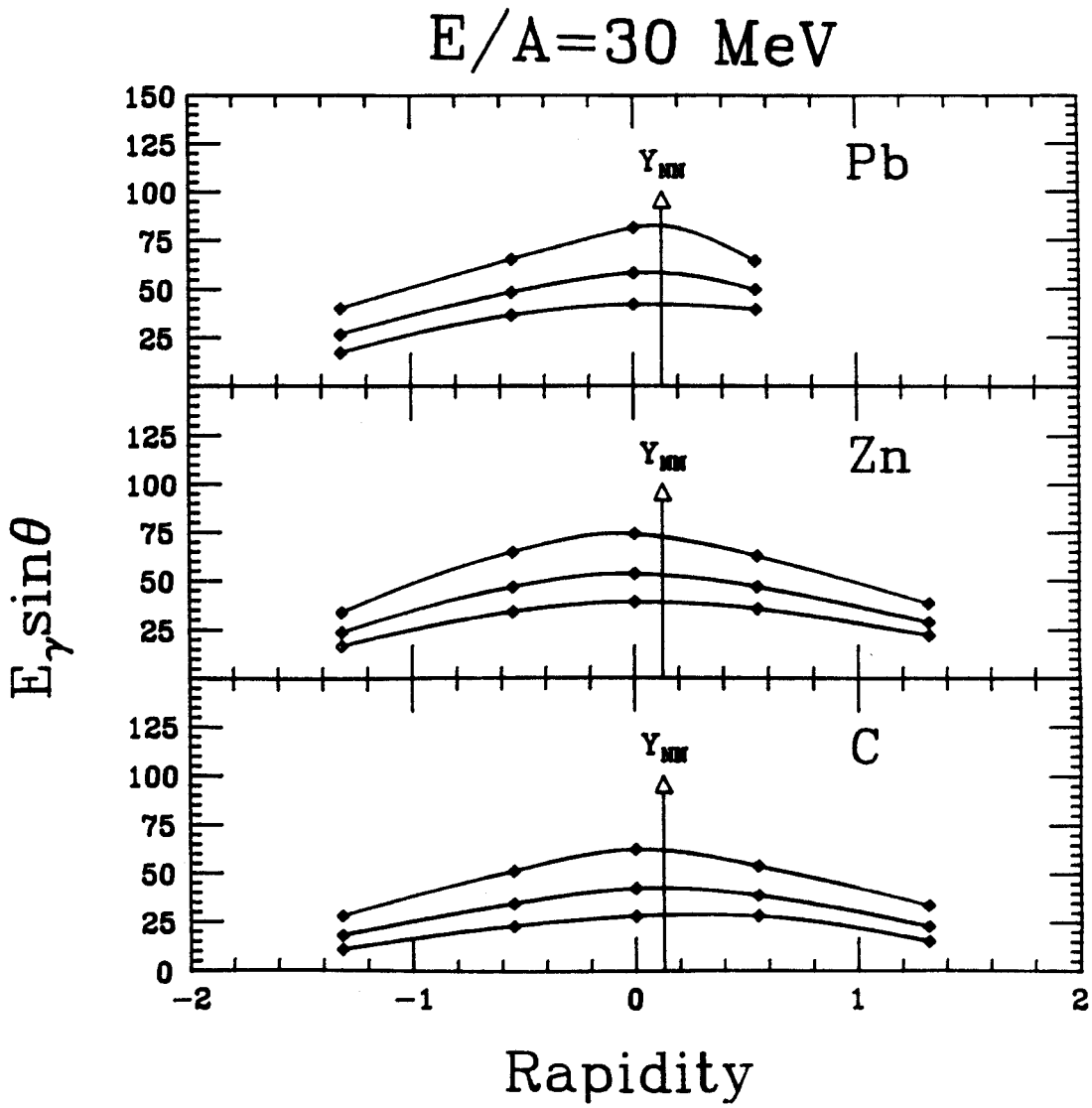

Figure I-18 Rapidity plot for Pb, Zn and C at E/A=30 MeV.

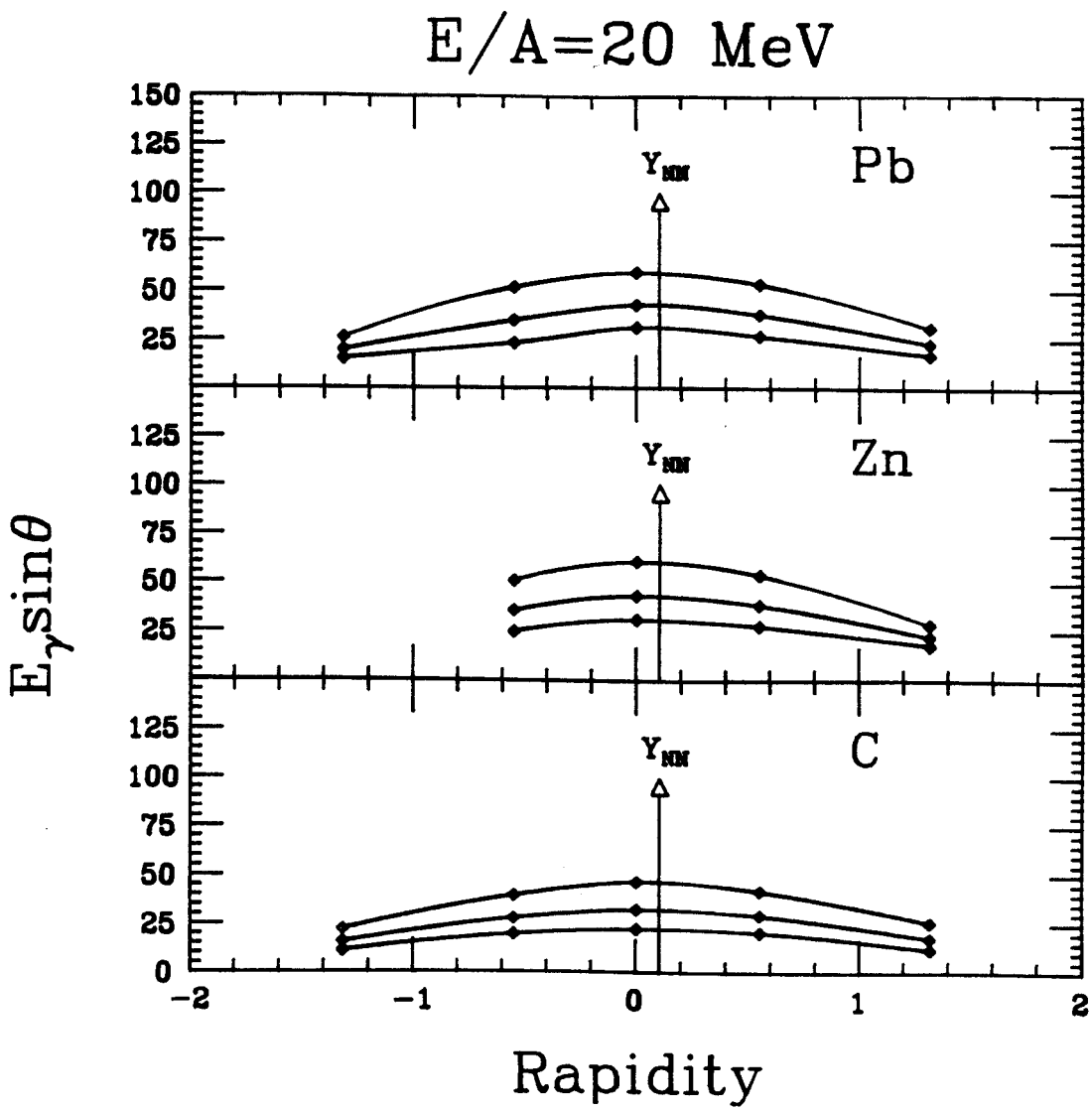

Figure I-19 Rapidity plot for Pb, Zn and C at E/A=20 MeV.

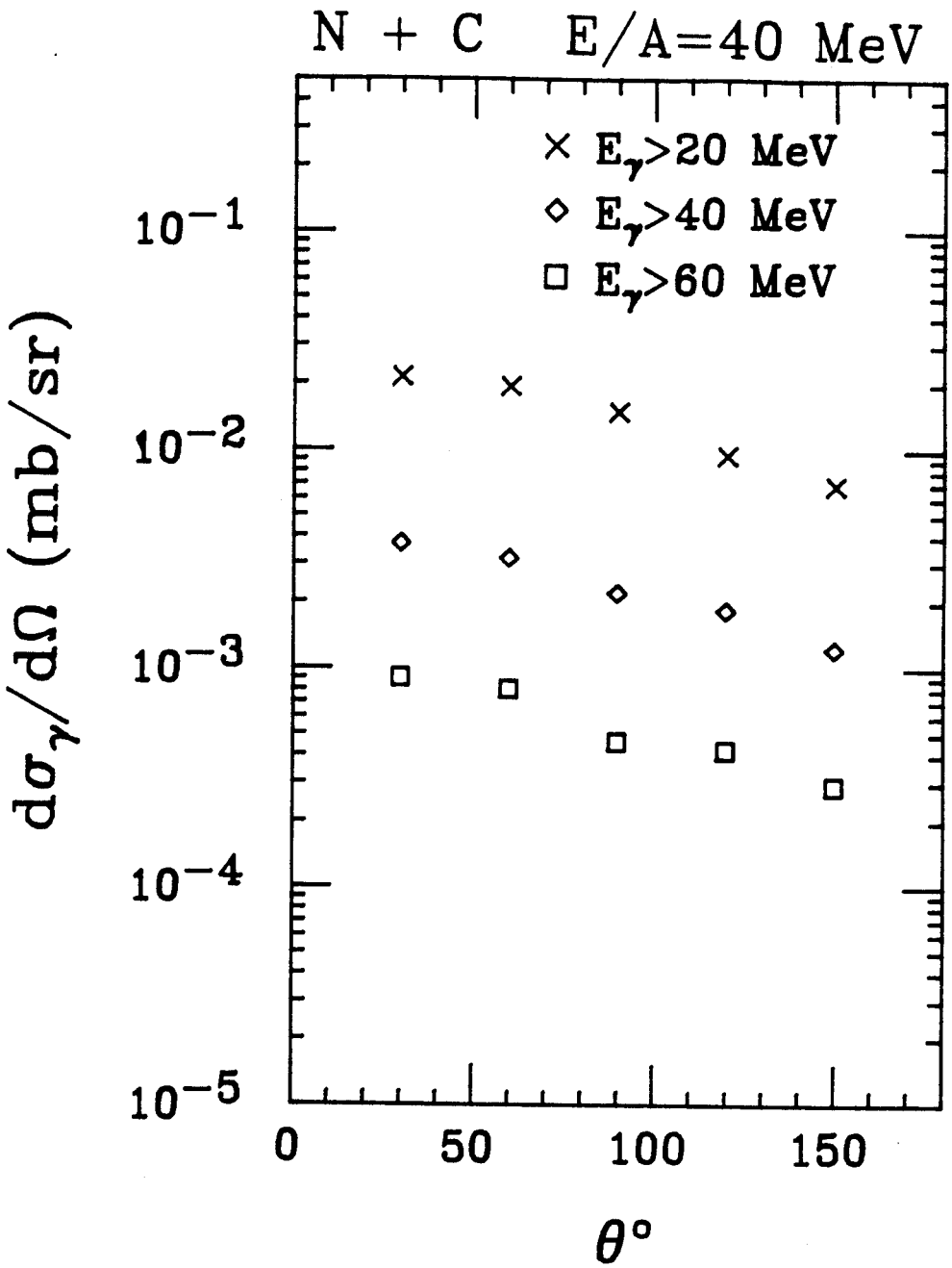

Figure I-20 N + C at E/A=40 MeV. Angular distribution for E_γ above 20, 40 and 60 MeV.

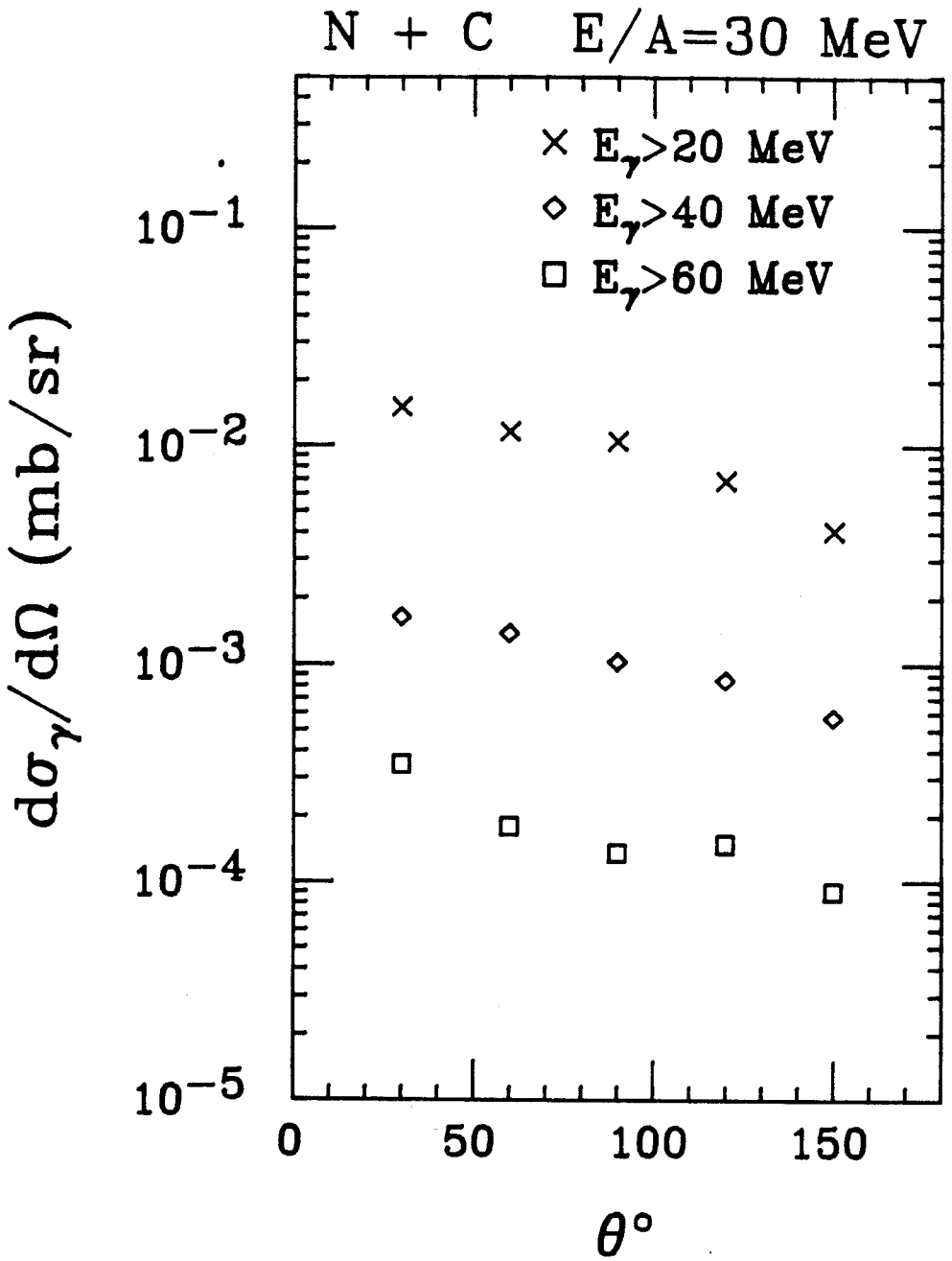

Figure I-21 N + C at E/A=30 MeV. Angular distribution for E_γ above 20, 40 and 60 MeV.

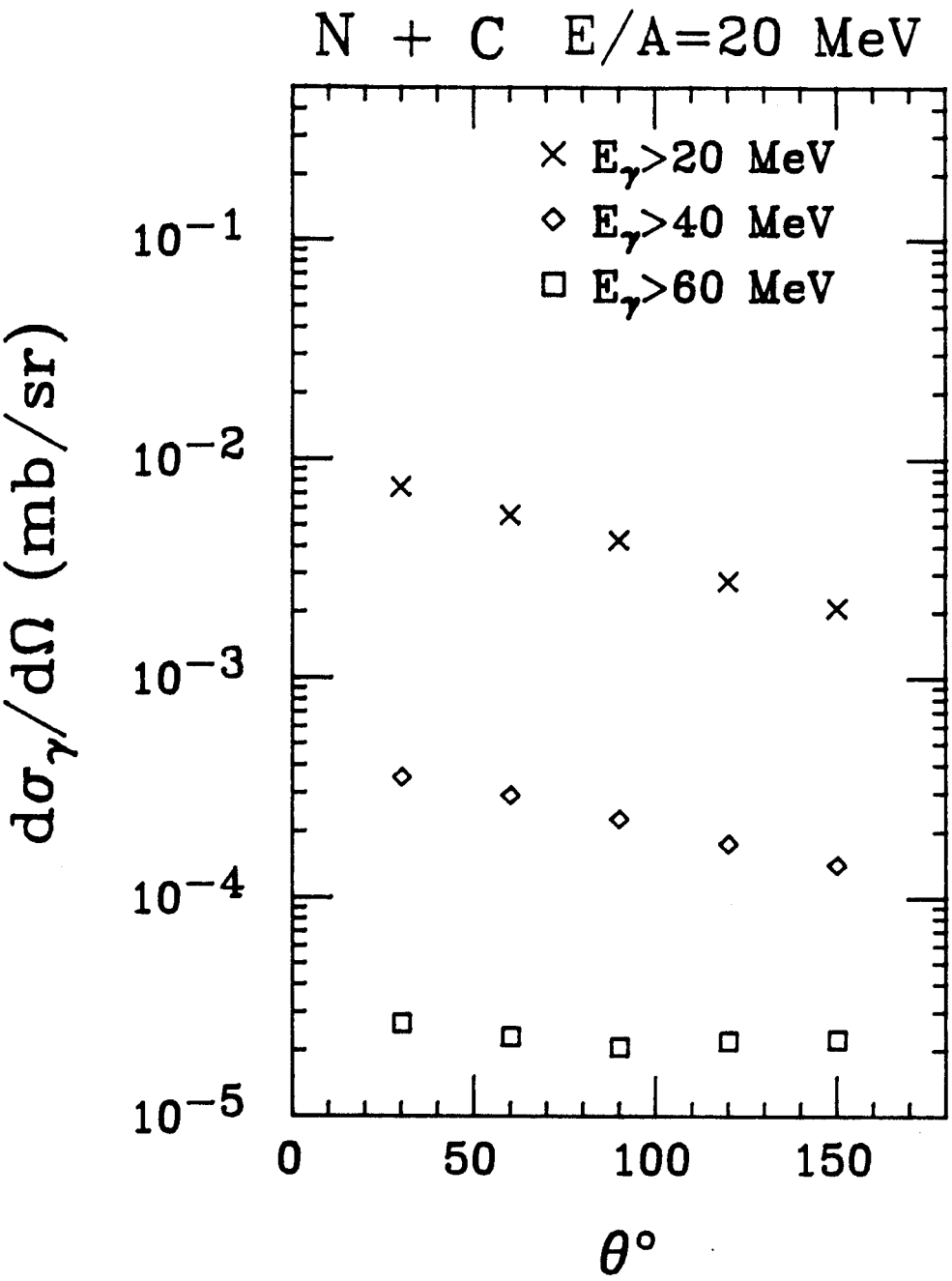

Figure I-22 N + C at E/A=20 MeV. Angular distribution for E_γ above 20, 40 and 60 MeV.

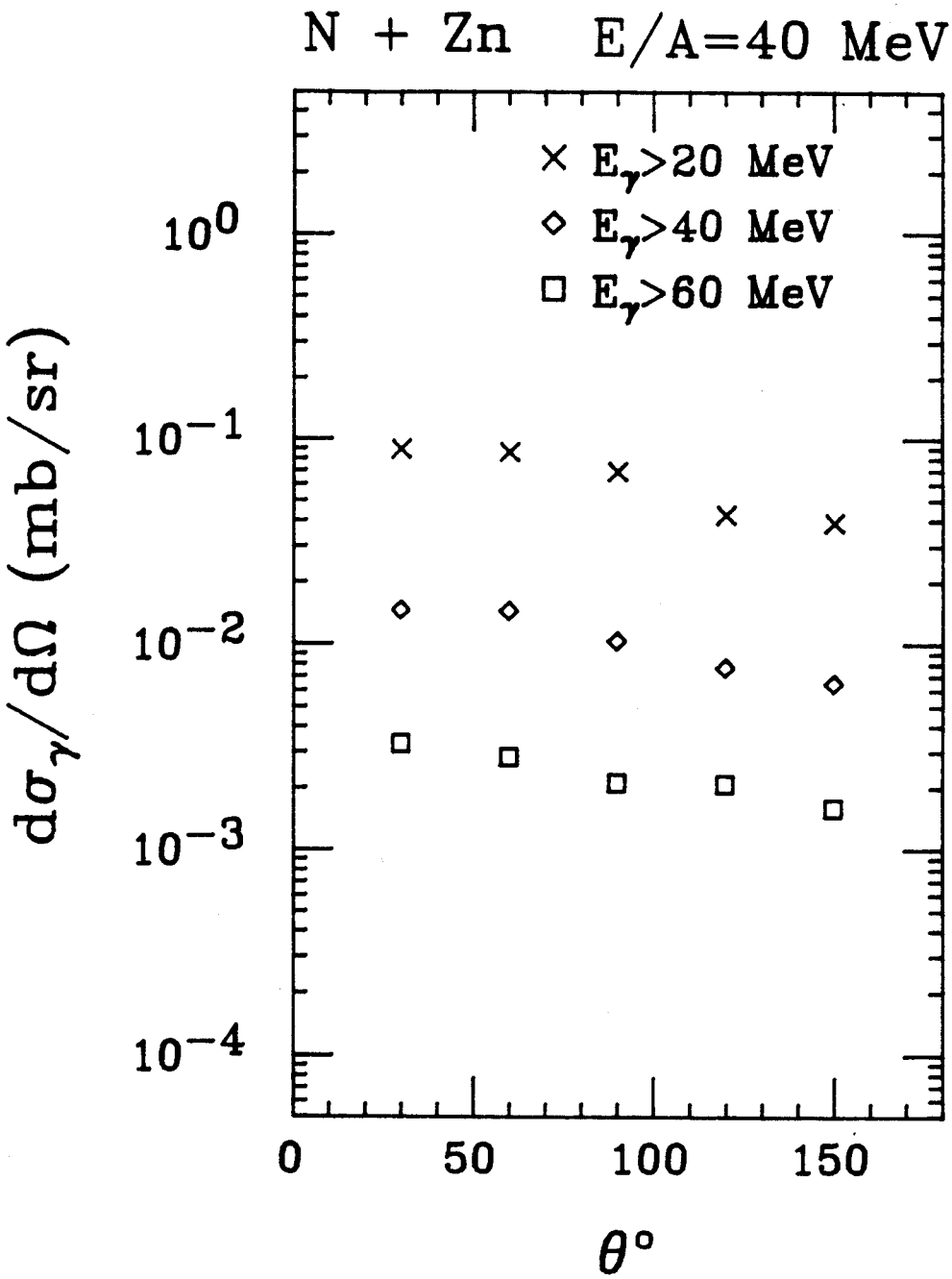

Figure I-23 N + Zn at E/A=40 MeV. Angular distribution for E_γ above 20, 40 and 60 MeV.

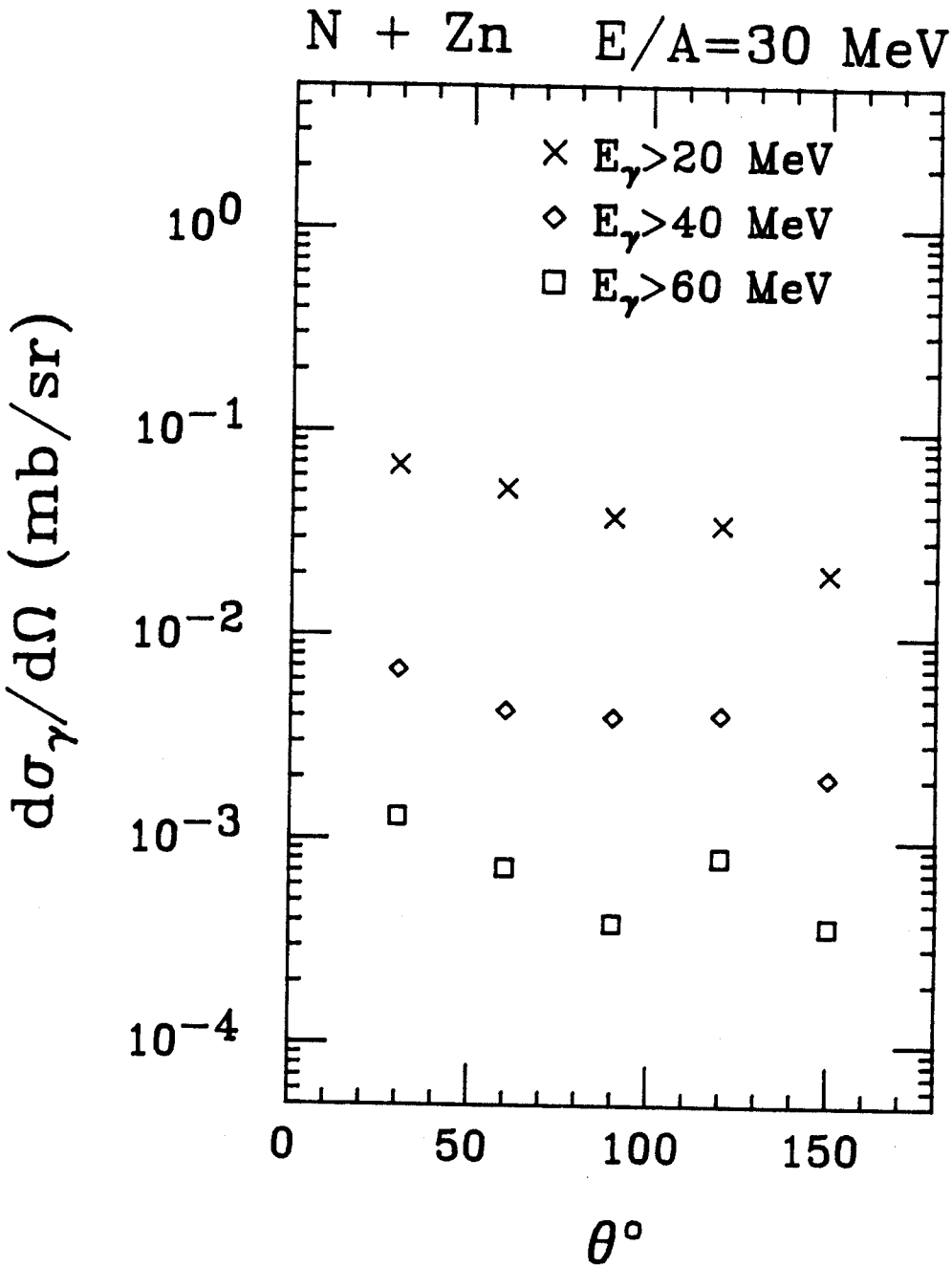

Figure I-24 N + Zn at E/A=30 MeV. Angular distribution for E_γ above 20, 40 and 60 MeV.

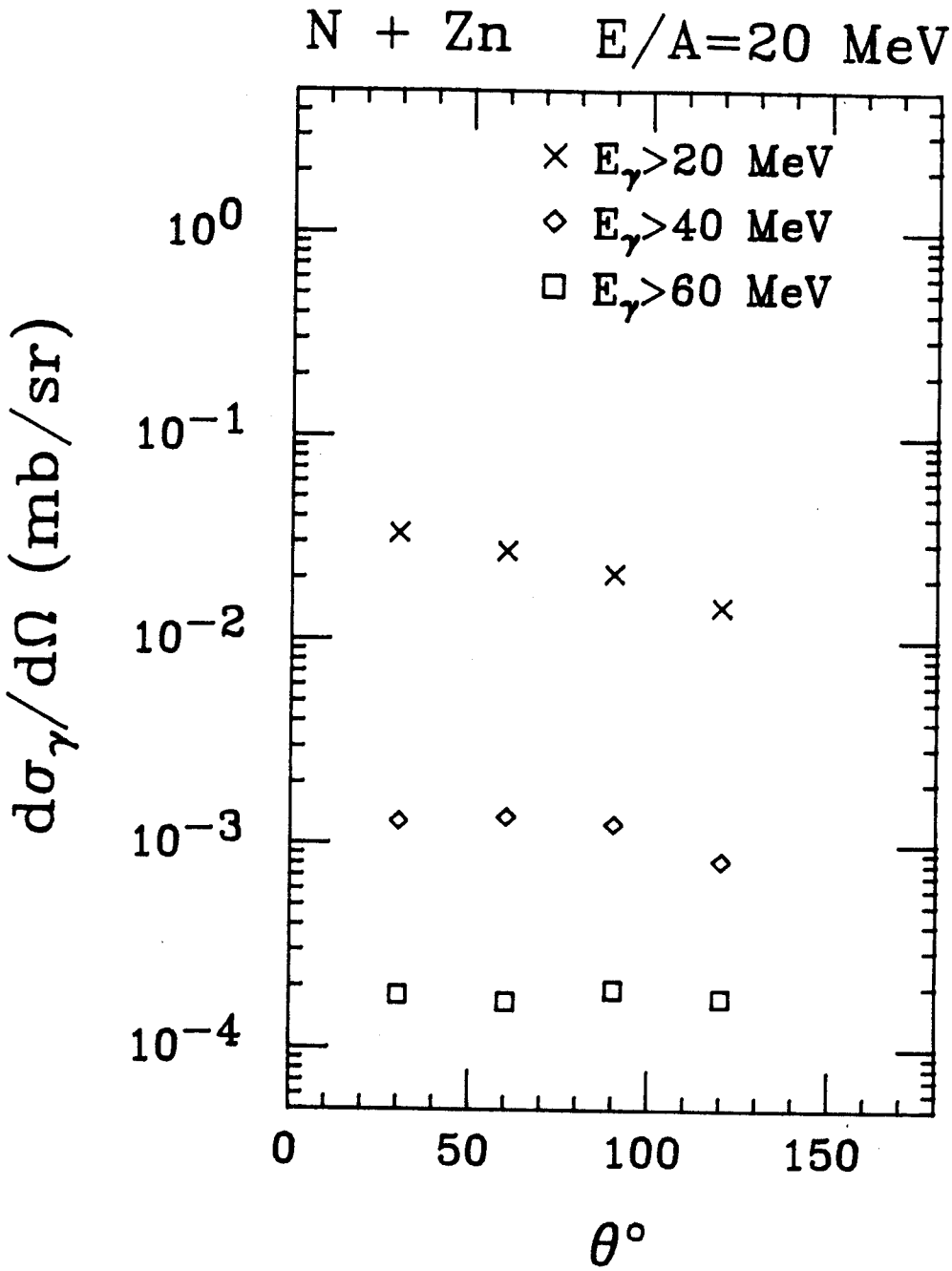

Figure I-25 N + Zn at E/A=20 MeV. Angular distribution for E_γ above 20, 40 and 60 MeV.

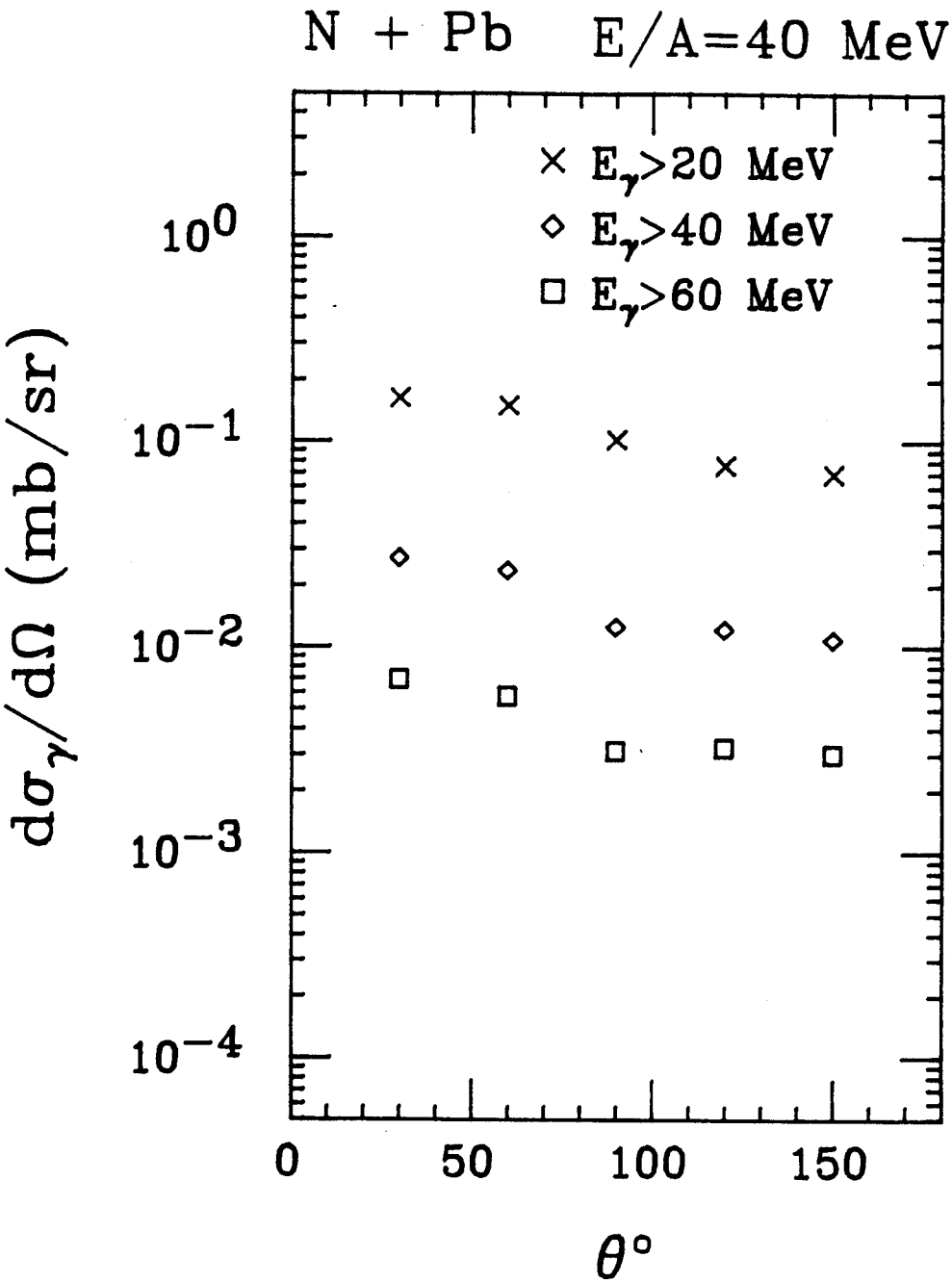

Figure I-26 N + Pb at E/A=40 MeV. Angular distribution for E_γ above 20, 40 and 60 MeV.

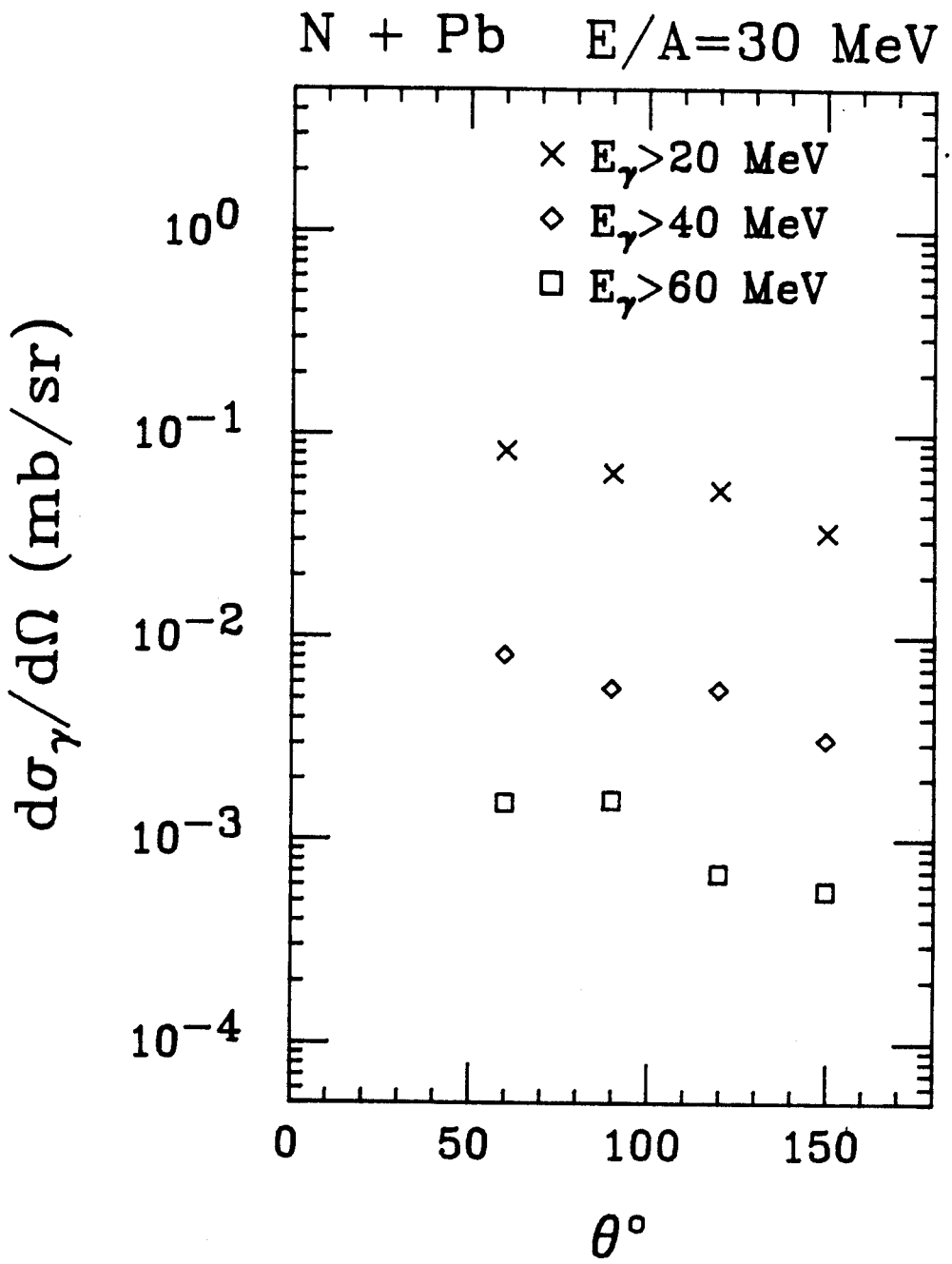

Figure I-27 N + Pb at E/A=30 MeV. Angular distribution for E_γ above 20, 40 and 60 MeV.

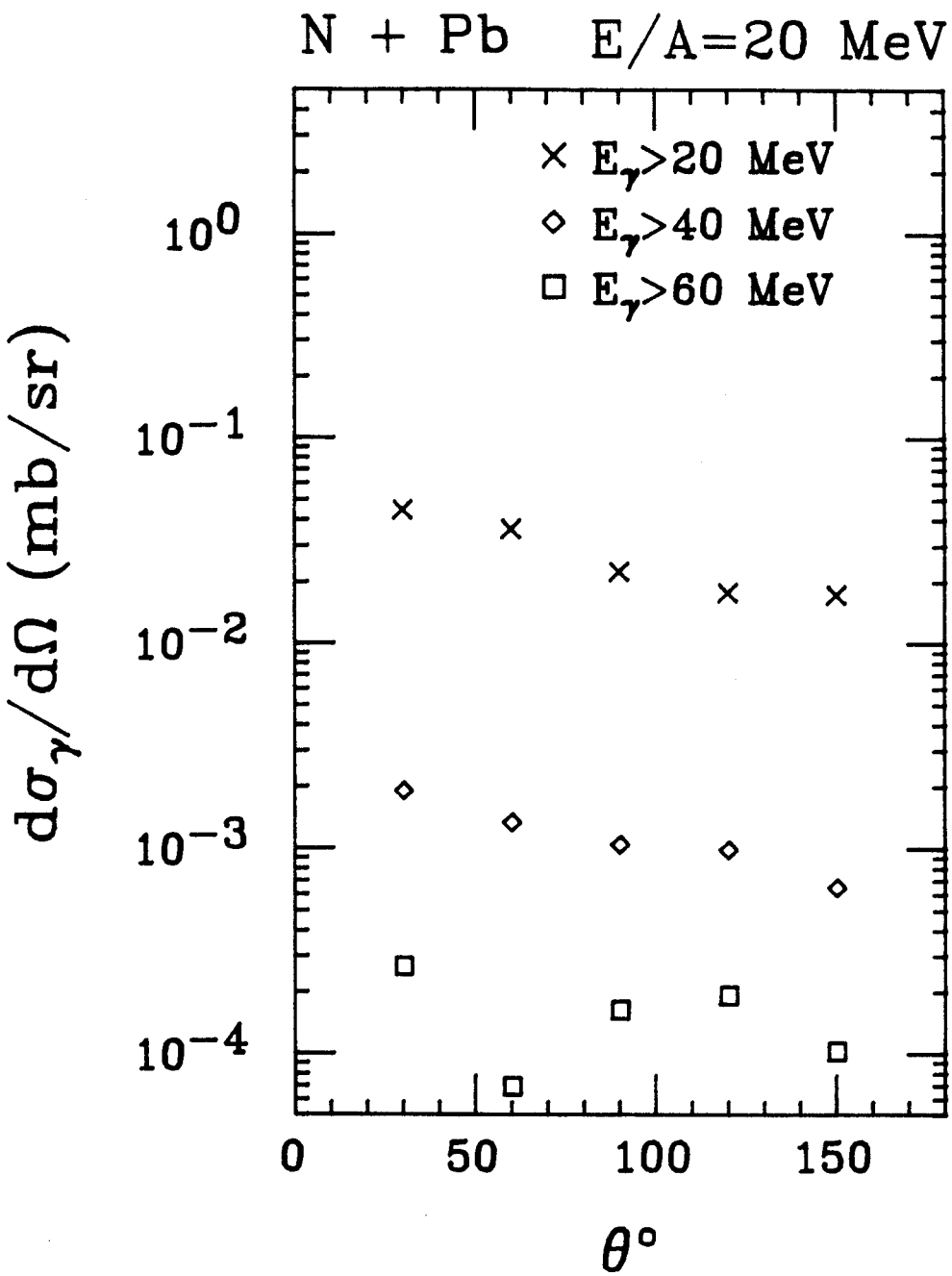

Figure I-28 N + Pb at E/A=20 MeV. Angular distribution for E_γ above 20, 40 and 60 MeV.

distributions integrated for $E_\gamma > 20$ MeV give for the ratio $\sigma(30°)/\sigma(150°)$: 2.35 for Pb, 2.28 for Zn and 3.14 for C. Similar behavior is found for all targets and beam energies. The total cross-sections at 90° for gamma-ray energies above 20 MeV are shown in Table I-4.

TABLE I-4 Total cross sections at 90° for gamma-ray energies above 20 MeV.

Target	Cross section (mb)		
	20 MeV/n	30 MeV/n	40 MeV/n
Pb	0.11	0.36	0.64
Zn	0.10	0.21	0.43
C	0.02	0.06	0.09

CHAPTER II

HIGH-ENERGY GAMMA RAYS: DATA COMPARISON AND THEORY

A. EXPERIMENTAL COMPARISON

The main characteristics of the gamma-ray spectra emerging from the experiment described in Chapter I are the exponential decrease of the double-differential cross section with energy and a nearly isotropic angular distribution in a frame moving with velocity close to the nucleon-nucleon center of mass velocity. These general features are in agreement with most of the results obtained by other experimental groups.

Grosse et al. [Gr 86] studied high-energy gamma rays, at the CERN syncrocyclotron, using a ^{12}C beam of 48, 60, 74 and 84 MeV/nucl. on targets from C to U. For constant values of the invariant photon cross section, they plotted the rapidity (equation I-3) against the transverse energy $E = E_\gamma \sin\theta$. The symmetry around the half rapidity line, not only for symmetric systems such as $^{12}C + ^{12}C$ but also for very asymmetric systems such as $^{12}C + ^{238}U$, led this group to introduce the idea of "equal participants". In this picture, gamma rays, are assumed to be produced in a source formed from equally many participant nucleons out of the target and the projectile. The observed value of the source velocity could, on the other hand, be used as an argument to support the idea of direct n-p bremsstrahlung as the mechanism responsible for the gamma-ray production.

Kwato et al. [Kw 86] conducted two experiments: one at Grenoble at the Sara facility using an ^{40}Ar beam on an Au target at E/A=30 MeV and one at Caen at the Ganil facility using a ^{86}Kr beam on C, Ag, and Au targets at E/A=44 MeV. Great care was devoted to the determination of the angular distribution and especially to its departure from a perfectly isotropic one in a frame moving with velocity close to the nucleon-nucleon center of mass velocity. A dipolar component was found in the 44 MeV/nucl. data and its amplitude was found to vary little in the wide mass range under study, with a mean value of 24%.

During a later experiment our group collected data on the reaction ^{40}Ar + Au → Y + X at E/A=30 MeV. Figure II-1 shows a comparison at 90° between our data and the Kwato et al. data. Within error bars the two double-differential cross-sections agree both in slope and magnitude.

R. Hingmann et al. [Hi 86] studied the reaction ^{40}Ar + ^{158}Gd at E/A=44 MeV at GANIL. The main aim of this experiment was to analyze the gamma-ray emission process as a function of impact parameter. Besides observing the coincidence between gamma rays and reaction products, the result of which will be discussed in chapter IV, inclusive spectra at 90° and 145° were also measured. The exponential decrease of the spectra and the fairly constant angular distribution are in agreement with the above mentioned experiments.

Completely different results were obtained by N. Alamanos et al. [Al 86] who made inclusive measurements of high-energy gamma rays produced in the reaction ^{14}N + Ni → Y + X with a 35 MeV/nucl. beam at the NSCL. The slopes of the exponential spectra are independent of the laboratory angle and the angular distribution in the laboratory is not

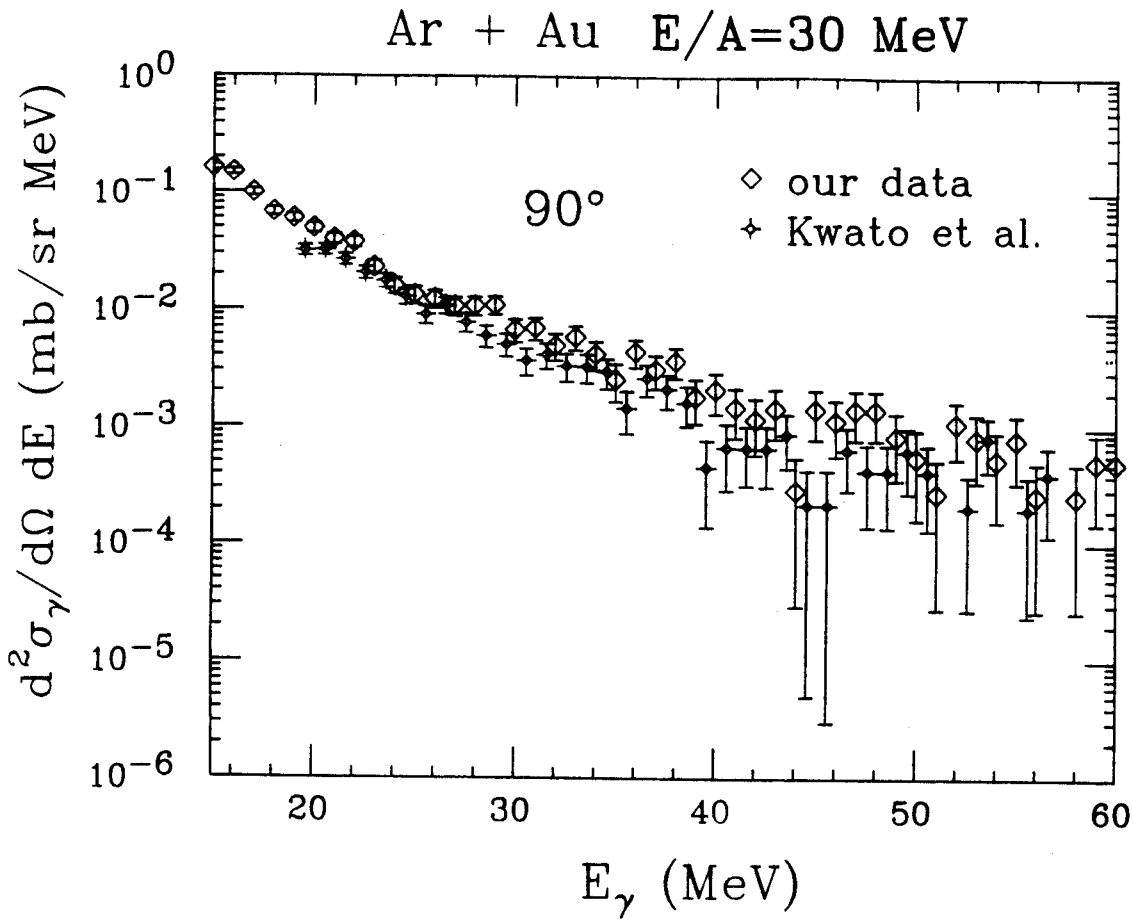

Figure II-1 $d\sigma^2/(dE\ d\Omega)$ at 90° for Ar + Au at E/A=30 MeV: Kwato et al. and ours (after calibration corrections).

forward peaked but has a predominant dipolar-like behavior with a maximum at 90°.

Very recently C. Gossett et al. [Gu 87] studied the gamma-ray production resulting from bombarding Al, Ni, Mo and Ta targets with a 19 MeV/nucl. ^{19}F beam at Berkeley. Although most of the features agree with the general trend, the magnitudes of the cross sections are larger than the ones we obtained for similar systems. Figure II-2 shows that the spectrum taken at 90° for the reaction ^{19}F + ^{58}Ni at E/A=19 MeV is a factor of 3 larger than our data for the reaction ^{14}N + ^{65}Zn at E/A=20 MeV at the same angle.

B. THEORETICAL MODELS

The explanation of the existence of a reaction product not present in the entrance channel of a reaction is not a simple theoretical task. Several reaction mechanisms have been suggested in the last few years to interpret the experimental high-energy gamma-ray spectra.

1. Bremsstrahlung

When charged particles pass through matter they are scattered and lose energy mainly by collisions with the atomic electrons since nuclear collisions are much less likely to happen. Energy loss is also possible by emission of electromagnetic radiation. When a charged particle passes through a nuclear field, its velocity changes which gives rise to acceleration and, from Maxwell's equations, to electromagnetic

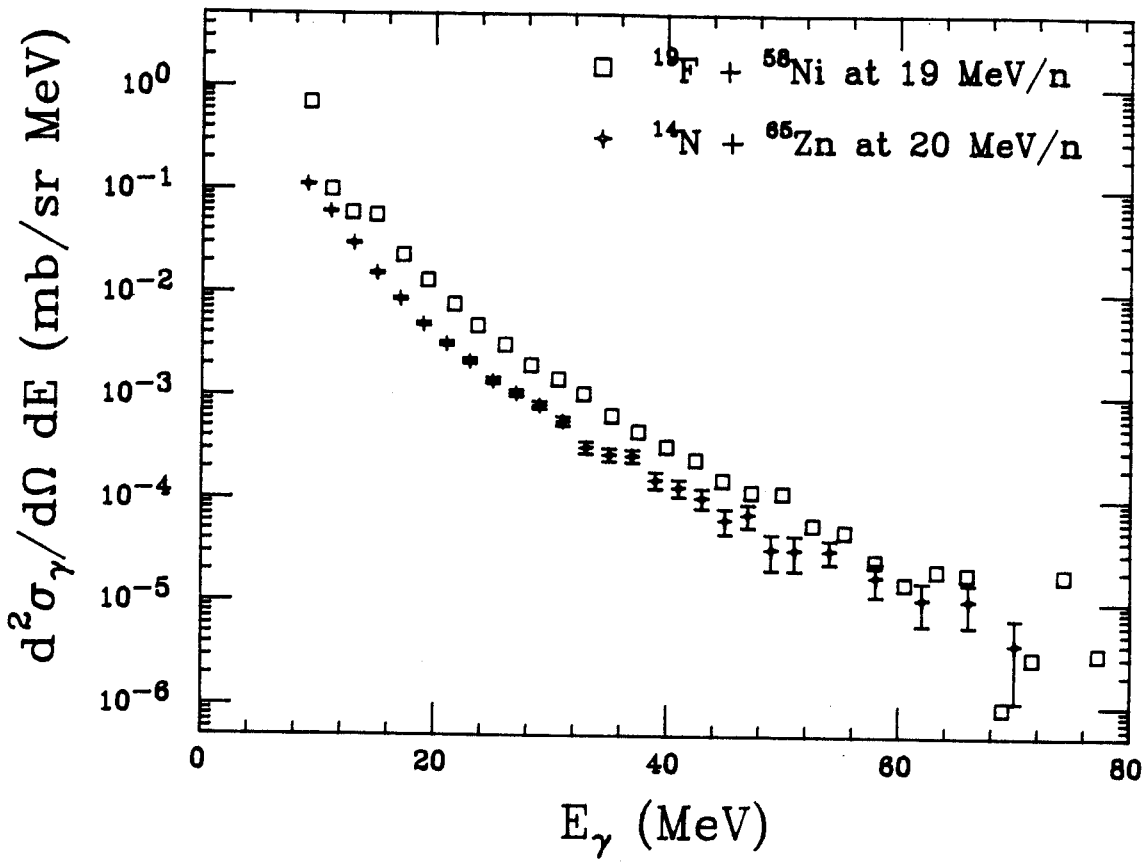

Figure II-2 $d\sigma^2/(dE\ d\Omega)$ at 90°: our N + Zn at E/A=20 MeV (after calibration corrections) and Gossett et al. F + Ni at E/A=19 MeV.

radiation. The emitted radiation is often called bremsstrahlung (braking radiation).

In a heavy ion collision, bremsstrahlung radiation can arise from mechanisms involving different degrees of collectivity: nucleus-nucleus, nucleon-nucleus, or nucleon-nucleon collisions. Below is a short description of the models used for the different processes. Their ability to reproduce the experimental results is also discussed.

1a. Nucleus-nucleus bremsstrahlung.

This component of the bremsstrahlung is associated with the collective behavior of the nucleons in the first stage of the reaction. For symmetric systems, the angular distribution in the center of mass frame has a quadrupolar nature with a characteristic minimum at 90° [Va 84]. In asymmetric systems the same behavior is still predicted for collisions where the projectile and target have the same A/Z ratio [Ni 85]. A look at the angular distribution obtained for the symmetric system $^{12}C + C$ [Gr 86] and for the nearly symmetric system $^{14}N + C$ [St 86] clearly rules out the nucleus-nucleus bremsstrahlung as the main mechanism in the gamma-ray production.

Ko et al. [Ko 86], in a study done with the intranuclear cascade model (INC) [Be 81], suggested the possibility of observing this collective process in the photon range between 10 and 30 MeV for heavy nuclei with A>40. Experiments in search of this component have recently been performed and they are currently under analysis.

1b. Nucleon-nucleus

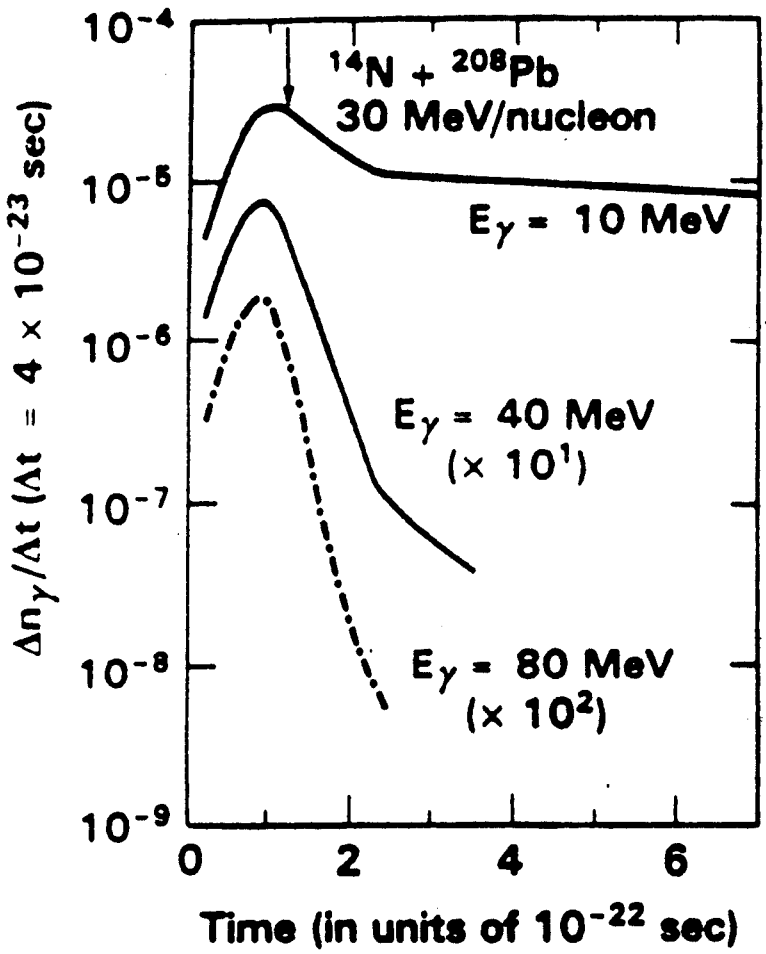

Figure II-4 Number of gamma rays emitted as a function of time for the reaction N + Pb at E/A=30 MeV. The arrow indicates the time at which the colliding nuclei have completely fused.

The nucleon-nucleus bremsstrahlung contribution to the gamma-ray yield has been studied by Bauer et al. [Ba 85] in the framework of the time dependent Hartree-Fock (TDHF) theory and found to be at least an order of magnitude too small to explain the data.

K. Nakayama and G. F. Bersch [Na 86] used the infinite matter approximation to study the contribution of the bremsstrahlung from a potential field compared to the contribution of the collisional process and found it to be negligible.

1c. Nucleon-nucleon bremsstrahlung

In the nucleon-nucleon bremsstrahlung the dipolar proton-neutron bremsstrahlung is the predominant component and the quadrupolar proton-proton bremsstrahlung is several orders of magnitude smaller [Ni 85].

Remington et al. [Re 87a] used the Boltzmann master equation (BME) [Bl 81] to follow the intranuclear nucleon-nucleon collision process. Boltzmann-like coupled, first-order differential equations are used to describe the rate of change of the nucleon occupation probability as a function of energy above the bottom of the nuclear well. The Fermi motion of both the target and the projectile are considered and superimposed on the projectile momentum to obtain gamma-ray energies above the kinematical limit given by the projectile energy. The Fermi motion is also expected to flatten the dipolar angular distribution so as to reproduce the nearly isotropic experimental results. The neutron-proton bremsstrahlung is added to the BME as a perturbation and the elementary reaction process is represented by equation II-2.

$$\text{II-2} \qquad \frac{d^2N}{dE_\gamma\, d\Omega_\gamma} = \frac{\alpha}{(2\pi)^2 E_\gamma} \sum_{k=1}^{2} \left| \frac{\hat{\varepsilon}_k \cdot \hat{\beta}_i}{1 - \hat{q} \cdot \hat{\beta}_i} - \frac{\hat{\varepsilon}_k \cdot \hat{\beta}_f}{1 - \hat{q} \cdot \hat{\beta}_f} \right|^2 P_{fac}(1 + X)$$

Where $\alpha \approx \frac{1}{137}$ is the fine structure constant, $\hat{\beta}_i$ and $\hat{\beta}_f$ are the initial and final proton velocities, $\hat{\varepsilon}_i$, $\hat{\varepsilon}_f$ and $\hat{q}$ are the unit vectors representing the two directions of polarization and the direction of propagation of the gamma ray. $P_{fac} = \frac{\beta_f \gamma_f}{\beta_i \gamma_i}$ is a quantum correction related to the available final state phase space [Na 86]. The (1 + X) factor for X = 0 reduces equation II-2 to a semiclassical result and for X = 1 gives a crude correction for meson exchange effects [Br 73]. The value X = 1 is chosen for the nucleus-nucleus calculations since the simpler proton-nucleus data of Edgington and Rose [Eg 66] are reproduced with it. Since the BME follows the intranuclear cascade only in energy space, no angular distribution is directly available. The cross section at 90° can, however, be obtained by dividing the differential cross section $\frac{d\sigma}{dE}$ in the nucleon-nucleon center of mass by 4π and neglecting the transformation factor $\gamma \approx 1$ between the center of mass and laboratory frame. Figure II-3 shows a comparison between the theoretical predictions for $^{14}N + {}^{12}C$ and $^{14}N + {}^{207}Pb$ at E/A=20, 30 and 40 MeV and the experimental results. Not included in the figure are the calibration correction factors of 2.5, 2.2 and 2.0 for beam energies of 20, 30 and 40 MeV/nucl. respectively. Figure II-4 shows the gamma-ray production as a function of time. The gamma-ray production seems to be

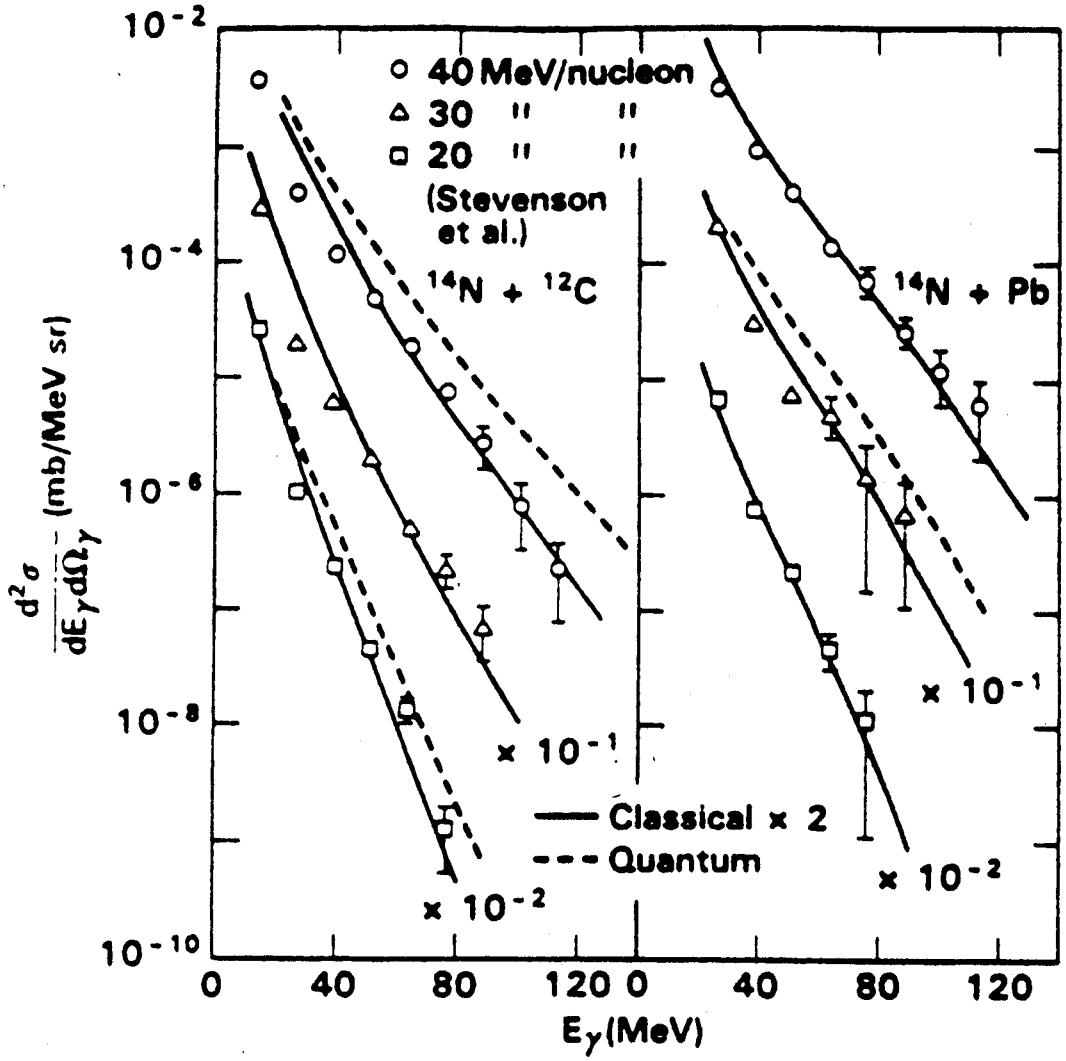

Figure II-3 Remington et al. theoretical results and our experimental results for N + C at E/A=20, 30 and 40 MeV (before calibration).

strongly related to the initial stage of the collision and the most energetic gamma rays appear to be produced mainly in the first collisions.

In a second study, Remington et al. [Re 87b] defined an "acceptance window" $\Delta\theta$, for injection of nucleons into the nuclear well. The uncertainty of the injection angle is then folded with equation II-1. Figures II-5 and II-6 show the angular distributions obtained within this picture and their comparison with the experimental values (before calibration). The dashed curves show the contribution of the first collision and the solid curves represent the sum of the first collision contribution and the secondary collision component assumed to be isotropic in the nucleon-nucleon center of mass.

Two recent dynamical studies of the neutron-proton bremsstrahlung done by Bauer et al. follow the collision both in coordinate and in momentum space. In the first [Ba 86], the elementary photon production cross section is represented by the non-relativistic expression (equation II-3) obtained by considering the collision of a particle of charge e and mass m with a fixed sphere of radius R.

$$\text{II-3} \qquad \frac{d^2\sigma_{elem}}{dE\, d\Omega_\gamma} = \frac{\alpha R^2}{12\pi E_\gamma}\left(2\beta_f^2 + 3\beta_i \sin^2\theta_\gamma\right)$$

where $\alpha = \frac{e^2}{hc}$ and R = radius of a sphere. The value $R \approx \sqrt{3}$ fm fits the data of Edginton and Rose. β_i and β_f are the initial and final velocities of the proton in the n-p center of mass. The impact parameter dependent double differential cross section is expressed as

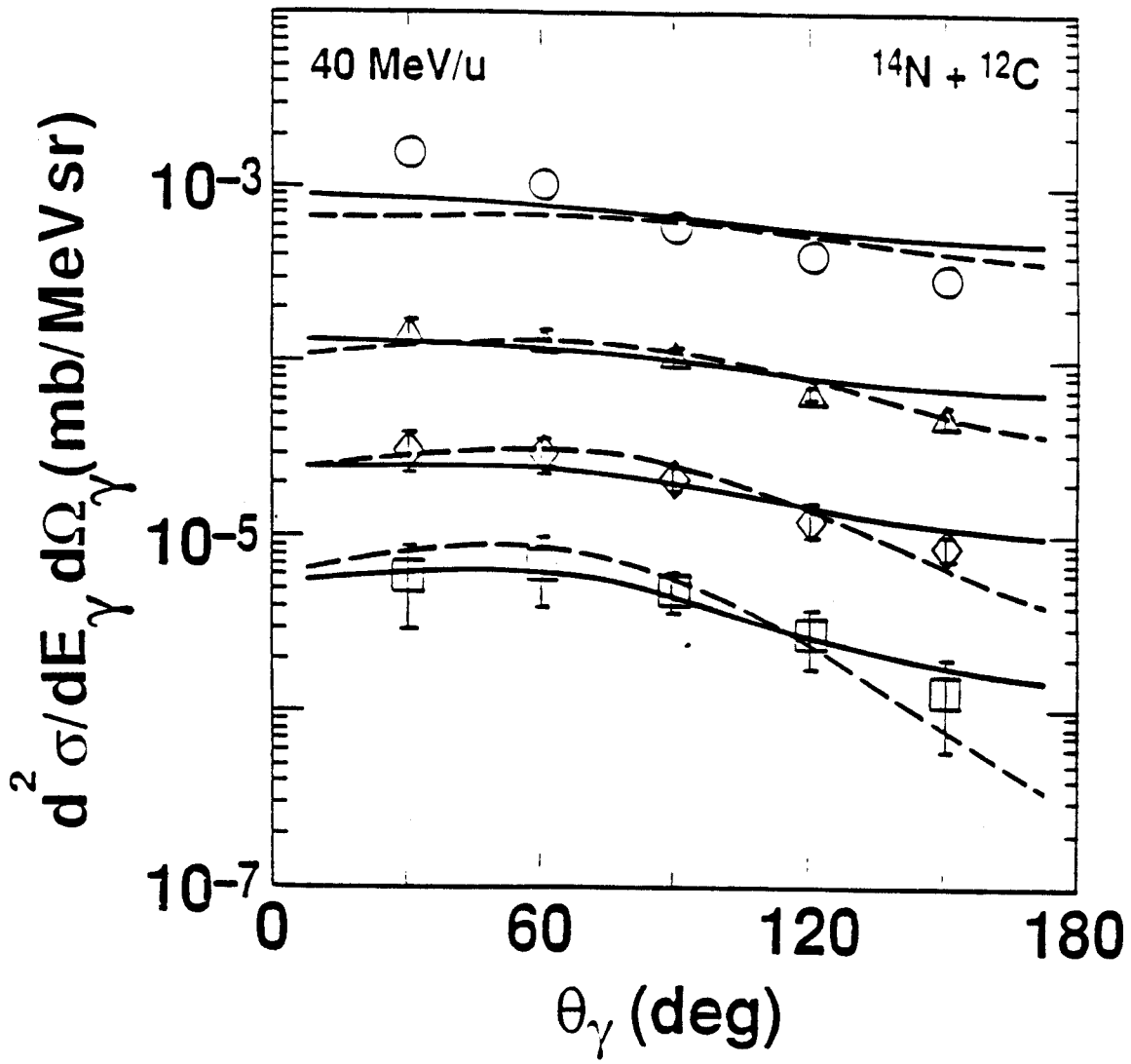

Figure II-5 Angular distribution for N + C at E/A=40 MeV: Remington et al. calculations and our data (before calibration correction).

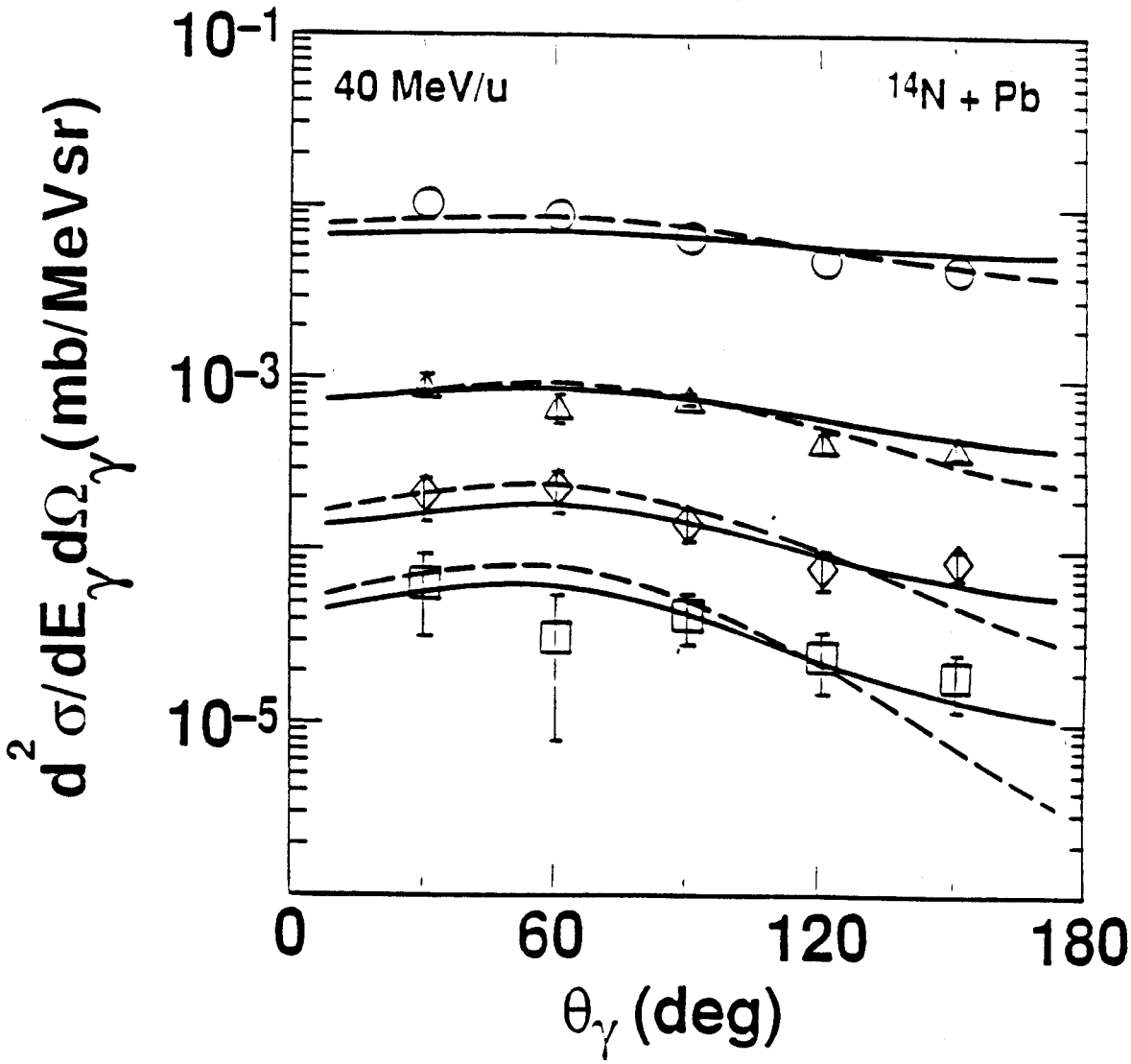

Figure II-6 Angular distribution for N + Pb at E/A=40 MeV: Remington et al. and our data (before calibration correction).

$$\text{II-4} \qquad \frac{d^2N(b)}{dE_\gamma d\Omega_\gamma} = \Sigma_{n\text{-}p\ coll} \int \frac{d\Omega}{4\pi} \frac{E}{E_\gamma'} \frac{1}{\sigma_{NN}} \frac{d^2\sigma_{elem}(k_1,k_2)}{dE_\gamma' \quad d\Omega_\gamma}$$

$$X\ [1-f(r,k_3,t)][1-f(r,k_4,t)].$$

The single particle distribution function $f_i=f(r_i,p_i,t)$ is a Wigner function, representing the phase-space density, and its time evolution is governed by the Boltzman-Uehling-Uhlembeck equation

$$\text{II-5} \qquad \frac{\partial f_1}{\partial t} + v\cdot\nabla_r f_1 - \nabla_r U \cdot \nabla_p f_1 = \frac{4}{(2\pi)^3} \int d^3k_2\ d^3k_3 d\Omega\ v_{12} \frac{d\sigma}{d\Omega}$$

$$X\ \delta^3(k_1+k_2-k_3-k_4)\ [f_1f_2(1-f_3)(1-f_4) - f_3f_4(1-f_1)(1-f_4)]$$

where $U(\rho)= - 218\ MeV\ \rho/\rho_0 + 164\ MeV\ (\rho/\rho_0)^{4/3}$.

Integration of equation II-4 over impact parameter gives the total yield in the nucleon-nucleon center of mass.

$$\text{II-6} \qquad \frac{d^2\sigma_{eff}}{dE_\gamma\ d\Omega_\gamma} = \int 2\pi b db \frac{d^2N(b)}{dE_\gamma\ d\Omega_\gamma}$$

From the dynamical nature of this model it is possible to extract information on the time the gamma rays are emitted. Figure II-7 shows the photon yield as a function of time for the $^{12}C + ^{12}C$ system at E/A=40 MeV.

In the interval between t_1=15 fm/c, when the two nuclei start touching each other, and t_2= 33 fm/c when maximum overlap takes place, about 90% of the gamma rays are emitted. It is clear that in this model, high-energy gamma rays can be regarded as probes of the momentum and energy of the nucleons in the early stages of a heavy ion reaction. Figure II-8 shows the impact parameter dependence of the gamma-ray yield. A comparison with the result obtained with a simple geometrical overlap of two circles is also shown. Overall this geometrical approximation reproduces reasonable well the BUU calculated impact-parameter dependence of the high-energy gamma-ray production.

The calculated double differential cross sections reproduce well the general behavior of the experimental results (before calibration) as shown in Figure II-9. However, the magnitude of the yield is too large, and the gap between the prediction and the experimental results becomes greater with decreasing beam energy. While, after the calibration corrections, the 40 MeV data is well reproduced the 20 MeV data is still overestimated. The general behavior of the differential cross-section angular distribution is well reproduced (after calibration correction) for 40 MeV gamma rays, but for higher gamma-ray energies the predicted angular distribution is more forward peaked then the experimental one.

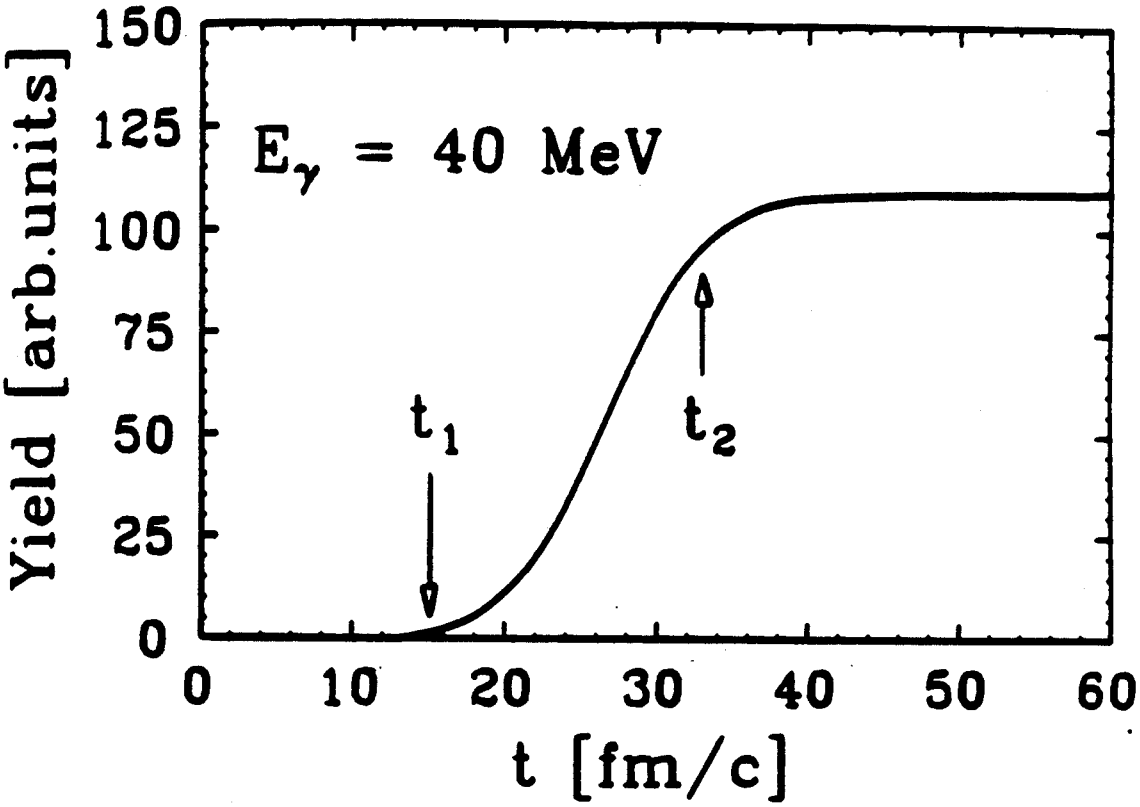

Figure II-7 BUU calculation of the photon yield as a function of time for C + C at E/A=40 MeV.

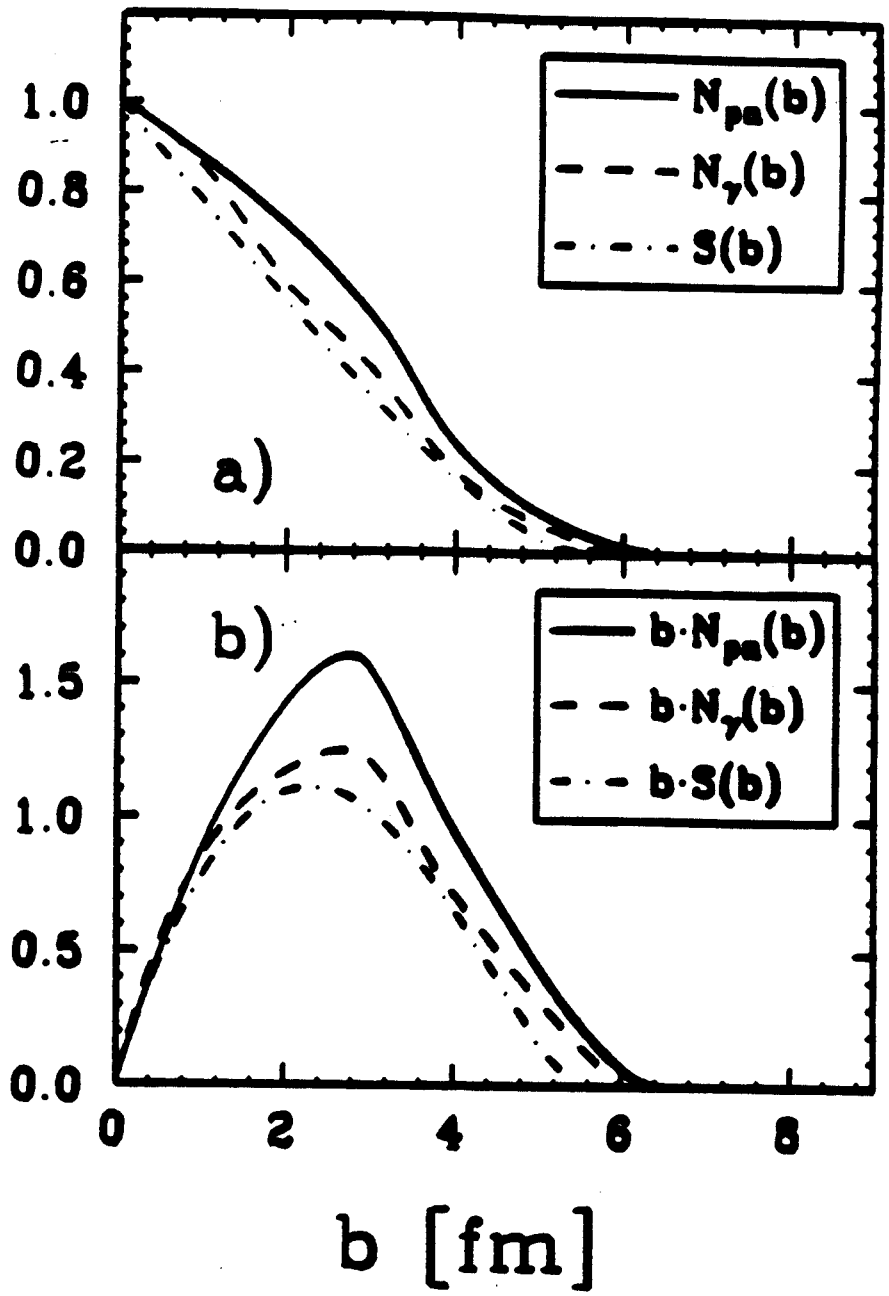

Figure II-8 BUU impact-parameter dependence of the gamma-ray yield.

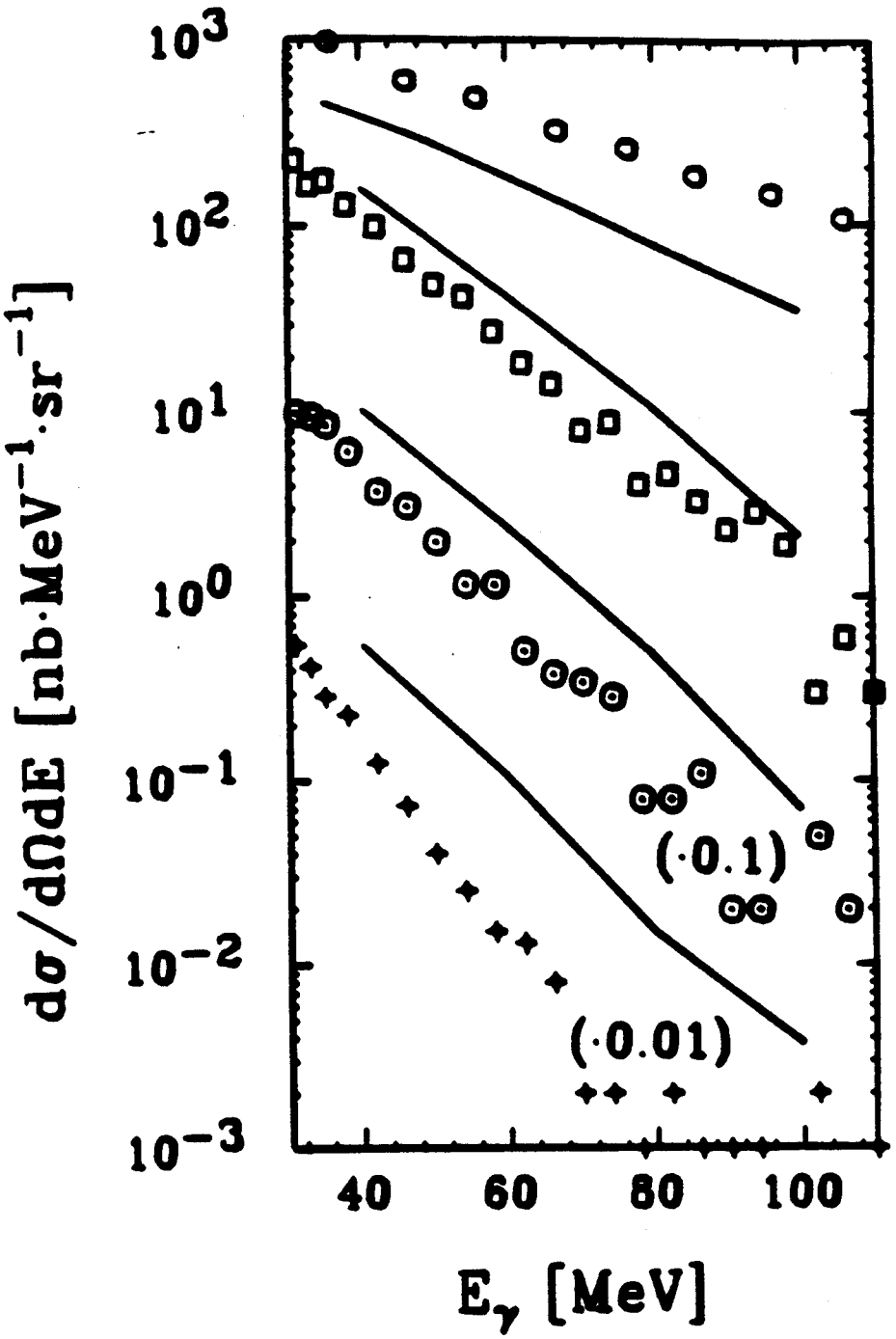

Figure II-9 Experimental $d\sigma^2/(dE\ d\Omega)$ and BUU calculations. From top to bottom: C + C at E/A=84 MeV [Gr 86] and our N + C at 40, 30 and 20 MeV/n (before calibration corrections).

In the second dynamical study, Bauer et al. [Ba 87] used a relativistic expression including the radiative corrections to the mesons ω and σ exchange in the elementary process. Figure II-10 and II-12 show the comparison between theoretical and experimental results (before calibration) both for the double differential and for the angular distribution.

2. Thermal emission

The exponential behavior of the gamma-ray spectra and the possibility of finding a reference frame in which the emission is isotropic could, on the other hand, be interpreted as a signature of a thermal process. In this picture gamma rays are produced during nucleon-nucleon collisions in a "fireball" or hot zone formed by part of the target and part of the projectile nucleons. Since the total available energy, in this case, is the sum of the hot zone nucleon energies, the high gamma-ray energies (50 - 100 MeV) can easily be obtained.

Bonasera et al. [Bo 87b] reduce the mass and the total energy of the fireball, obtained from geometrical considerations, to take in account the limitations in the number of collisions imposed by the Pauli principle. The decay rate is calculated with the Weisskopf theory. While the slopes of the gamma-ray spectra are well reproduced, the total yield is overestimated, even after calibration corrections, by at least a factor of 3.

Nifenecker et al. [Ni 85] used a Boltzmann gas of temperature T to represent the fireball. The velocities of the colliding nucleons obey

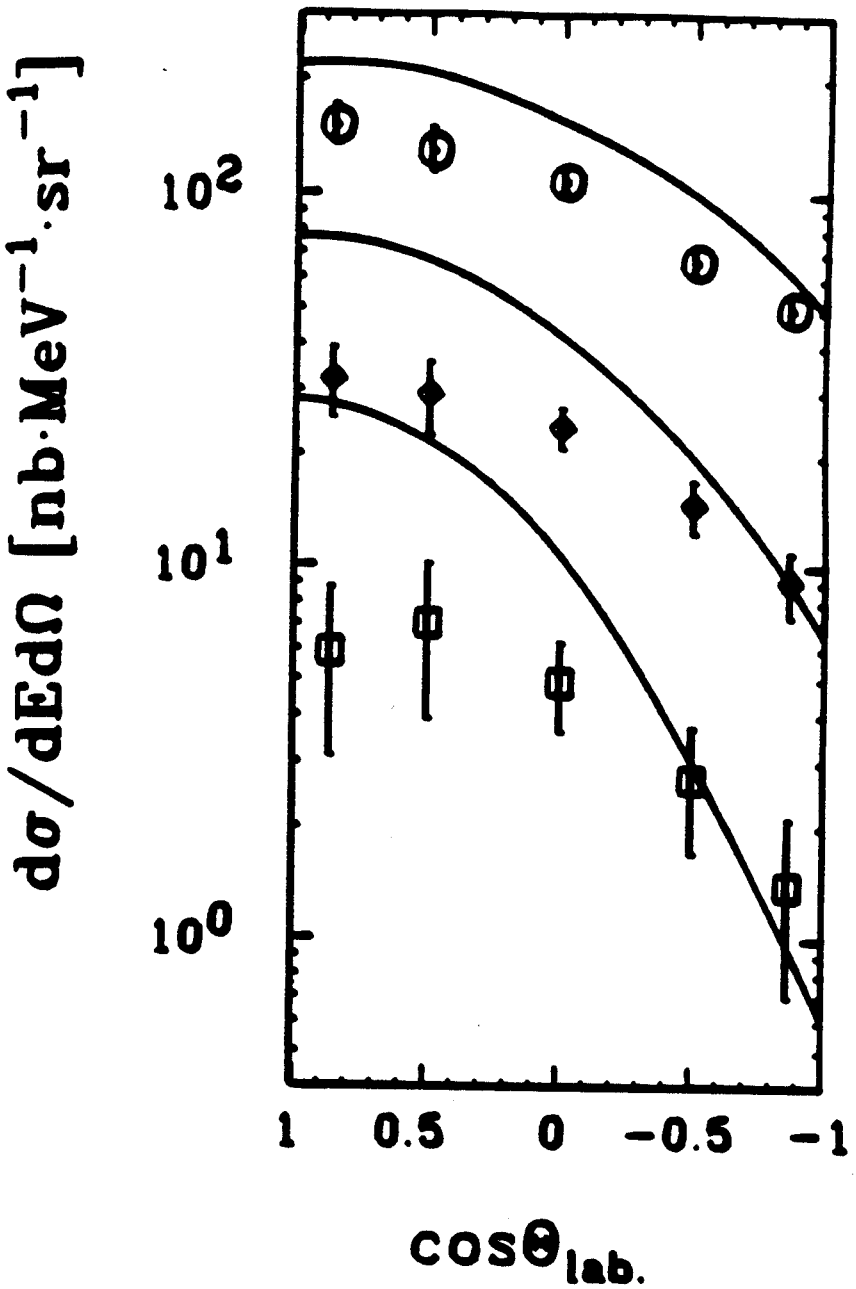

Figure II-10 BUU angular distributions as compared to our data (before calibration corrections) for N + C at E/A=40 MeV and photon energies of 40 (circles), 60 (diamonds) and 80 (squares) MeV.

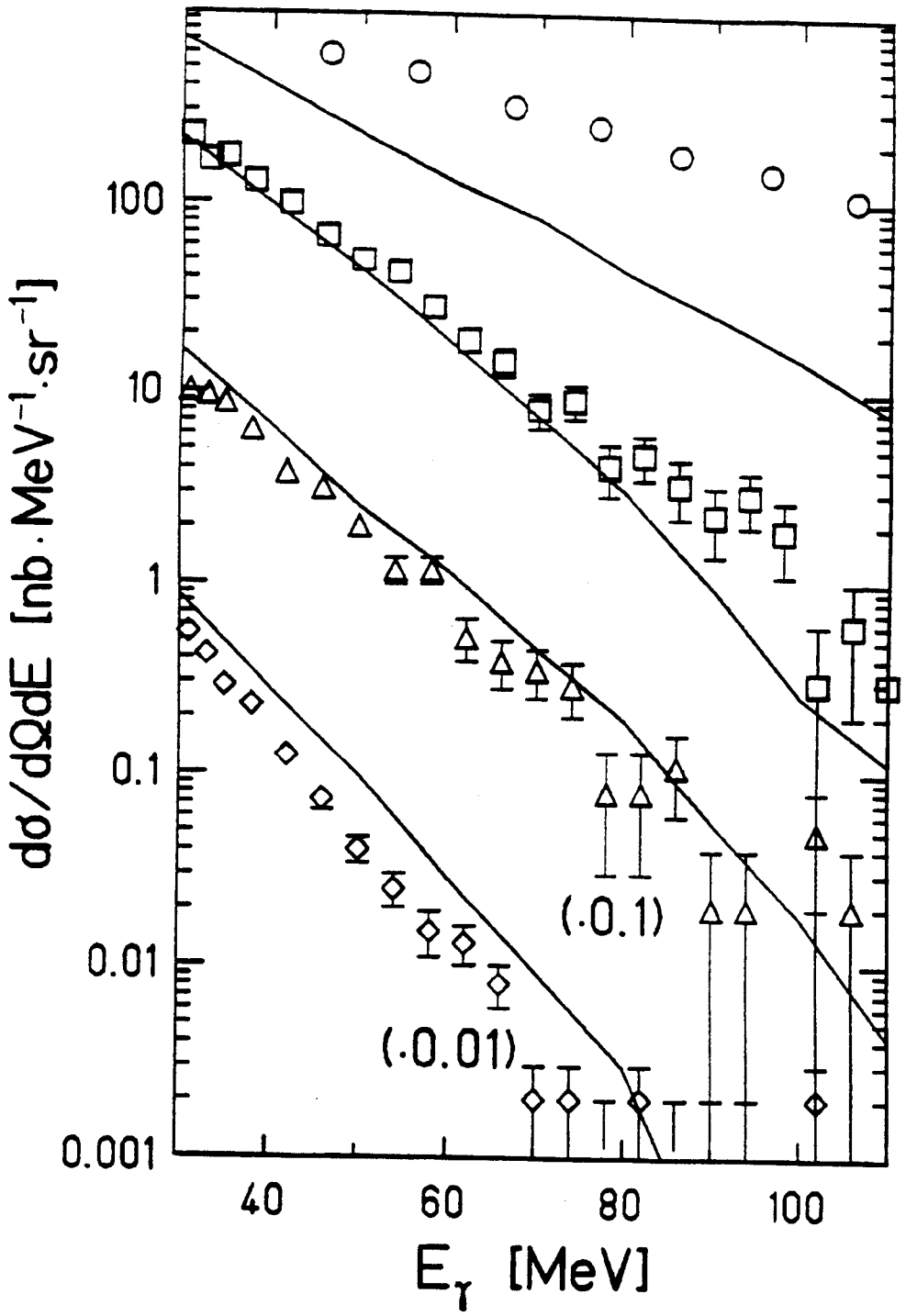

Figure II-11 Experimental $d\sigma^2/(dE\ d\Omega)$ and BUU calculations. From top to bottom: C + C at E/A=84 MeV [Gr 86] and our N + C (before calibration corrections) at E/A=40, 30 and 20 MeV.

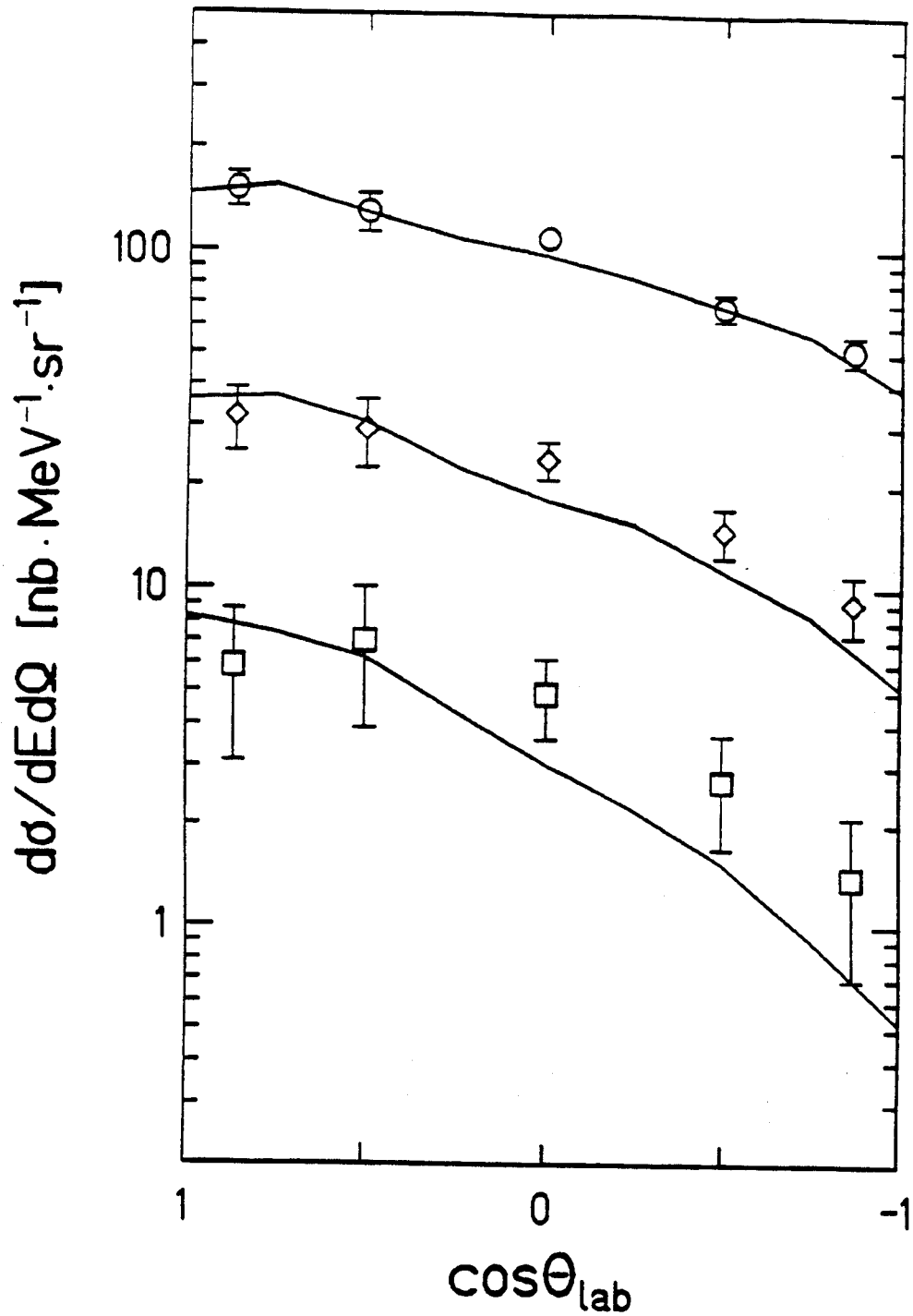

Figure II-12 BUU angular distributions as compared to our data (before calibration corrections) for N + C at E/A=40 MeV and photon energies of 40 (circles), 60 (diamonds) and 80 (squares) MeV.

Maxwell distributions, and the emitted radiation is incoherent because of the lack of correlation between nucleons in the fireball. The n-p bremsstrahlung emission is studied in the soft-photon approximation and only the portion of the spectrum $^{12}C + C$ at E/A=84 MeV below 50 Mev can be reproduced well using thermal emission as the main mechanism.

D. Neuhauser and S. E. Koonin [Ne 87] substituted the exact quantal nucleon-nucleon bremsstrahlung cross section in place of the classical soft-photon approximation. This substitution appears to modify substantially the theoretical spectrum especially at high energies. Good agreement is found for the reactions $^{14}N + Pb$ at E/A=40 MeV (before calibration) and $^{12}C + U$ at E/A=84 MeV (Figure II-13).

CHAPTER III

HIGH-ENERGY GAMMA RAY-CHARGED PARTICLE COINCIDENCE

A. EXPERIMENTAL SET-UP

In order to shed some light on the high energy gamma-ray production mechanism we performed an experiment at the National Superconducting Cyclotron Laboratory to study the coincidence between high-energy gamma rays and light (Z=1) charged particles (c.p.) emitted in the reaction:

$$^{14}N + Zn \rightarrow Y + c.p. + X \quad \text{at } E/A=40 \text{ Mev}$$

Where X is any other reaction product.

On one side of the beam, sixteen charged particle telescopes were placed outside a small aluminum vacuum chamber (Figure III-1) and viewed the target through three thin (0.254 mm) kapton windows. Fourteen of the telescopes were grouped in pairs and covered the angular range between 30° and 120°, one was positioned at 130°, and the last one was at θ=40° and ϕ=90° out of the plane. The total solid angle covered was 250 msr.

On the other side of the beam two high-energy gamma-ray telescopes were positioned, outside the chamber, at 60° and 120° each covering a solid angle of 125 msr. The vacuum chamber wall facing the high-energy gamma-ray detectors was 0.95 cm thick. The transmission coefficient for 10 MeV gamma rays is 0.9423 and 0.9413 for 60 MeV gamma rays. The experimental set-up is shown in Figure III-2. The experiment ran for ten days with about 20 enA of E/A=40 MeV ^{14}N on a 30 mg/cm^2 Zn target.

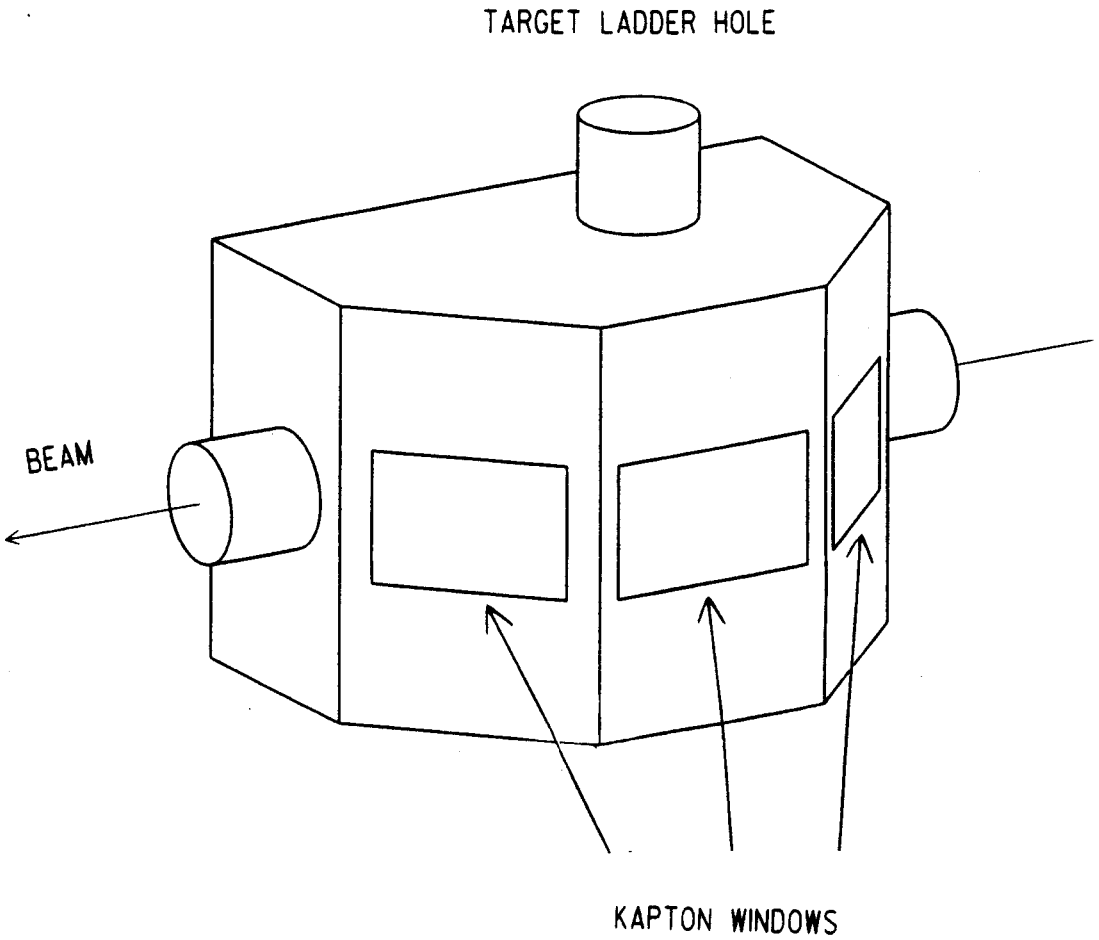

Figure III-1 Aluminium vacuum chamber.

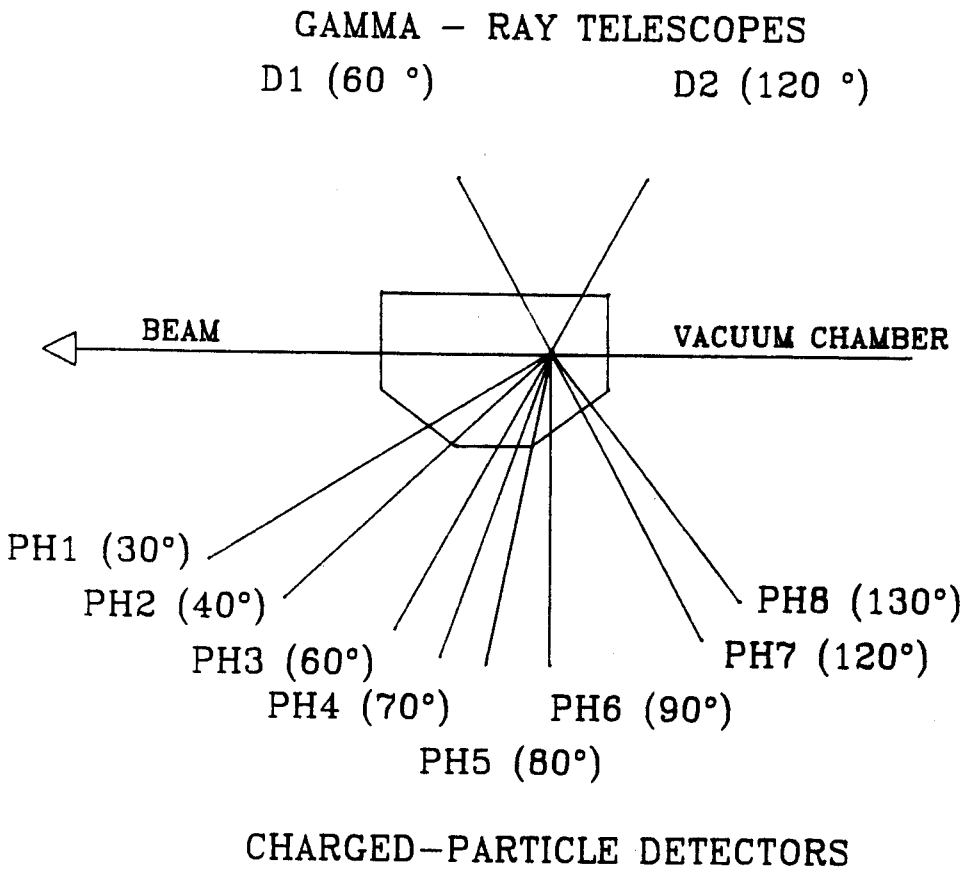

Figure III-2 Experimental set-up for the coincidence experiment.

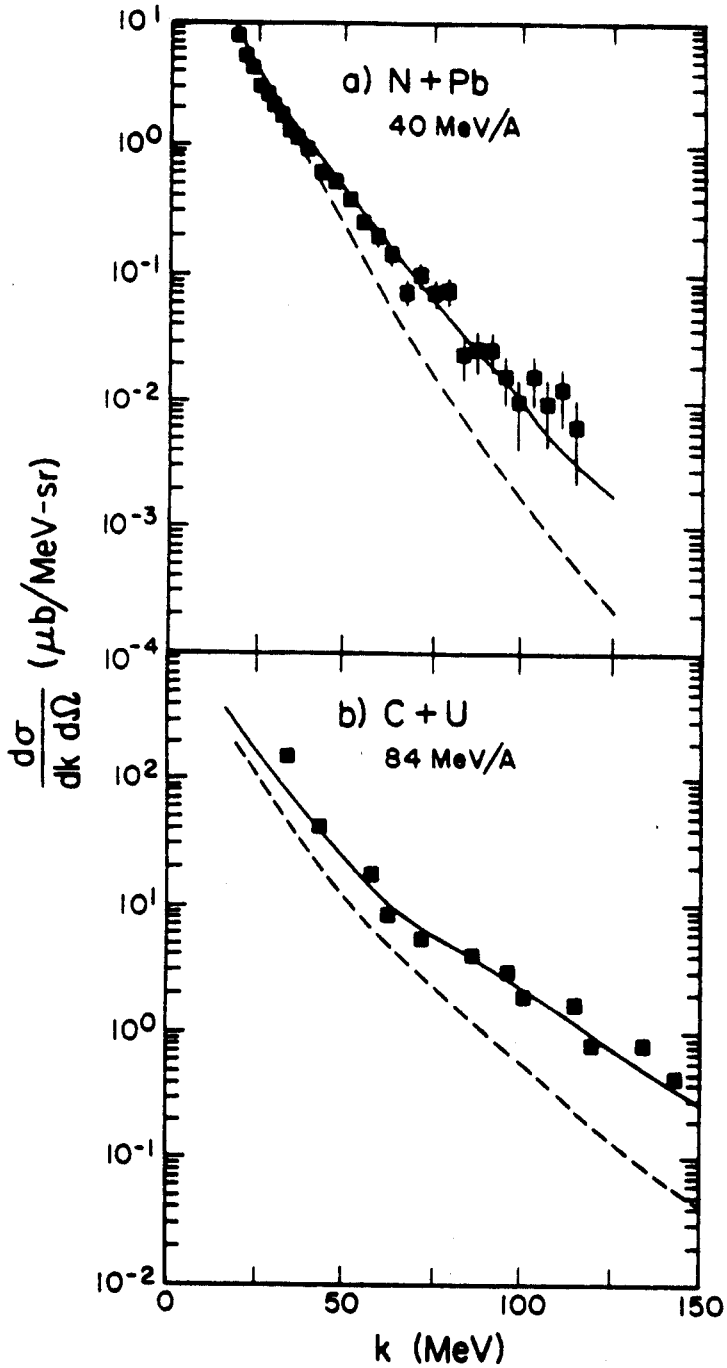

Figure II-13 Neuhauser et al. theoretical calculations compared to our C + Pb (before calibration corrections) at E/A=40 MeV and to Grosse et al. C + U at E/A=84 MeV [Gr 86].

1. ΔE-E detectors.

The charged particle ΔE-E telescopes (Figure III-3) were plastic scintillators, often called "phoswichs" (phosphorous sandwich). They consisted of a fast scintillating plastic (Bicron BC-412) 1.6 mm thick for ΔE measurements followed by a tapered 127 mm slow scintillating plastic (Bicron BC-444) for E measurements. The properties of the plastic scintillator material are reported in Table III-1.

A single photomultiplier tube (Amperex 2202), viewing the detector through the end of the E detector, could provide a ΔE and an E signal by applying a narrow time gate for the 60 ns short component and a broad gate for the 260 ns component (Figure III-4). Protons, deuterons and tritons could easily be separated. The energy range of particles detected in the telescopes is summarized in Table III-2. The different low and high energy limit for each detector is due to the different amount of target, kapton window and air crossed by charged particles detected at different angles.

2. High-energy gamma-ray detector

The high energy gamma-ray detectors used in this experiment were essentially the same ones used in the singles experiment described in chapter I. The only difference was the type of converter used. We replaced the active CsI converters with two equal 12.7 x 12.7 x 0.35 cm passive Pb converters characterized by higher efficiency (Figure III-5).

B. ELECTRONICS

Table III-1 Plastic scintillator properties.

	Fast plastic (BC-412)	Slow plastic (BC-444)
Rise time (ns)	1.0	19.
Decay time (ns)	3.3	179.7
Pulse width (FWHM ns)	4.2	171.9
Wavelength of maximum emission(nm)	434	428

MSU-87-244

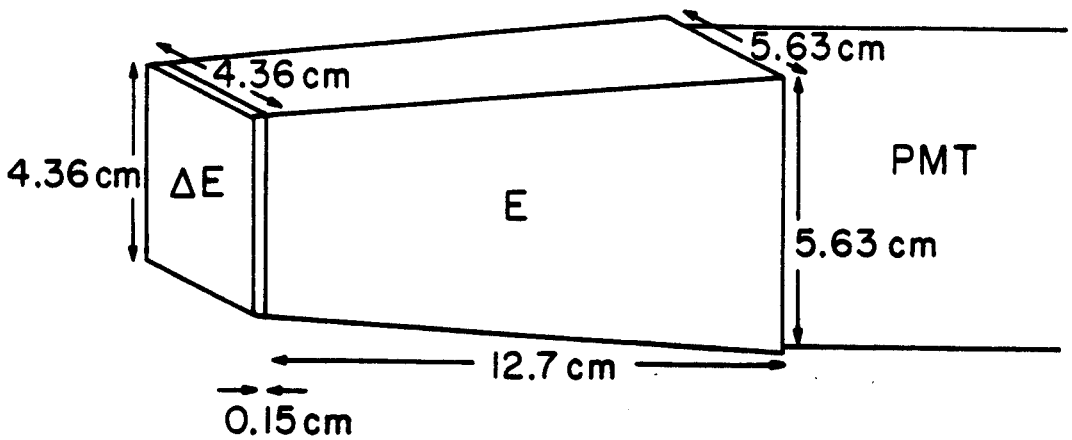

Figure III-3 Charged particle ΔE-E telescope.

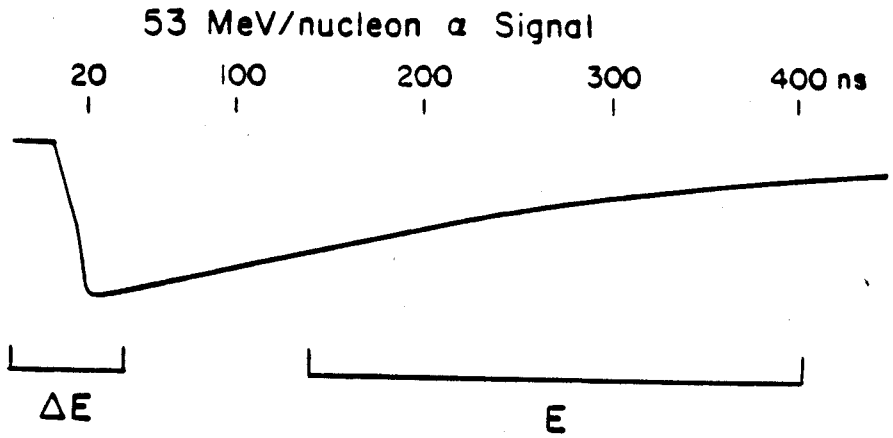

Figure III-4 Time gates for ΔE and E signal.

Table III-2 Lower and upper energy limits for charged particle detected in the ΔE-E telescopes.

DET	p		d		t	
	L(MeV)	H(MeV)	L(MeV)	H(MeV)	L(MeV)	H(MeV)
PH1	14.5	135	19.7	182	23.5	218
PH2	14.5	135	19.7	182	23.5	218
PH3	14.5	135	19.7	182	23.5	218
PH4	13.9	134	18.7	182	22.3	218
PH5	14.1	134	18.9	182	22.7	218
PH6	14.5	135	19.7	182	23.3	218
PH7	14.5	135	19.5	182	23.3	218
PH8U	14.1	134	19.1	182	22.7	218
PH8D	15.5	135	21.1	182	24.9	218

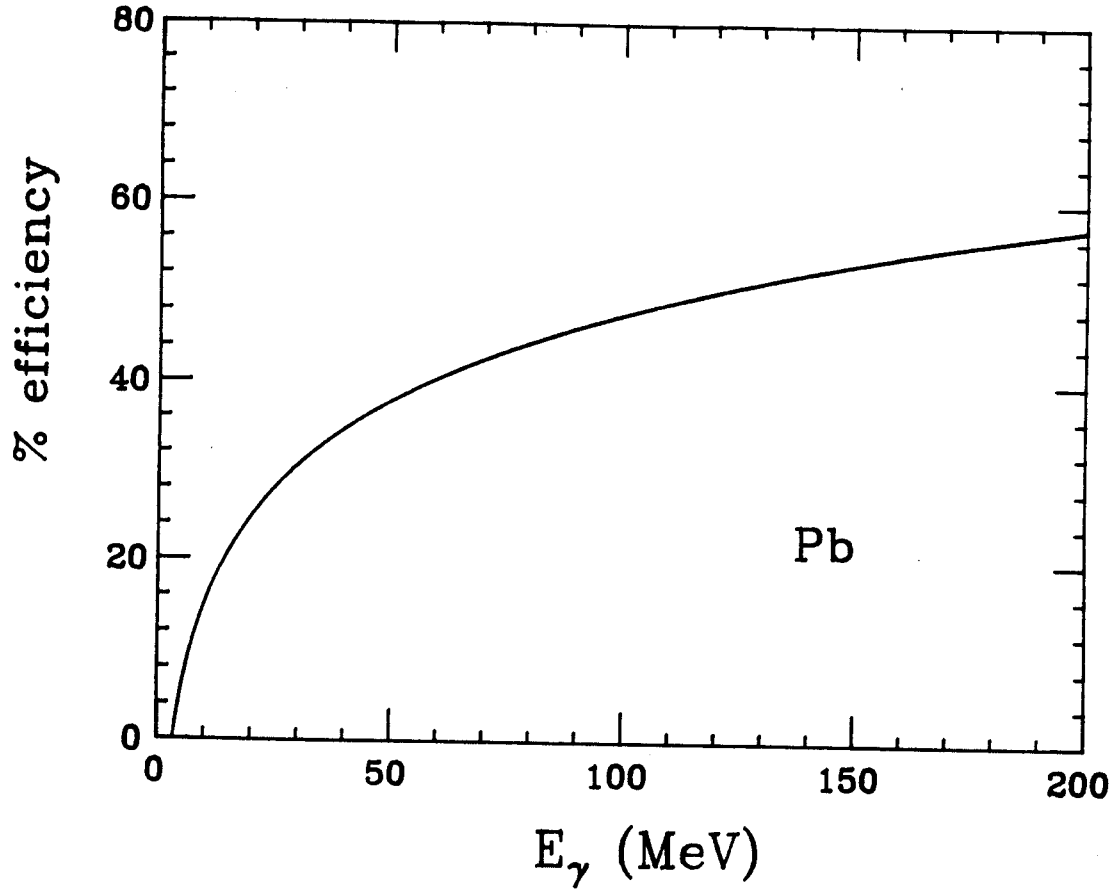

Figure III-5 Efficiency versus gamma-ray energy for Pb converter.

The electronics set-up allowed the simultaneous collection of four different types of events:

1) Gamma-ray singles taken by either one of the two gamma detectors.
2) Gamma ray-charged particle coincidence between either Cherenkov detector and any of the phoswich detectors.
3) Scaled down charged particle singles and two-fold coincidences.
4) All charged particle three fold and higher coincidences.

The scale-down factor was different for different positions in order to obtain comparable count rates: it was 1000 for the first four most forward angles (30-70°), 500 for the next two (80 and 90°) and 200 for the last two (120 and 130°).

Figure III-6 is a drawing of the logic master gate. The electronic circuit for a charged particle detector is shown in Figure III-7, and the circuit used for each high-energy gamma-ray telescope was the same as the one shown in chapter I in Figure I-2a.

C. CHARGED PARTICLE DETECTOR CALIBRATION

The energy scale of the Z=1 isotopes in the ΔE-E spectra was calibrated using a deuteron beam at E/A=53 MeV on a 19.31 mg/cm^2 Au target. Three calibration points were obtained using the elastic scattering peak and the two peaks produced by degrading the elastically scattered deuterons using Al absorbers 11 and 18 mm thick.

Before the calibration points could be used to define an energy scale it was necessary to correct the ΔE-E spectra by the so called "gamma-neutron line subtraction". For each charged particle event the

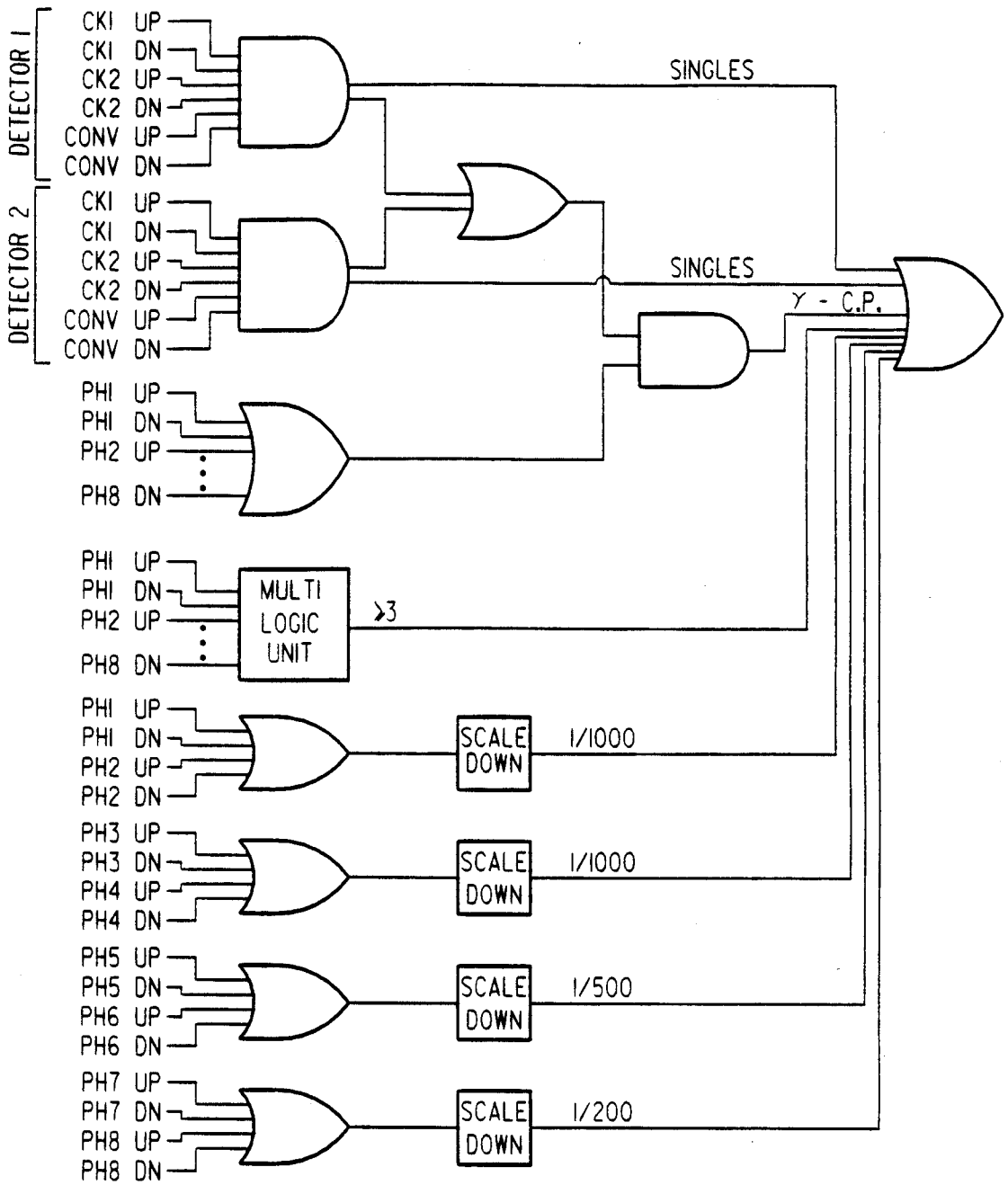

Figure III-6 Logic master gate.

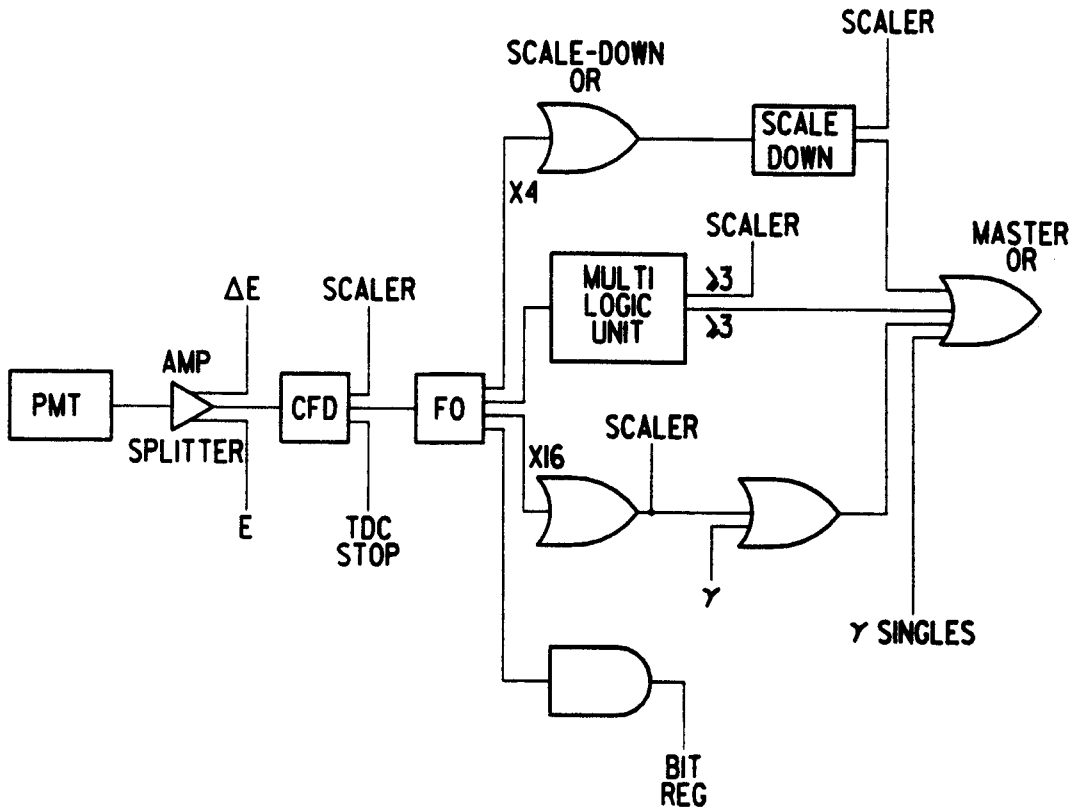

Figure III-7 Electronic circuit for a charged particle detector.

ΔE signal is always contaminated by part of the E signal causing the ΔE signal to increase with increasing energy. The data from neutron and gamma-ray events can be used to correct for the false rise due to the nature of the interaction of these uncharged particles in the detector. The interaction probability of neutrons and gamma rays in the ΔE portion is small, because it is thin, but the interaction probability of these particles in the E portion is not small. Thus, for these reactions, light only comes from the E portion of the detector and the ΔE signal is entirely due to contamination from the E signal. The ΔE-E spectrum for neutrons and gamma rays is a line beginning at the origin (the "gamma-neutron line) which represents the false rise in ΔE as a function of E. The corrected charged-particle spectra were found by taking a point by point difference between the ΔE of each charged particle event and the ordinate of a point in the "gamma-neutron line" having the same value of E. Figures III-8a and III-8b show a ΔE-E spectrum before and after the subtraction respectively.

Shown in Figures III-9a and III-9b are plots of energy versus channel number for one of the charged particle detectors. Plots are shown both for ΔE and the E part of the detector. The calibration was done both for the gamma ray-charged particle coincidence and the charged particle single trigger configuration since a difference in the timing of the two produced a slight difference in the ΔE-E spectra.

Since the plots of energy versus channel number vary from detector to detector and we desired to have a unique energy scale for all detectors, we employed the following simple rescaling process. In Figure III-10, line (a) represents an arbitrary reference line while line (b) represents a phoswich calibration line obtained by fitting the

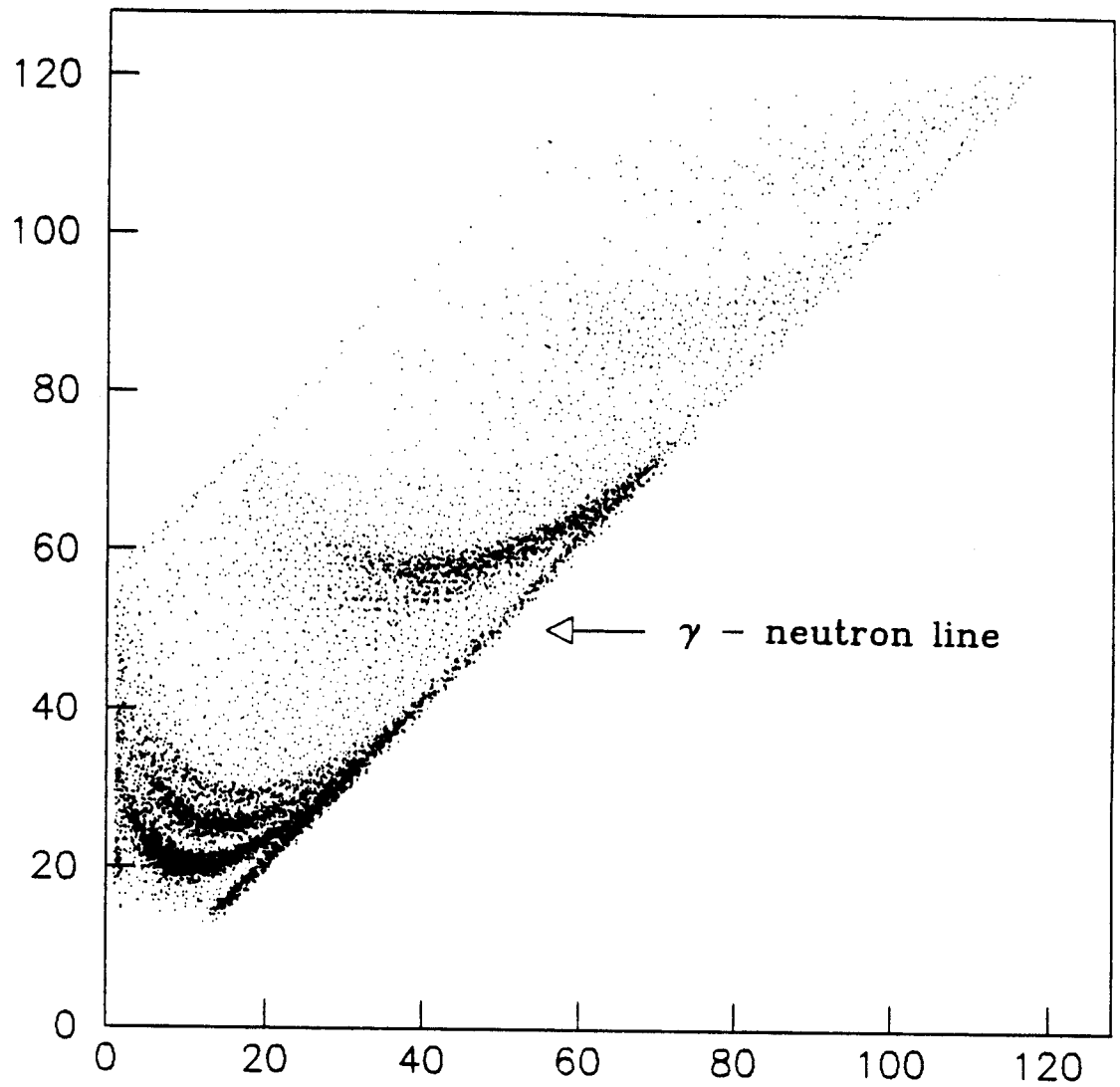

Figure III-8a Isotope lines before "gamma-neutron line" subtraction.

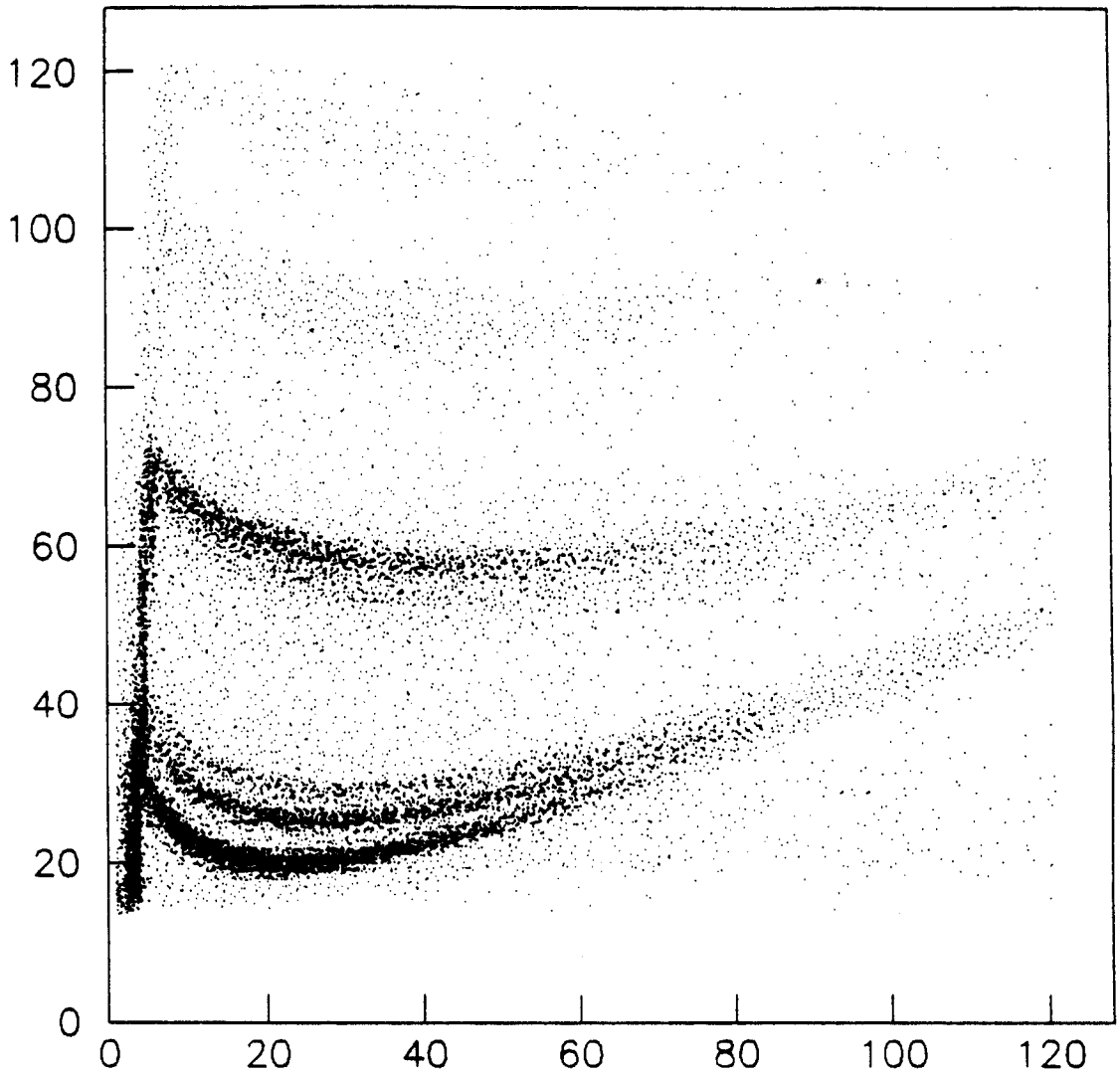

Figure III-8b Isotope lines after "gamma-neutron line" subraction.

MSU-87-245

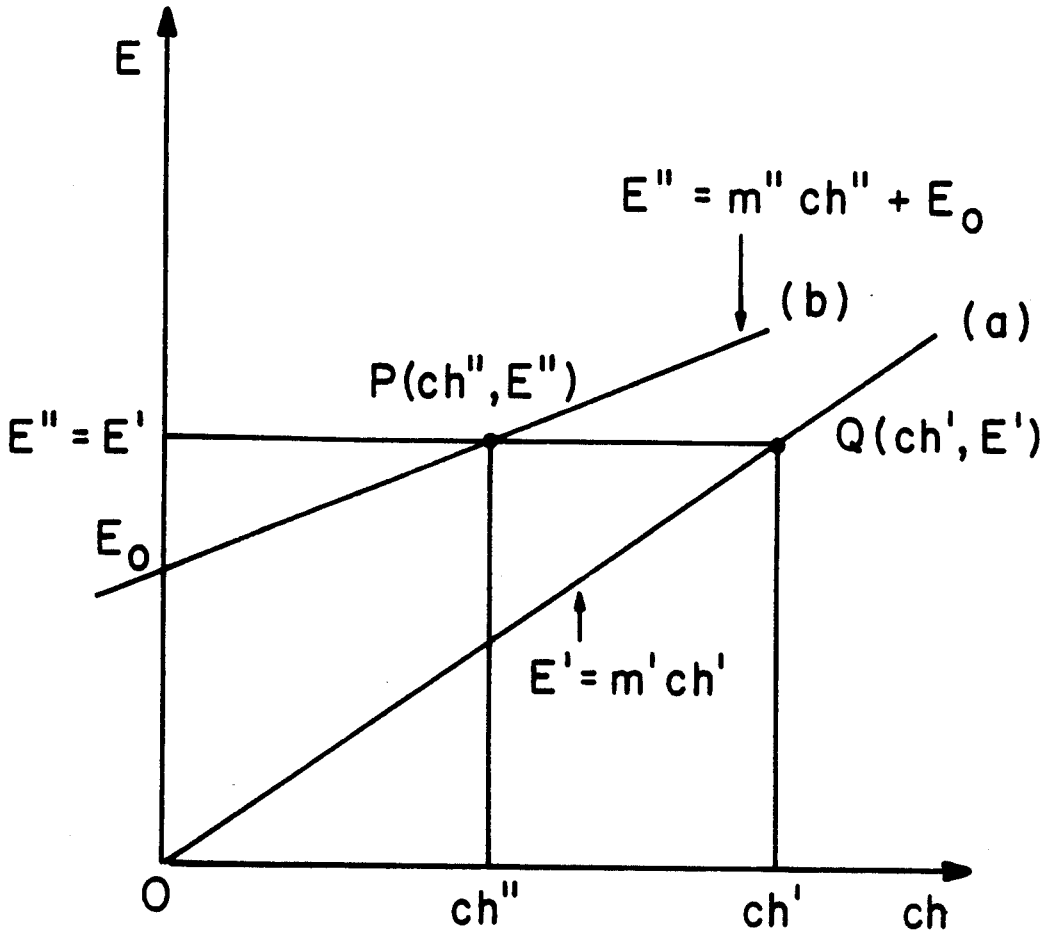

Figure III-10 Energy rescaling diagram for a charged particle detector.

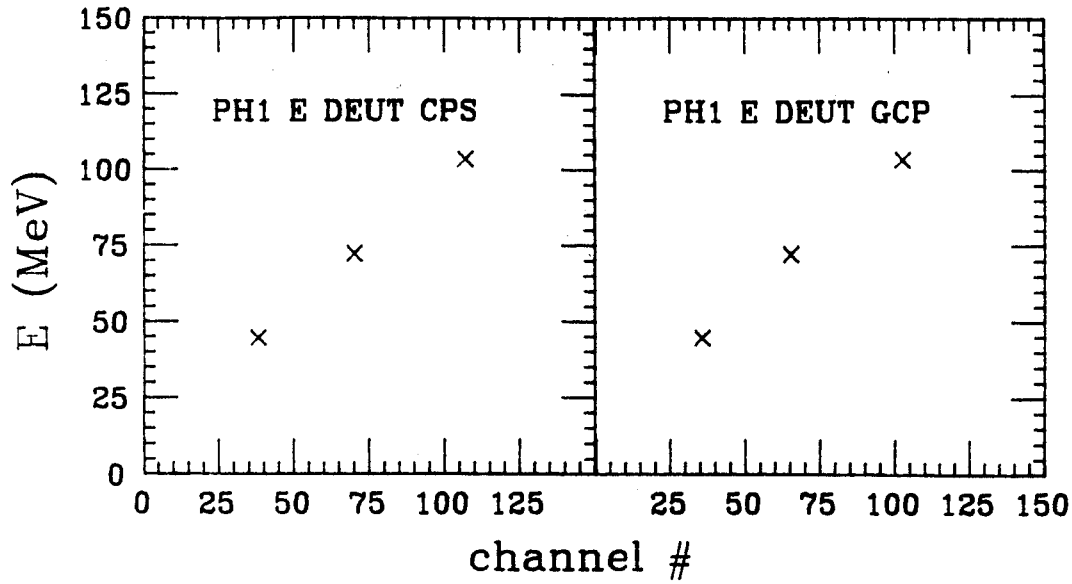

Figure III-9a E versus channel number for a charged particle detector.

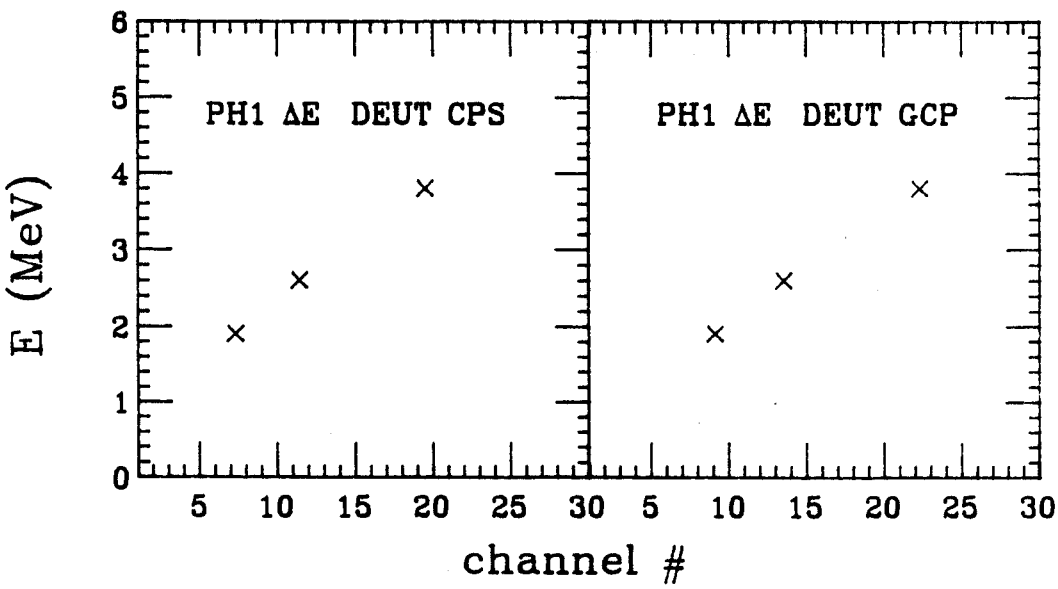

Figure III-9b ΔE versus channel number for a charged particle detector.

data points of plots similar to Figure III-9. Points P and Q have the same energy but different channel number. Equating the two energies:

III-1 $\quad E'=E'' \Rightarrow m'ch'= m''ch'' + E_o$

the new value of ch' is $ch'=m''ch''/m'+E_o/m'$. The value of m' defines the energy scale.

The kinetic energy of each charged particle was obtained by adding together the contributions, rescaled using the calibration data, of the fast ΔE component and the slow E component.

D. DATA REDUCTION

The major contamination in the high energy gamma-ray spectrum is due to cosmic muons. To reduce this background to a minimum it was required that there be: no signal out of the discriminator for the front, side and top anticoincidence shields. More restrictive conditions additionally required the pulse height in the detector shields be below a minimum value.

All 16 charged particle detectors were originally designed to be positioned 43.2 cm away from the target so that, at that distance, both the front and the back faces subtended the same solid angle (Figure III-11). In the coincidence experiment, some of the detectors were positioned at much smaller distances (Table III-3) creating problems with particles escaping from the sides (Figure III-12). Since the E portion of the signal for the escaping particles is smaller than the one obtained for a completely contained particle, the point representing the

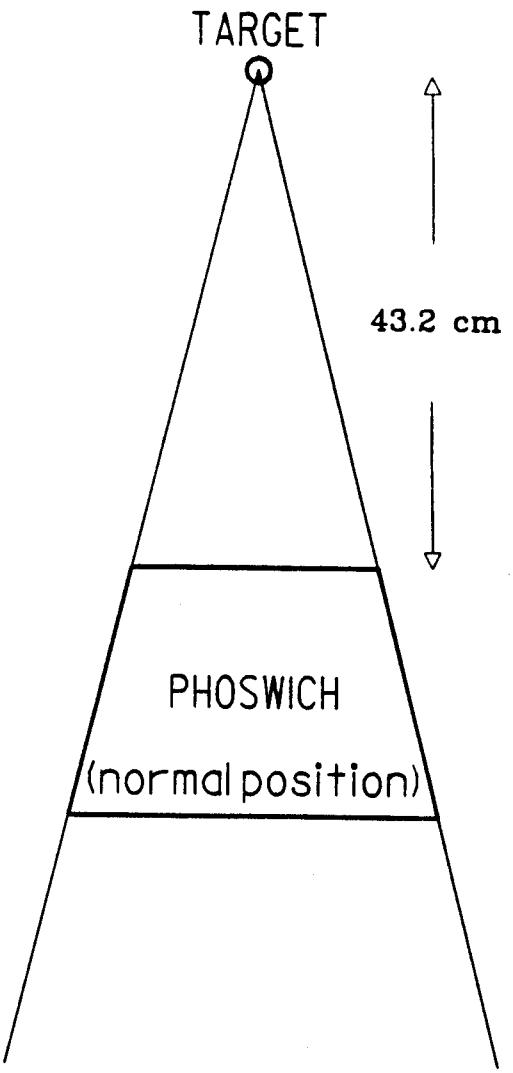

Figure III-11 Charged-particle detector: normal position.

Table III-3. Angular position, distance and solid angle covered for each charged particle detector.

DETECTOR	ANGLE θ (°)	SOLID ANGLE(msr)	DISTANCE FROM TARGET(cm)
PH1U	31.3	5.150	61.03
PH1D	31.3	5.150	61.03
PH2U	42.3	5.116	61.24
PH2D	42.3	5.116	61.24
PH3U	61.0	15.962	34.67
PH3D	61.0	15.962	34.67
PH4U	72.6	20.653	30.48
PH4D	72.6	20.653	30.48
PH5U	81.5	20.350	30.71
PH5D	81.5	20.350	30.71
PH6U	91.0	21.110	30.15
PH6D	91.0	21.110	30.15
PH7U	122.0	22.800	29.00
PH7D	122.0	22.800	29.00
PH8U	131.9	22.250	29.36
PH8D	40.0	4.200	67.56
	φ=90		

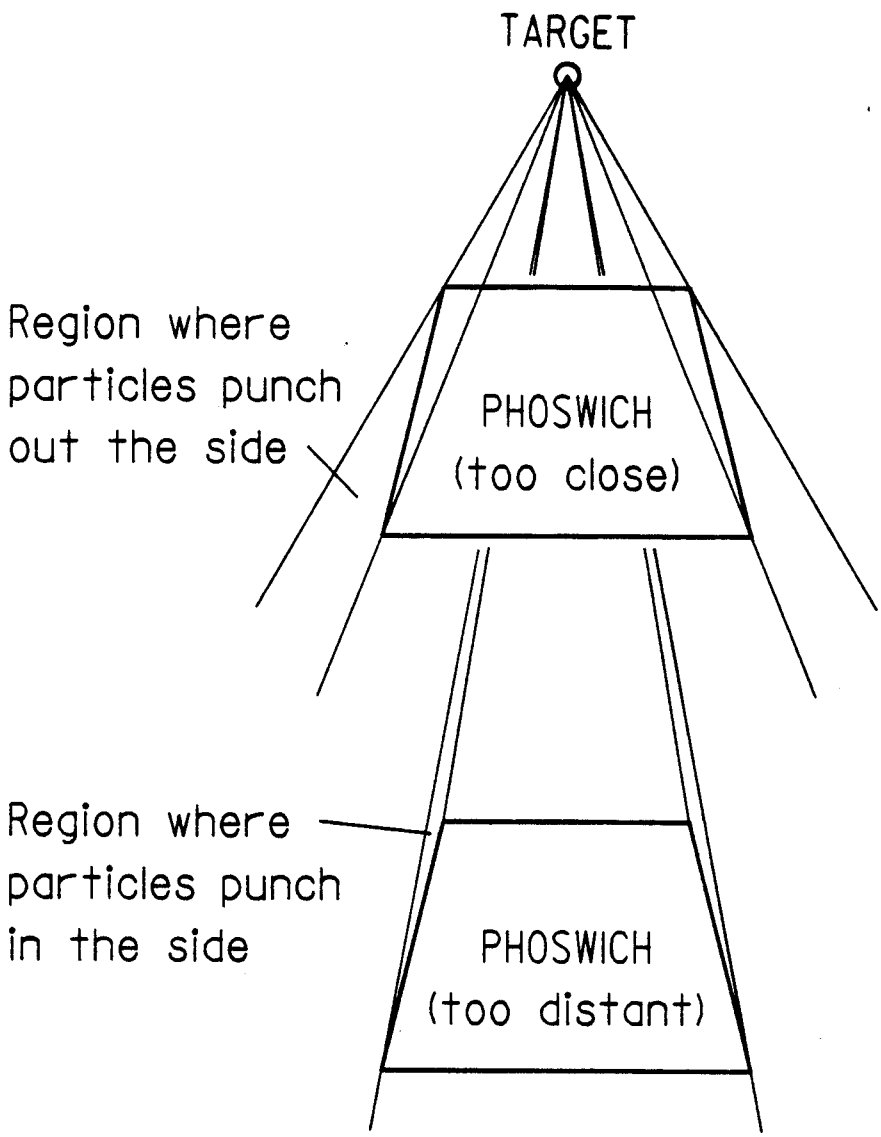

Figure III-12 Charged-particle detector: closer and farther.

particle in ΔE-E plot, is shifted to the left of the correct isotope line. The overall effect is that the covered solid angle is then determined by the back face of the detector. Other detectors sat farther away, allowing a particle to enter from the side and miss the ΔE portion of the detector (Figure III-12). These events look like neutron events since the ΔE signal will always be a fraction of the E signal as explained above and will therefore be rejected in the analysis. One of the charged particle detectors at 80° failed before the calibration and the data from it were never included in the results.

Gates were drawn on the ΔE-E plots to separate particles with different mass and charge. Separate sets of gates were drawn for charged particle singles and for charged particles in coincidence with high-energy gamma rays because of the spectral difference caused by the different electronic timing. The coincidence between a gamma ray and a charged particle was defined by drawing a gate on a two dimensional time plot of the first Cherenkov element versus each phoswich.

E. RESULTS

1. Ratios.

A comparison of the spectra for high-energy gamma-ray singles at 60° and for high-energy gamma rays at 60° in coincidence with protons at 30° or at 70° did not show any strong features (Figure III-13). The comparison of the spectra for proton singles at 30° and protons at 30° in coincidence with gamma rays at 60° (Figure III-14) also failed to indicate any marked difference in the coincidence data. The energy

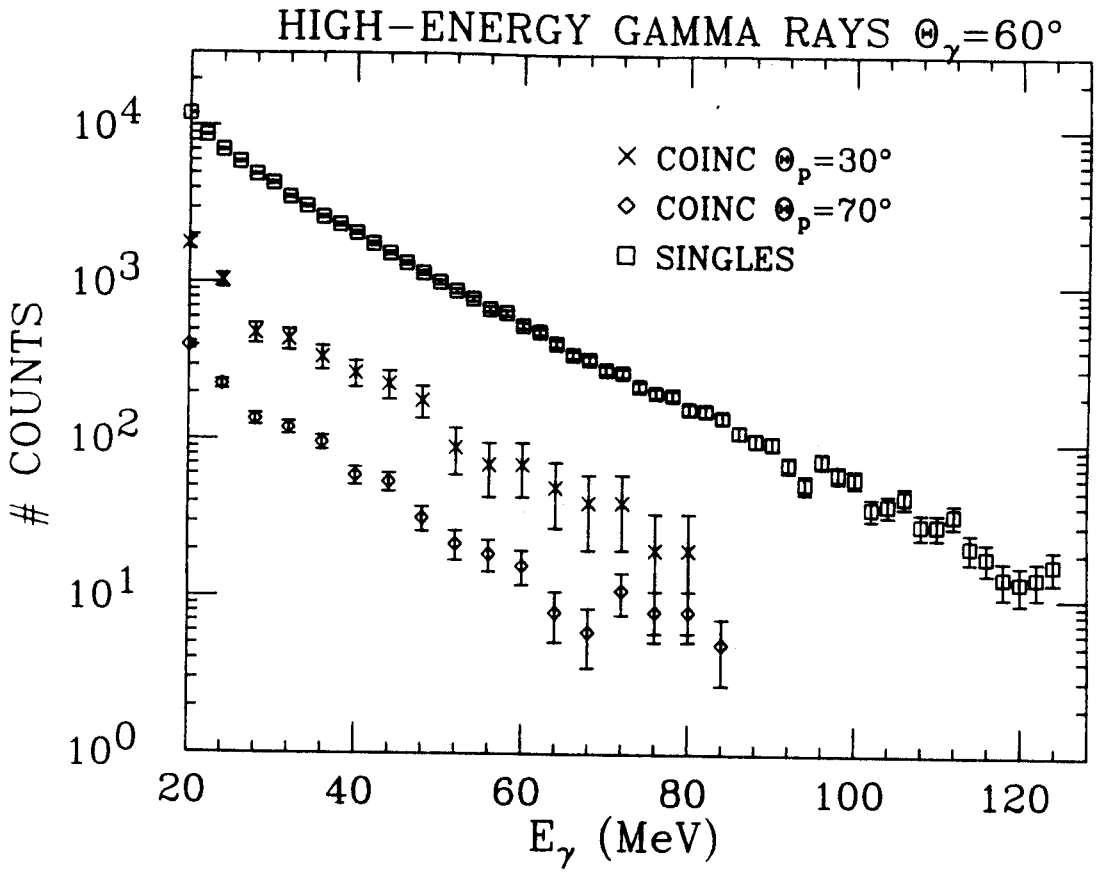

Figure III-13 Gamma ray singles at 60° and gamma rays at 60° in coincidence with protons at 30° or at 70°.

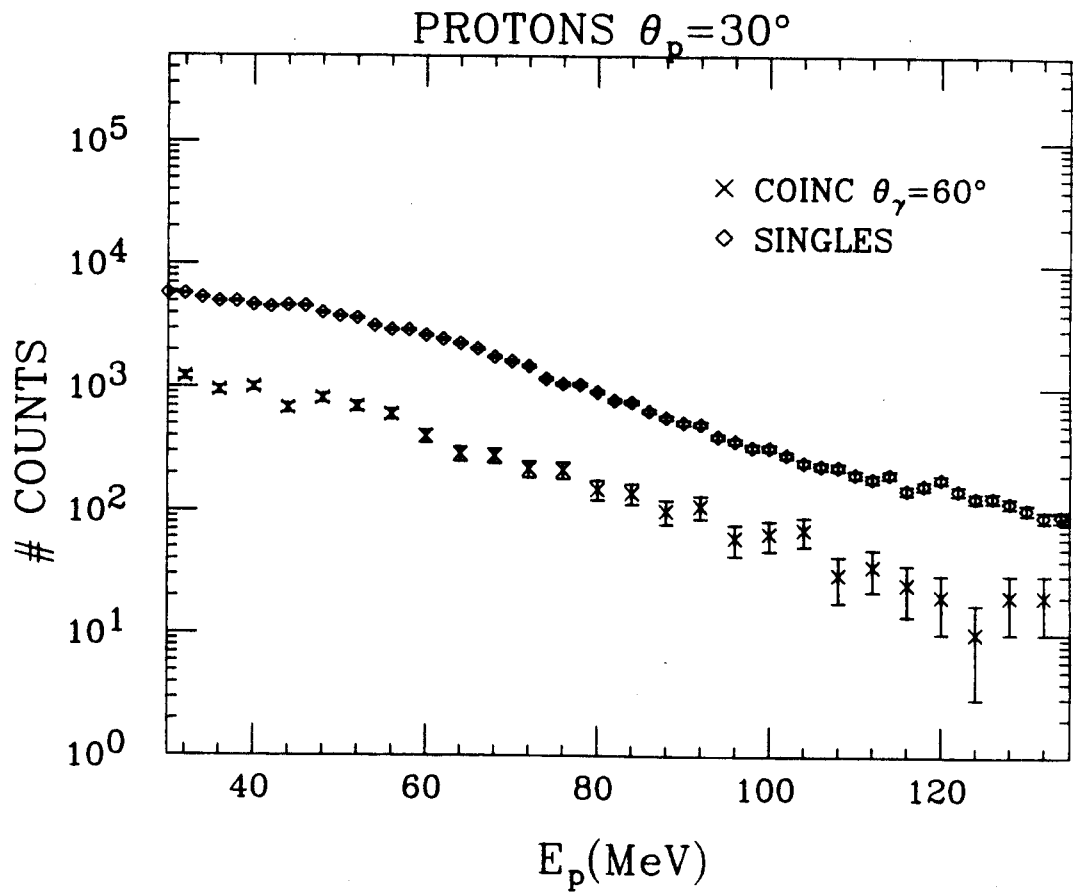

Figure III-14 Proton singles at 30° and protons at 30° in coincidence with gamma rays at 60°.

integrated angular distributions for the two sets of events also showed the same overall behavior as a function of angle (Figure III-15). This comparisons are only qualitative since the solid angles used are the ones determined by the frontal ΔE surface while for phoswichs at a distance smaller than 43.2 cm, because of the scattering out of the particles, the physical solid angle can be up to 25% smaller. A more careful examination of the data seemed to be necessary to uncover small differences. To do so we studied the ratio of the coincidence cross section to the product of the singles cross-sections. The energy integrated angular distribution of the ratio defined in equation III-2

$$\text{III-2} \qquad R(\theta_p) = \frac{\sigma_{\gamma p}}{\sigma_\gamma \ \sigma_p} \qquad \text{where} \qquad \sigma_{\gamma p} = \frac{d^2\sigma}{d\Omega_\gamma d\Omega_p} \ ,$$

$$\sigma_\gamma = \frac{d\sigma}{d\Omega_\gamma} \ , \qquad \sigma_p = \frac{d\sigma}{d\Omega_p} \ .$$

is shown in Figure III-16 for coincidence with Detector 1 (at 60°) and in Figure III-17 for coincidence with Detector 2 (at 120°). The energy range is 20-128 MeV for gamma rays and 30-135 MeV protons. The uncertainties are assumed to be statistical in origin and they are calculated using the quadrature method. For both gamma-ray detectors the ratio is fairly constant with a mean value of 0.6 $barn^{-1}$.

The values of the ratio $R(\theta_p)$ obtained for the out-of-plane phoswich at $\phi=90°, \theta=40°$ are compared in Table III-4 to the values obtained for the corresponding in plane phoswich at $\phi=0°, \theta=40°$. While for coincidences with D2(120°) the two values agree within error bars in

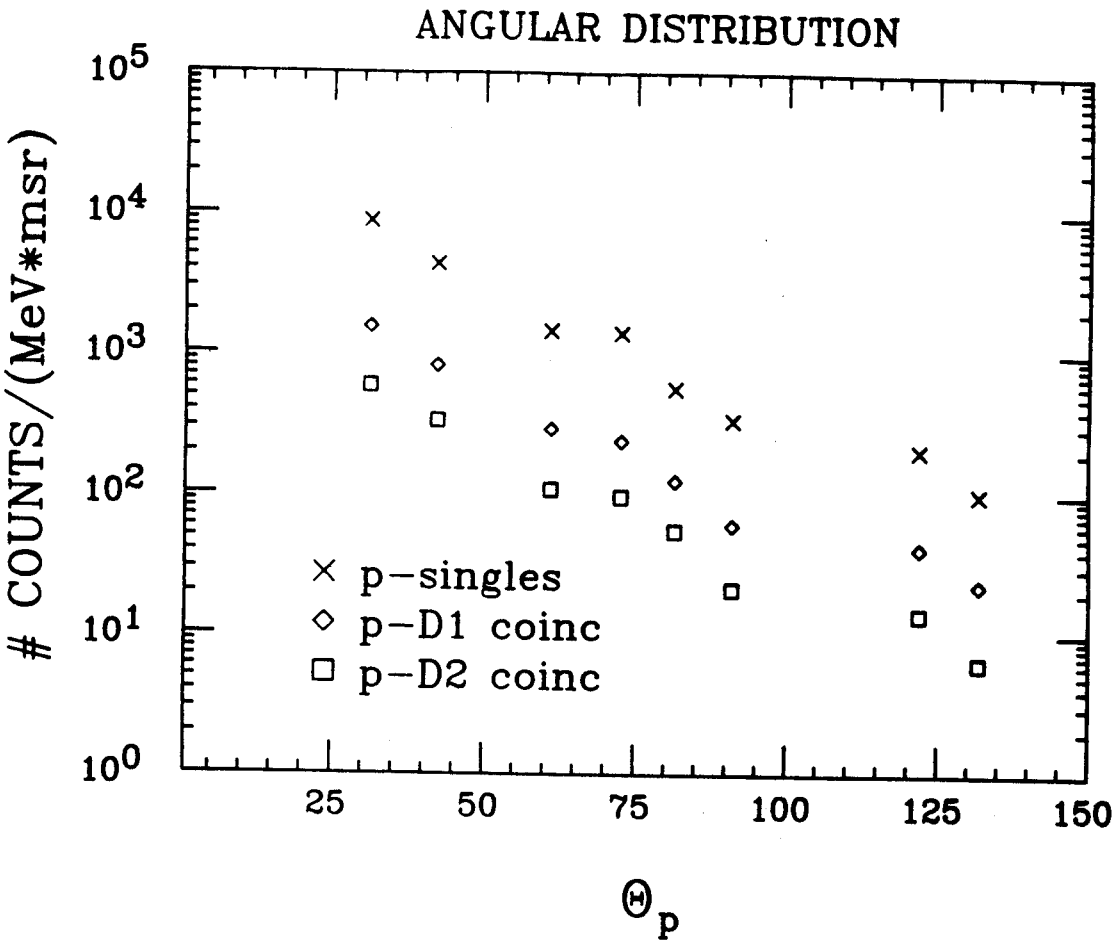

Figure III-15 Energy-integrated angular-distributions: proton singles and protons in coincidence with gamma rays at 60°.

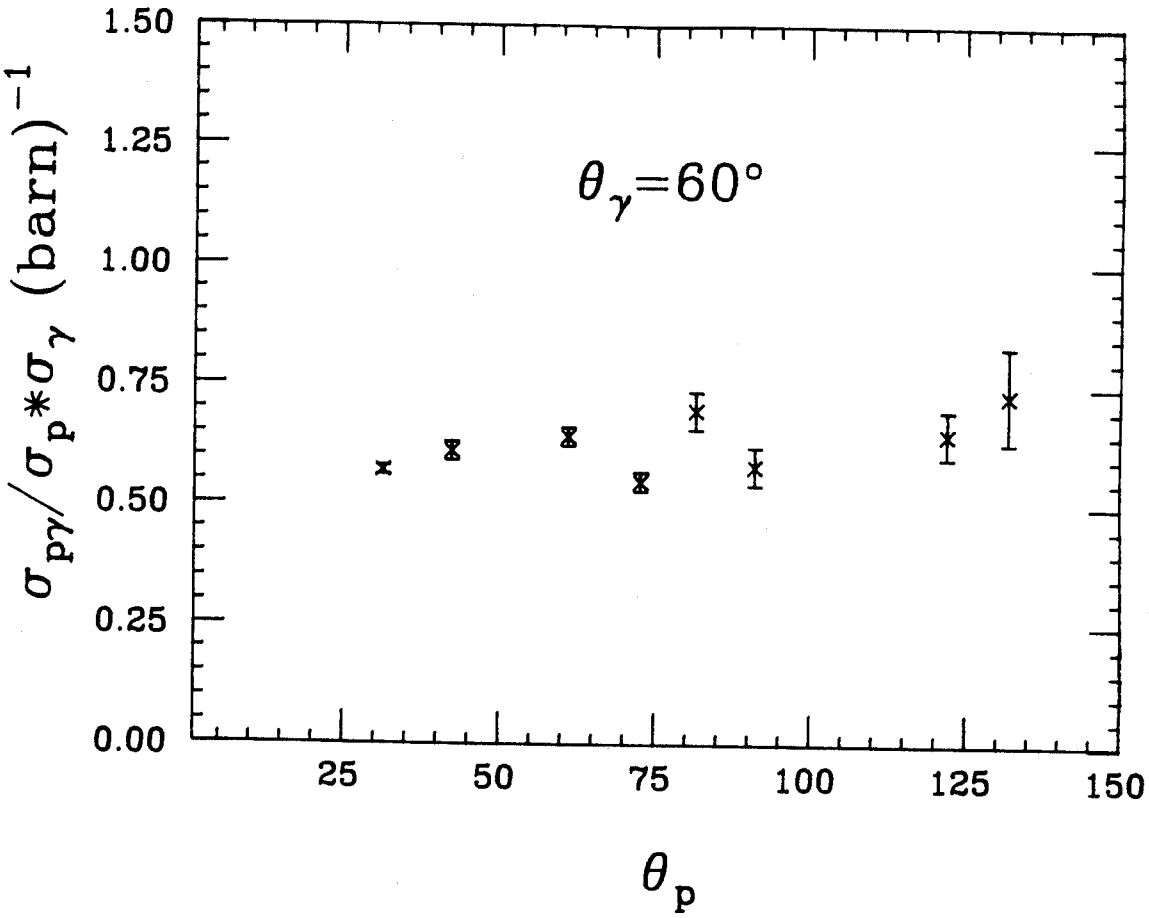

Figure III-16 Ratio versus Θ_p for gamma rays at 60°.

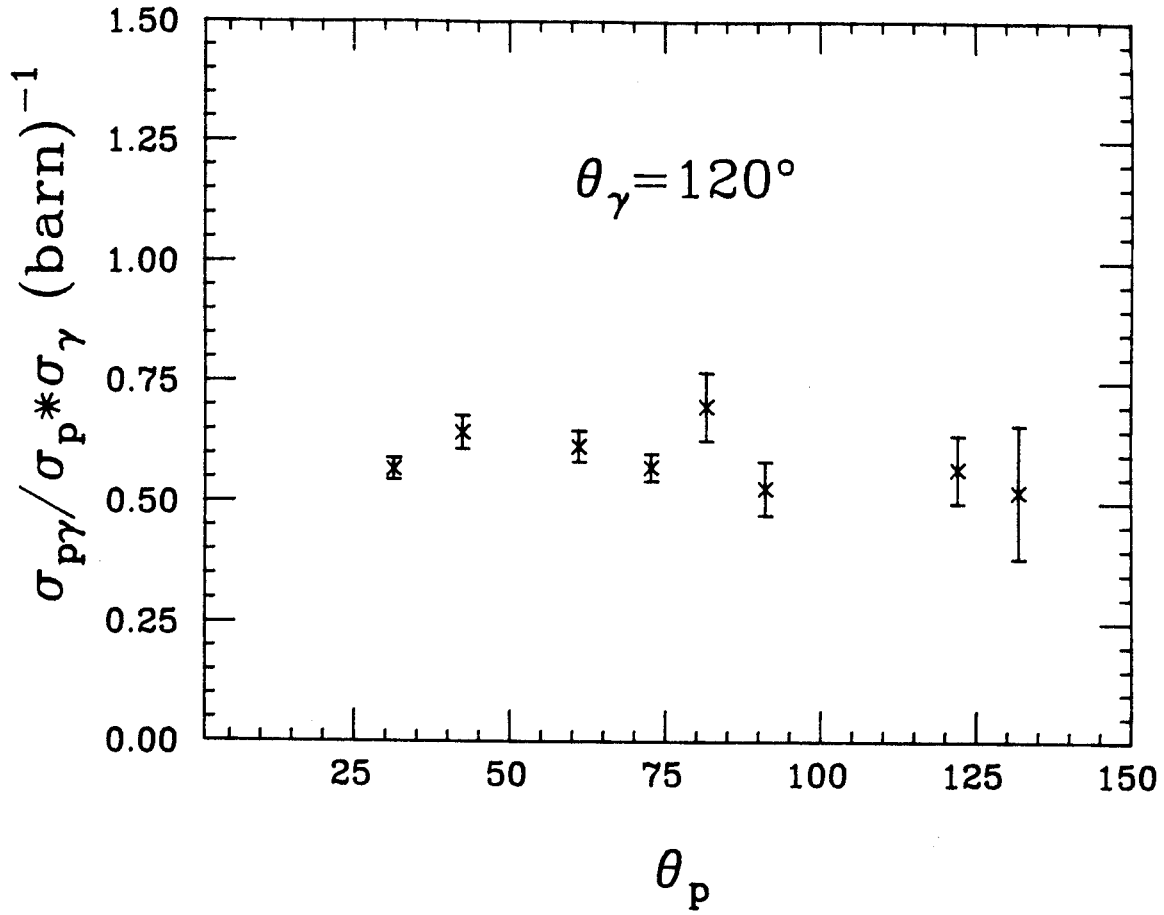

Figure III-17 Ratio versus Θ_p for gamma rays at 120°.

Table III-4. Comparison of $R(\theta_p)$ values for the out-of-plane and the in-plane phoswich at $\theta=40°$.

	$R(\theta_p)$ $\theta_\gamma=60°$	$R(\theta_p)$ $\theta_\gamma=120°$
$\theta=40°$, $\phi=0°$	0.61 ± 0.02	0.64 ± 0.04
$\theta=40°$, $\phi=90°$	0.51 ± 0.03	0.57 ± 0.05

the case of coincidences with D1(60°) the difference between the two is approximately two standard deviations.

To study the proton energy dependence, the ratio $R(E_p)$ was defined as

$$\text{III-4} \qquad R(E_p) = \frac{\sigma_{\gamma p}(E_p)}{\sigma_\gamma \quad \sigma_p(E_p)} \qquad \text{where} \qquad \sigma_{\gamma p} = \frac{d^3\sigma}{d\Omega_\gamma dE_p d\Omega_p} ,$$

$$\sigma_p = \frac{d^2\sigma}{d\Omega_p dE_p} \qquad \sigma_\gamma = \frac{d\sigma}{d\Omega_\gamma} .$$

Figure III-18 shows the ratio R calculated at four angles: 30, 40, 60 and 70°. Again R is basically constant with a value of 0.6 $barn^{-1}$. The ratio at back angles could not be calculated because of inadequate statistics.

To study the gamma-ray energy dependence of the ratio we used a thermal source parameterization of the proton spectra both for the singles and for the coincidence case. The proton source velocities are listed in Table III-5. The ratio as a function of gamma ray energy was studied in the laboratory frame for proton energies integrated above four different lower values. The lower values of the proton energy corresponded to energies of 30, 40, 50 and 60 MeV in a source frame moving with velocity β=0.142c. The ratio $R(E_\gamma)$, as function of gamma-ray energy is

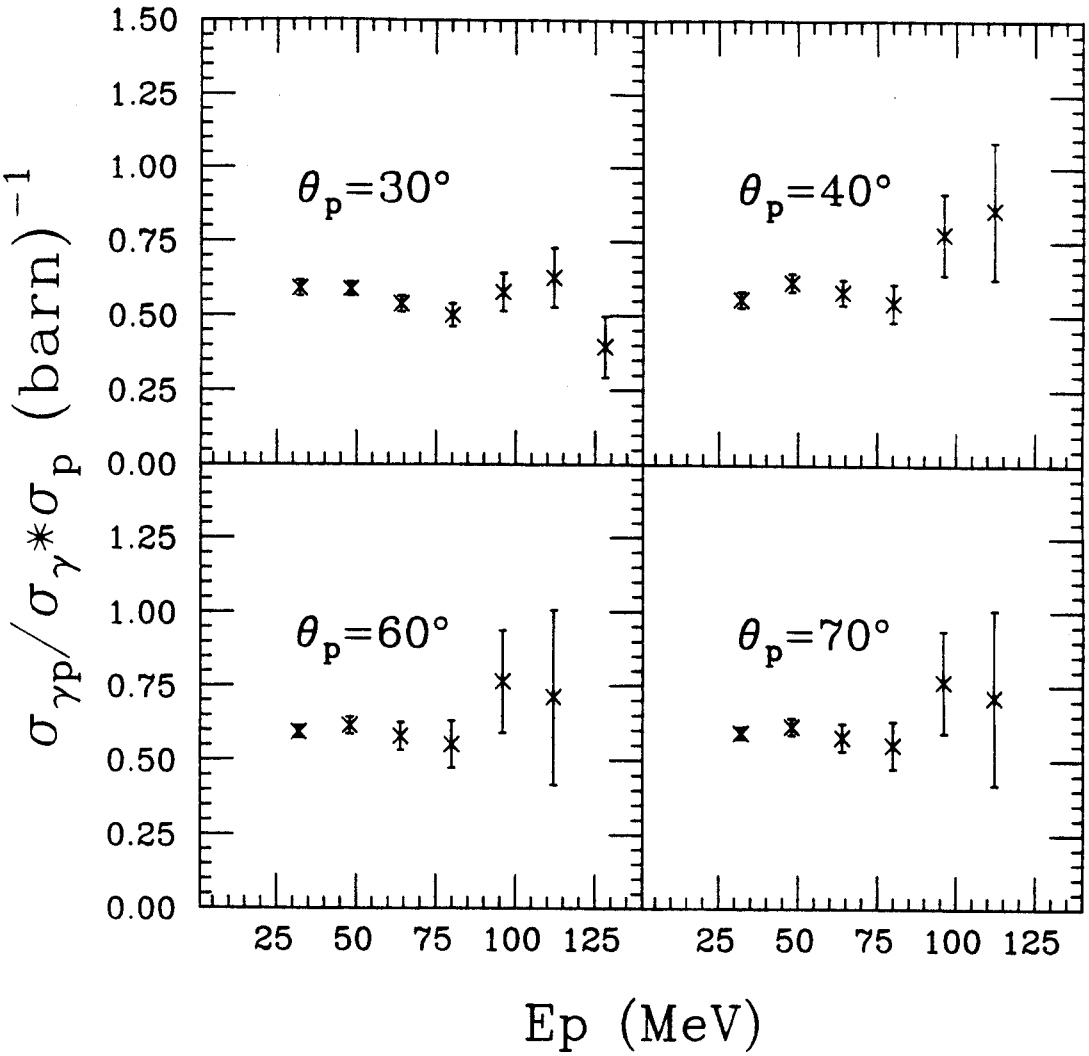

Figure III-18 Ratio versus E_p for protons at: 30, 40, 60 and 70°.

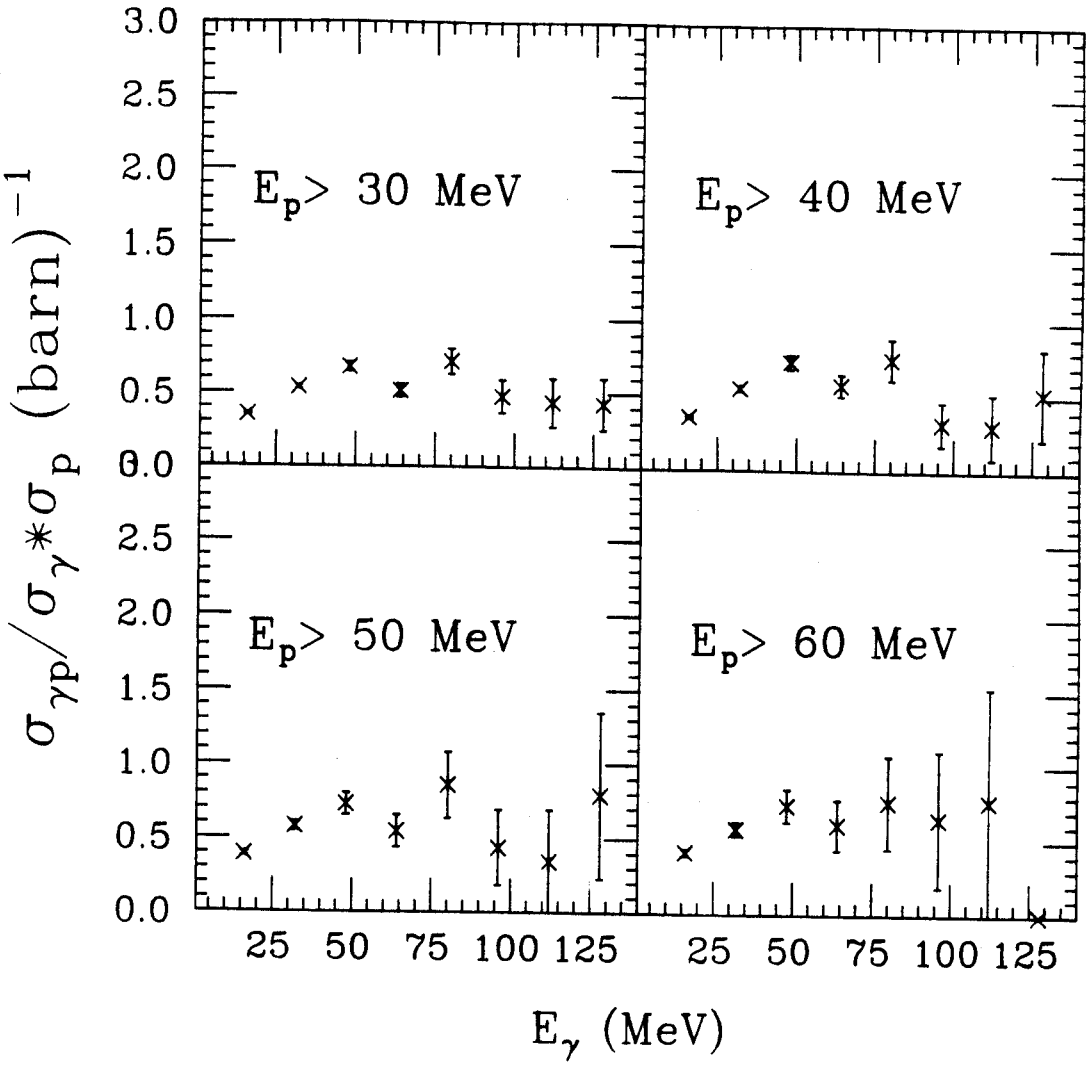

Figure III-19 Ratio versus E_γ for E_p> 30, 40, 50 or 60 MeV in a reference frame moving with velocity equal to β=0.14.

Table III-5. Proton source velocities.

	β=v/c
proton singles	0.145
proton in coincidence with D1	0.140
proton in coincidence with D2	0.135

III-5 $$R(E_\gamma) = \frac{\sigma_{\gamma p}(E_\gamma)}{\sigma_p \quad \sigma_\gamma(E_\gamma)} \qquad \text{where} \qquad \sigma_{\gamma p} = \frac{d^3\sigma}{d\Omega_\gamma dE_\gamma d\Omega_p}\Big|_{E_p \geq E_p^*},$$

$$\sigma_\gamma = \frac{d^2\sigma}{d\Omega_\gamma dE_\gamma}, \qquad \sigma_p = \frac{d\sigma}{d\Omega_p}\Big|_{E_p \geq E_p^*}$$

and $E_p^* \geq$ 30, 40, 50 or 60 MeV.

The results are shown in Figure III-19. Within experimental errors no gamma-ray energy dependence is seen in the value of the ratio for energies above 25 MeV. For energies around 20 MeV, where gamma rays are strongly associated with the giant dipole resonance, the value of the ratio $R(E_\gamma)$ is smaller which indicates a less likely coincidence.

2. Multiplicity.

A specific parameter was constructed to count how many phoswichs registered a charged particle in each event. The value of this parameter defined the event multiplicity for our experimental geometry. Because the phoswich 5UP was not calibrated, and phoswich 8DN was out of plane, the total number of detectors used in determining the multiplicity was 14. The total solid angle covered was 224 msr. The gamma ray - charged particle multiplicity parameter was incremented if the following conditions were satisfied for a given phoswich:

1) On a 2-dimensional TDC plot of the phoswich versus the first element of the gamma-ray detector positioned at 60°, the event under consideration was inside the proper coincidence gate.
2) The gamma ray had an energy equal to or greater than 20 MeV.
3) The charged particle was a Z=1 isotope.
4) The Z=1 isotope had an energy equal to or greater than 30 MeV.

An event with a gamma ray of energy equal to or above 20 MeV but with no Z=1 isotope satisfying the above conditions was counted as multiplicity 0. The gamma - charged particle multiplicity M histogram is shown in Figure III-20. The number of counts and the uncertainties (purely statistical errors) are listed in Table III-6.

Because of the complexity of the master gate, the charged particle - charged particle multiplicity was by far more difficult to obtain than the previous multiplicity. All the charged particle events with multiplicity less than three were scaled down by various factors depending upon the detector position. The number of counts in the multiplicity-one bin was the result of the sum over all detectors of the number of events with multiplicity one for each phoswich, PH_k, multiplied by the appropriate scale-down factor n_k. The total multiplicity-one datum can then be written as

$$\text{III-4} \qquad \sum_{k=1}^{14} \#\text{counts } PH_k = \sum_{k=1}^{14} \#\text{counts recorded } PH_K \cdot n_k$$

An event was accepted in any given phoswich if it represented a Z=1 isotope with energy above or equal to 30 MeV, had correct timing and no other Z=1 isotope was registered in the other phoswichs.

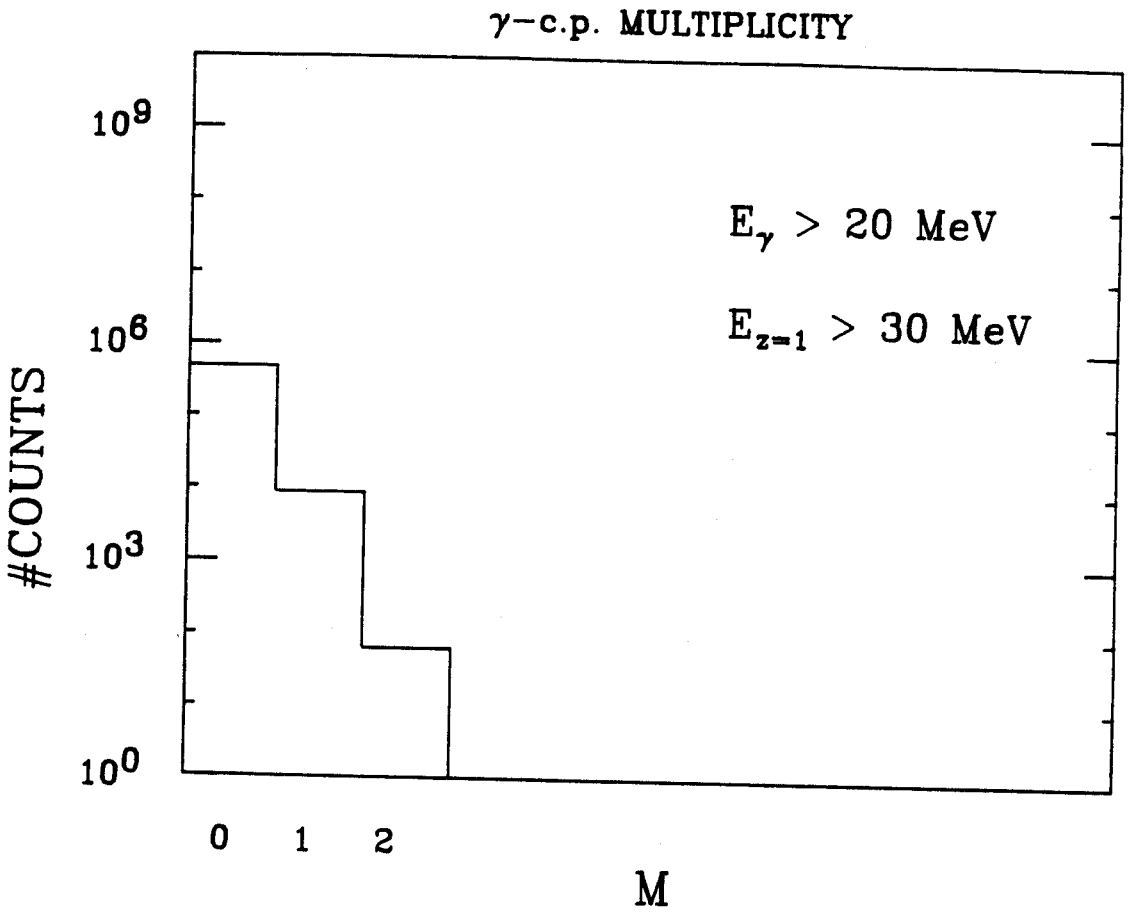

Figure III-20 Multiplicity of charged particles in coincidence with gamma rays at 60° (Y-cp).

is reduced to the solid angle covered by the remaining 13 detectors. In order to be able to directly compare the Y-c.p. with c.p.-c.p. coincidence counts, we normalized the c.p.-c.p. data to the same solid angle as for the Y-c.p. data by multiplying the the number of coincidences, $\sum_{\substack{l=1 \\ l=k}}^{14}$ #coinc. $PH_k PH_l$, by the factor in equation III-12. $\Delta\Omega_k$ is the solid angle covered by phoswich PH_k.

III-12 $$\frac{\sum_{I=1}^{14} \Delta\Omega_I}{\sum_{I=1}^{14} \Delta\Omega_I - \Delta\Omega_k} .$$

The total multiplicity-two datum is then the sum of 182 contributions and can be written as

III-13 $$\sum_{k=1}^{14} \left[\sum_{\substack{l=1 \\ l=k}}^{14} \#\ \text{coinc.}\ PH_k PH_l \left(\frac{\sum_{J=1}^{14} \Delta\Omega_J}{\sum_{j=1}^{14} \Delta\Omega_j - \Delta\Omega_k} \right) \right].$$

Both the statistical error and the error introduced by the scale-down factors are considered in the determination of the total uncertainty for the multiplicity-two datum given by equation III-14. The compound scale-down factor for the pair of phoswichs PH_k and PH_l is indicated as sc_{kl} .

III-16 $$\sum_{\substack{i>j \\ i=j \\ i=k}}^{14}\ \sum_{j=1}^{14}\ \sum_{k=1}^{14} PH_k PH_j PH_i = 3\left(\sum_{\substack{i=j \\ i=k}}^{14}\ \sum_{j=1}^{14}\ \sum_{k=1}^{14} PH_k PH_j PH_i\right)$$

A further correction is necessary to take in account the smaller solid angle available in the c.p.-c.p. case then in the Y-c.p. case. For the coincidence $PH_k PH_j PH_i$ the correct factor would be

III-17 $$\frac{\sum_{k=1}^{14}\Delta\Omega_k}{\sum_{k=1}^{14}\Delta\Omega_l - \Delta\Omega_i}\ \frac{\sum_{i=k}^{14}\Delta\Omega_i}{\sum_{i=k}^{14}\Delta\Omega_i - \Delta\Omega_j}$$ with j=i and j=k.

but since the detailed angular information is lost the mean correction factor used was:

III-18 $$\frac{14}{13}\ \frac{13}{12}.$$

Following the same kind of reasoning the correction factor for the recorded multiplicity-four datum was:

III-19 $$4\ \frac{14}{13}\ \frac{13}{12}\ \frac{12}{11}.$$

The charged particle - charged particle multiplicity M, is shown in Figure III-21. The number of counts and the uncertainties are listed in Table III-6.

$$\text{III-14}\qquad \left\{\sum_{k=1}^{14}\left(\frac{\sum_{j=1}^{14}\Delta\Omega_j}{\sum_{j=1}^{14}\Delta\Omega_j - \Delta\Omega_k}\right)\sum_{\substack{l=1\\ l\neq k}}^{14}\left[\#\ \text{coinc.}PH_kPH_l\text{recorded} + 0.5\right]\cdot sc_{kl}\right\}$$

$$\pm\left\{\sum_{k=1}^{14}\left(\frac{\sum_{j=1}^{14}\Delta\Omega_j}{\sum_{j=1}^{14}\Delta\Omega_j - \Delta\Omega_k}\right)\sum_{\substack{l=1\\ l\neq k}}^{14}\left\{\left((sc_{kl})^2\frac{1}{4}\right. + \left[\left(\#\ \text{coinc.}PH_kPH_l\text{recorded} + 0.5\right)\cdot sc_{kl}\right]^{1/2}\right\}.$$

The physical solid angle, for phoswichs positioned at distances closer than 43.2 cm., is somewhat smaller than the solid angle determined by the front of the detector and bigger than the one determined by the back of it. In Table IV-6 are reported both the upper and the lower limit of the multiplicity calculated for the two cases.

Multiplicity three and above were not scaled down and thus were obtained in the same fashion as in the gamma - charged particle multiplicity, incrementing the multiplicity parameter when the time, isotope and energy requirements were met. The uncertainty for multiplicities equal to or above three is simply the statistical error.

The recorded multiplicity-three datum is the sum of all different three-fold combinations of the 14 phoswichs

$$\text{III-15}\qquad \sum_{\substack{i=j\\ i=k}}^{14}\sum_{\substack{j=1\\ j=k}}^{14}\sum_{k=1}^{14} PH_kPH_jPH_i.$$

The needed multiplicity-three datum is given, though, by the left-hand side of equation III-16.

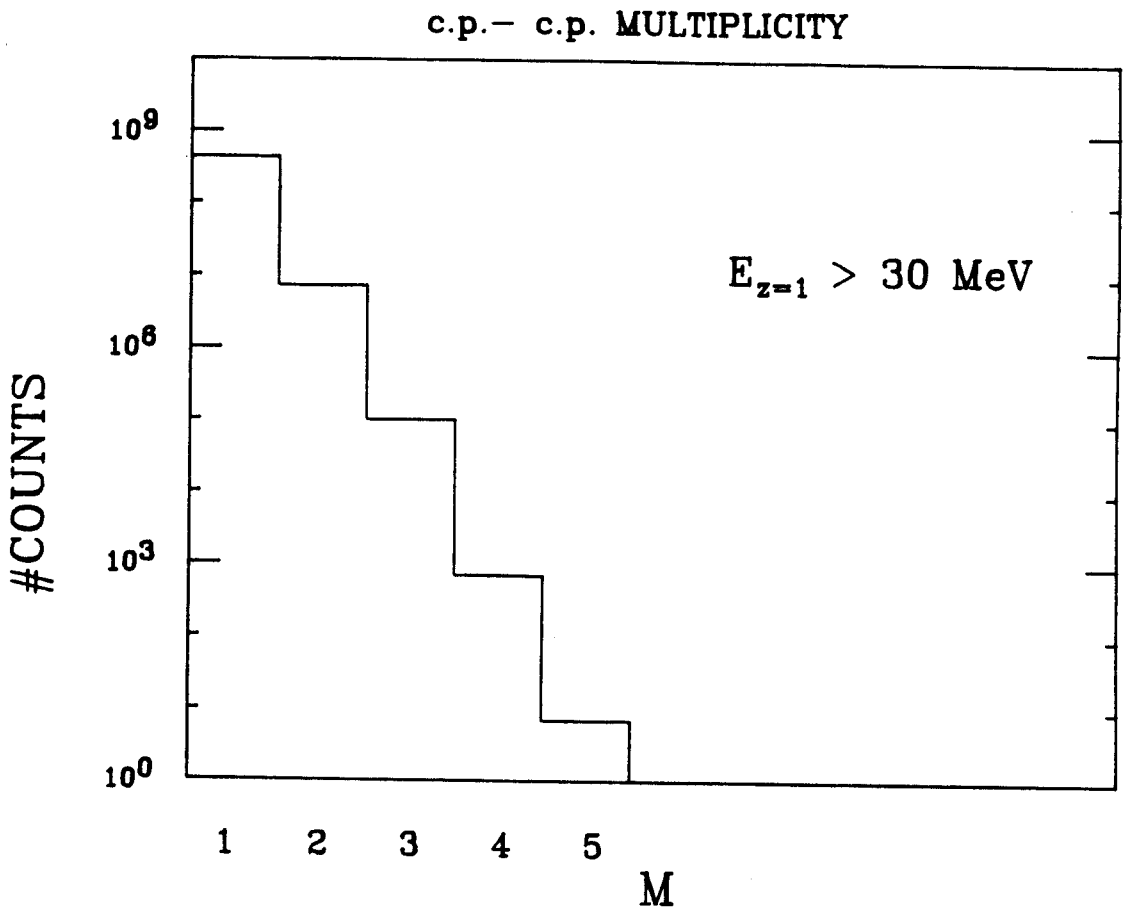

Figure III-21 Charged particle-charged particle multiplicity (cp-cp).

Table III-6. Multiplicities: Y - c.p. and c.p. - c.p.

	Y - c.p.		c.p. - c.p.
M=0	477913 ± 691	M=1	427924640 ± 20714
M=1	8689 ± 93	M=2	7056394 ± 3046 (frontal solid angle)
			7085198 ± 3057 (back solid angle)
M=2	63 ± 8	M=3	97927 ± 167
		M=4	682 ± 12
		M=5	7 ± 1

In calculating the uncertainty, we have to consider two sources of error. The first originates from the nature of the scale-down factor: a count for PH_k is not recorded until the real number of counts reaches an integer multiple of n_k. The correct number of counts in phoswich PH_k is, therefore, between

III-5 (# counts recorded $PH_k \cdot n_k$)

and

III-6 (# counts recorded $PH_k + 1) \cdot n_k$.

To make this error symmetric we can rewrite it as

III-7 $$\left[\left(\#\text{ counts recorded } PH_k + \frac{1}{2}\right) \cdot n_k \pm \frac{n_k}{2}\right] .$$

The second uncertainty is purely statistical and for phoswich PH_k is just $[\#\text{ counts } PH_k]^{1/2}$. The uncertainty for PH_k, obtained with the quadrature method, is then

III-8 $$\Delta(\#\text{counts } PH_K) =$$

$$\left\{\left(\frac{n_k}{2}\right)^2 + \left[\sqrt{\left(\#\text{counts recorded } PH_k + 0.5\right)\cdot n_k}\ \right]^2\right\}^{1/2}$$

and the multiplicity-one datum can be written as:

$$\text{III-9} \qquad \sum_{k=1}^{14}\left(\#\text{ counts recorded } PH_k + \frac{1}{2}\right) \cdot n_k \pm$$

$$\sum_{k=1}^{14}\left[\left(\frac{n_k}{2}\right)^2 + \left(\#\text{ counts recorded } PH_k + 0.5\right) \cdot n_k\right]^{1/2}.$$

The multiplicity-two analysis was complicated by the fact that the coincidence of the two Z=1 isotopes was scaled down by a factor consisting of a combination of the scale-down factors of the two detectors under consideration. If PH_i and PH_j represent two phoswichs, not part of the same "or" group, and n_i and n_j their respective scale-down factors, the total number of coincidences for the pair would be:

$$\text{III-10} \qquad \#\text{ coinc. } PH_i\ PH_j = \frac{\#\text{ coinc. } PH_i\ PH_j \text{ recorded}}{\frac{1}{n_i} + \frac{1}{n_j} - \frac{1}{n_i n_j}}$$

For phoswichs in the same "or" group the number of coincidences is simply :

$$\text{III-11} \qquad \#\text{ coinc. } PH_i\ PH_j = \frac{\#\text{ coinc. } PH_i\ PH_j \text{ recorded}}{\frac{1}{n_j}}$$

In considering coincidences between a phoswich, PH_k, and any other phoswich the solid angle available to detect the second charged particle

Figure III-22 shows a comparison of the rescaled multiplicities. The ratio between the gamma - charged particle multiplicity M=1 (a Z=1 charged particle in coincidence with a gamma ray) and the charged particle - charged particle multiplicity M=2 (a Z=1 charged particle in coincidence with a Z=1 charged particle) is 1.103 ± 0.012 using frontal solid angles and 1.098 ± 0.012 using back solid angles. Because of the small number of counts in the Y-c.p. M=2 bin and the large uncertainty in the c.p.-c.p. M=3 bin, due to the lack of a precise solid angle correction, a comparison between these two multiplicities can not be made quantitatively.

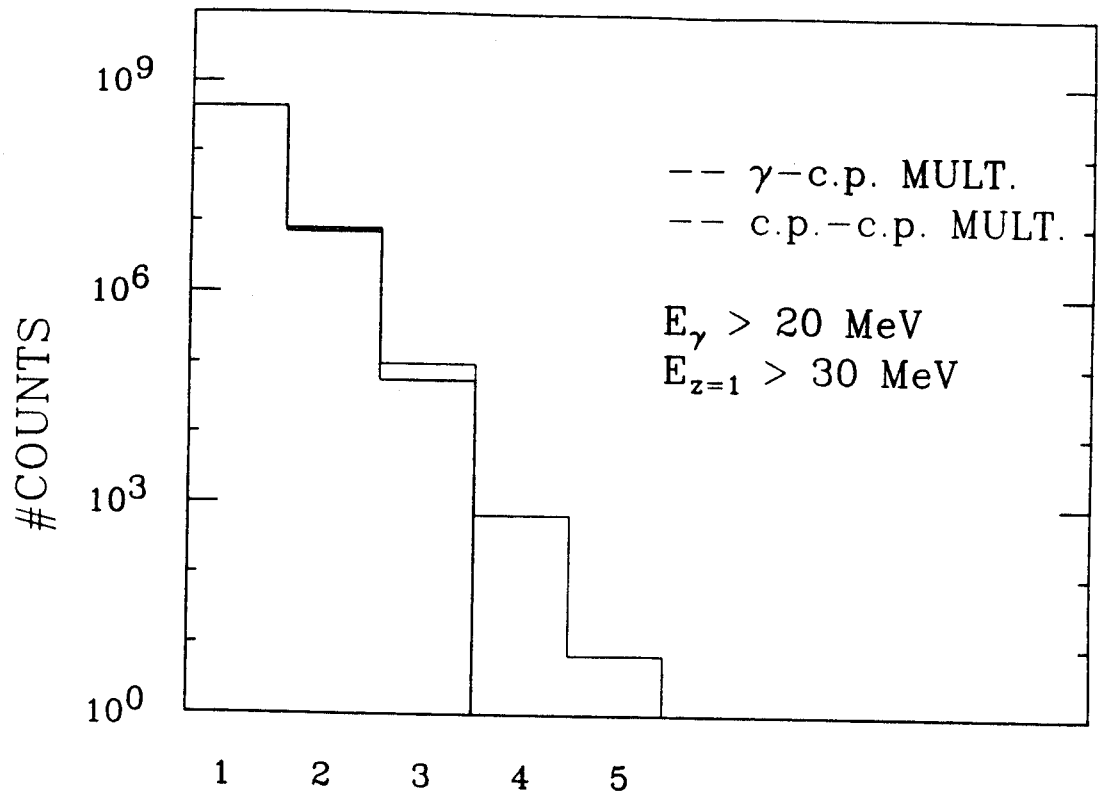

Figure III-22 Comparison of the Y-cp and cp-cp multiplicities.

CHAPTER IV

INTERPRETATION OF THE COINCIDENCE RESULTS

A. IMPACT-PARAMETER DEPENDENCE

Hingmann et al. [Hi 87] performed at GANIL the first exclusive high-energy gamma-ray experiment observing the products of the reaction $^{40}Ar + ^{158}Gd$ at E/A=44 MeV. Gamma rays at 90° fulfilling the following conditions were examined:

(a) coincidences with slow heavy fragments (central collisions)

(b) coincidences with fast projectile-like fragments (peripheral collisions).

(c) no coincidences with charged particles (grazing collisions)

The gamma-ray spectra obtained in the three cases are shown in Figure IV-1. Keeping in mind that the conditions under study probably contain some overlap, a comparison of spectra (a) and (b) shows a larger yield of gamma rays associated with more central collisions. The difference in the slope parameter could be simply related to the poor statistics in the high-energy portion of spectrum (b). The dashed lines in Figure IV-1 are the results of a nucleon-nucleon bremsstrahlung calculation.

Herrmann et al. [He 87] studied high-energy gamma rays produced in the reaction $^{92}Mo + ^{92}Mo$ at the incident beam energy of 19.5 MeV/nucl. at the UNILAC at GSI. Gamma rays were observed in the angular range between 90 and 170° in coincidence with binary fragments of charge Z>10

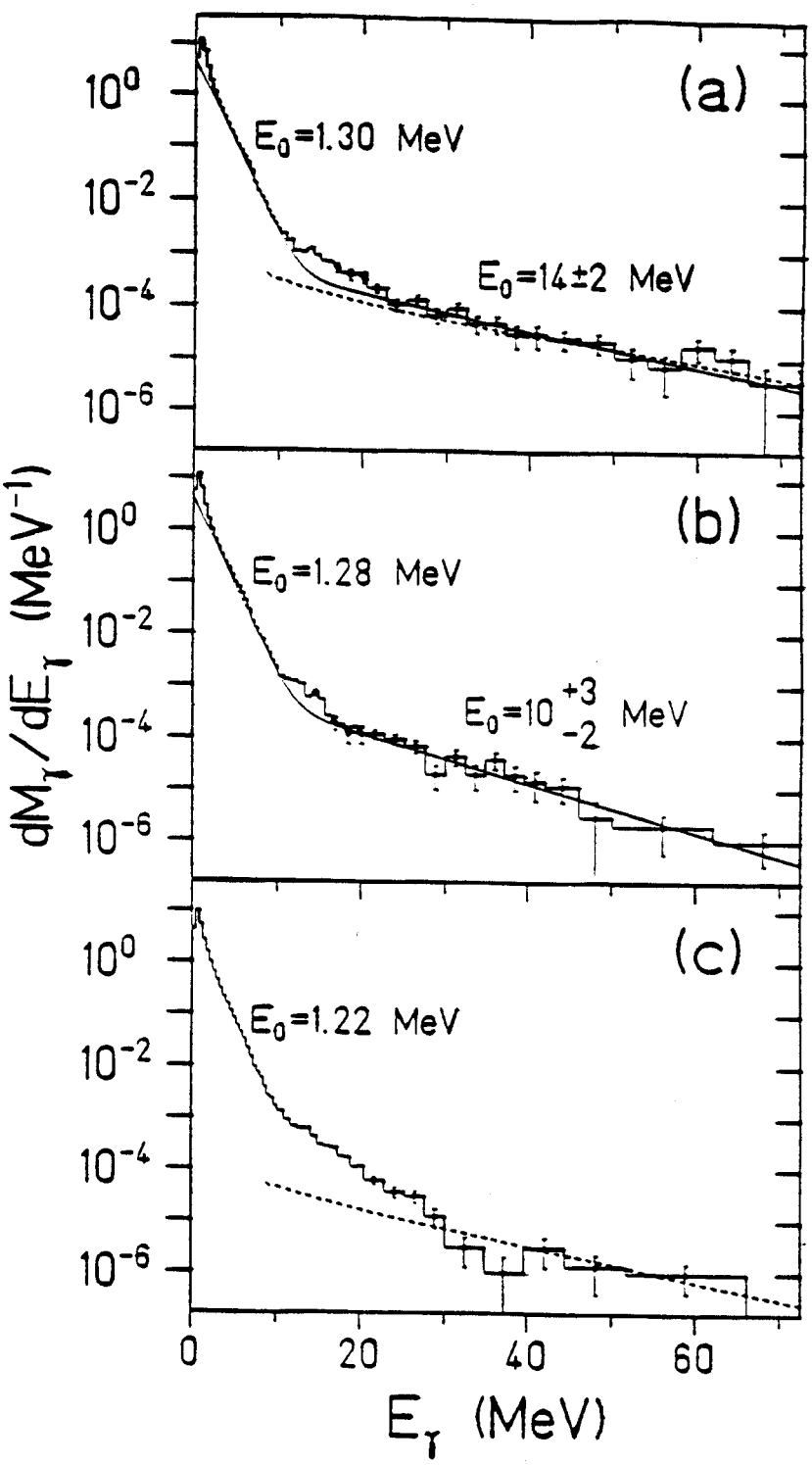

Figure IV-1 Gamma-ray spectra from reference [Hi 87]:
(a) coincidences with slow heavy fragments
(b) coincidences with fast projectile like fragments
(c) no coincidence with charged particles .

detected in the forward hemisphere. The gamma-ray yield was studied as a function of the total kinetic-energy loss in the collision (TKEL). Increasing TKEL was found to be associated with an increase in the gamma-ray yield and with a flatter spectral slope. Their interpretation associated the gamma-ray production to a statistical emission from the excited fragments rather then to a nucleon-nucleon bremmstrahlung process.

To test further the impact parameter dependence of the gamma-ray emission we studied the charged particle (Z=1) multiplicity associated with gamma-ray production (Figure III-19) and compared it with the charged-particle (Z=1) multiplicity associated with charged-particle production (Figure III-20). If gamma rays are produced mainly in central collisions, the average charged-particle multiplicity associated with the emission of a gamma ray is expected to be higher than the charged-particle multiplicity associated with the emission of other particles such as Z=1 isotopes. A comparison of the two (Figure III-21 and Table III-6) shows only a small enhancement (≈10%) of the charged-particle (Z=1) production when a gamma ray is also produced. On the limited basis of this result, since higher multiplicities results are not available, high-energy gamma-ray emission appears to have an impact-parameter dependence similar to that of the light Z=1 charged-particle production. A fundamental difference between the two measurements needs to be pointed out: while in the gamma ray case the coincidences are detected on the opposite side of the beam in the charged particle - charged particle case both particles are detected on the the same side of the beam. The p-p, p-d and d-d coincidence results of D. Fox et al. [Fo 87] for C + Ag at E/A=40 MeV do not show much difference between

coincidences of particle detected on the same or on the opposite side of the beam and suggests a similar behavior for coincidences of Z=1 particles.

In chapter II we saw that recent calculations [Ba 86] predict the impact-parameter dependence of the gamma-ray yield to be proportional to the overlap area of the colliding nuclei. We calculated the value of the ratio R using this geometrical approximation.

The overlap area, A(b), of the projectile and the target nucleus is calculated assuming the nuclei to be spheres with radii $R = 1.2\ A^{1/3}$ fm (Figure IV-2). In our specific case, R_1 is the radius of the zinc nucleus, R_2 is the radius of the nitrogen nucleus, and b is the impact parameter.

The ordinate of the two intersection points is indicated by y_0, and its value is found by solving the system formed by the equations of the two circles representing the two nuclei (equation IV-1). The resulting expression for y_0 is given in equation IV-2.

IV-1
$$x^2 + y^2 = R_1^2$$
$$x^2 + (y - b)^2 = R_2^2.$$

IV-2
$$y_0 = \frac{R_1^2 - R_2^2 + b^2}{2b}$$

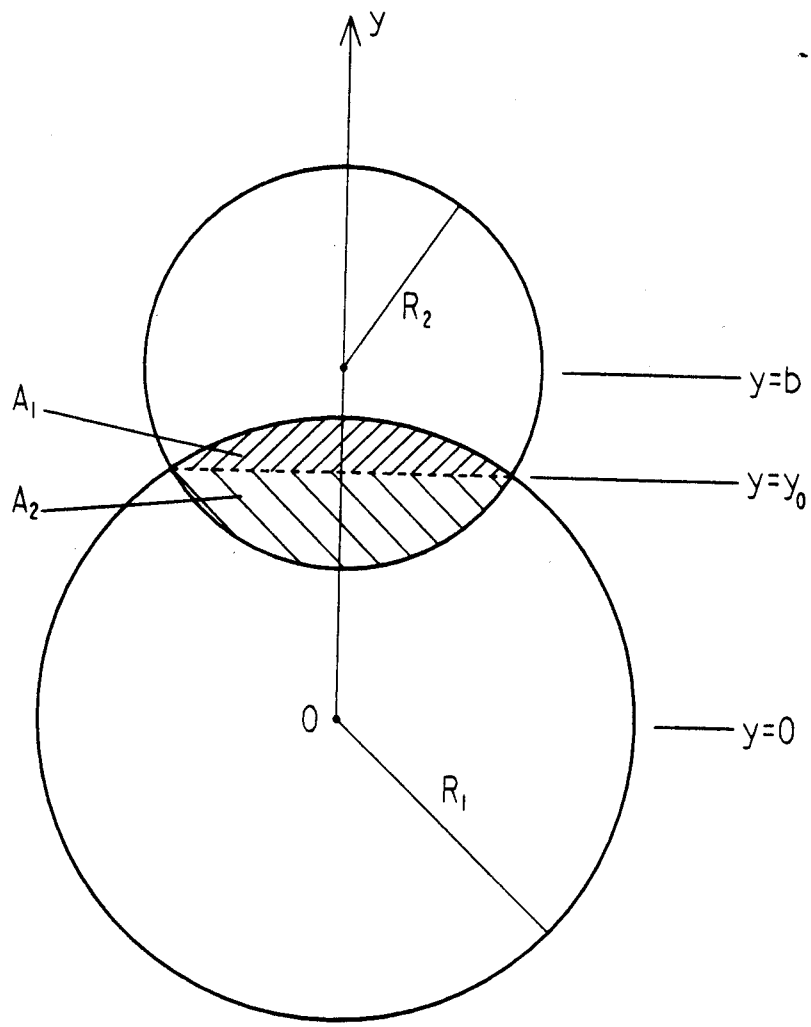

Figure IV-2 Overlap between the Zn nucleus (radius R_1) and the N nucleus (radius R_2) .

For $b \geq (R_1 - R_2)$ the shaded overlap area $A_1(b)$, a section of the circle of radius R_1, is given by equation IV-3. The shaded overlap area $A_2(b)$, a section of the circle of radius R_2, is given by equation IV-4. The total overlap area is $A(b) = A_1(b) + A_2(b)$. For $b \leq (R_1 - R_2)$ the overlap area is simply the area of the smallest circle namely $A(b) = \pi R_2^2$.

IV-3 $$A_1(b) = 2 \int_{y_0}^{R_1} \sqrt{R_1^2 - y^2}\, dy =$$

$$R_1^2 \arccos \frac{y_0}{R_1} - y_0 R_1 \sqrt{1 - \left(\frac{y_0}{R_1}\right)^2}$$

IV-4 $$A_2(b) = 2 \int_{b - y_0}^{R_2} \sqrt{R_2^2 - (b - y)^2}\, dy =$$

$$R_2^2 \arccos \frac{b - y_0}{R_2} - R_2(b - y_0) \sqrt{1 - \left(\frac{b - y_0}{R_2}\right)^2}$$

The coincidence to singles ratio can be calculated by assuming that the proton and gamma-ray cross sections are both proportional to $A(b)$. The ratio R assuming the following proportionality:

IV-5 $\sigma_\gamma \propto A(b)$, $\sigma_p \propto A(b)$ and $\sigma_{\gamma p} \propto A(b)A(b)$

is then given by equation IV-6.

IV-6
$$R = \frac{\int_0^{R_1+R_2} [A(b)]^2 d^2b}{\left[\int_0^{R_1+R_2} A(b)\, d^2b\right]^2} =$$

$$\frac{\int_{R_1-R_2}^{R_1+R_2} [A_1(b) + A_2(b)]^2 d^2b + \int_0^{R_1-R_2} [\pi R_2^2]^2 d^2b}{\left[\int_{R_1-R_2}^{R_1+R_2} [A_1(b) + A_2(b)]\, d^2b + \int_0^{R_1-R_2} \pi R_2^2\, d^2b\right]^2}$$

The integration was performed numerically.

We also considered an impact parameter dependence proportional to the overlap volume of the two nuclei. The ordinate of the two intersection points is indicated with z_0, and its value is found by solving the system formed by the equations of the two spheres representing the two nuclei (equation IV-7). The resulting expression for z_0 is given in equation IV-8.

IV-7
$$x^2 + y^2 + z^2 = R_1^2$$
$$x^2 + y^2 + (z - b)^2 = R_2^2.$$

IV-8 $$z_0 = \frac{R_1^2 - R_2^2 + b^2}{2b}$$

For $b \geq (R_1 - R_2)$ the shaded overlap volume $V_1(b)$, a section of the sphere of radius R_1, is given by the integral in equation IV-9 and the shaded overlap volume $V_2(b)$, a section of the sphere of radius R_2 is given by the integral in equation IV-10. The total overlap volume is $V(b) = V_1(b) + V_2(b)$.

For $b \leq (R_2 - R_1)$ the overlap volume is simply the volume of the smallest sphere namely $V(b) = \frac{4}{3}\pi R_2^3$.

IV-9 $$V_1(b) = \int_0^{2\pi} d\phi \int_0^{\arccos(z_0/R_1)} \sin\theta \, d\theta \int_{z_0/\cos\theta}^{R_1} r^2 \, dr =$$

$$\frac{\pi}{3}[\, 2R_1^3 - 3z_0R_1^2 + z_0^3\,]$$

IV-10 $$V_2(b) = \int_0^{2\pi} d\phi \int_0^{\arccos(b-z_0)/R_2} \sin\theta \, d\theta \int_{(b-z_0)/\cos\theta}^{R_2} r^2 \, dr =$$

$$\frac{\pi}{3}[\, 2R_2^3 - 3(b-z_0)R_2^2 + (b-z_0)^3\,].$$

Under the assumptions shown in equation IV-11, the ratio R then is given by equation IV-12.

IV-11 $\sigma_\gamma \propto V(b)$, $\sigma_p \propto V(b)$ and $\sigma_{\gamma p} \propto V(b)V(b)$

IV-12
$$R = \frac{\int_0^{R_1+R_2} [V(b)]^2 d^2b}{\left[\int_0^{R_1+R_2} V(b)\, d^2b\right]^2} =$$

$$\frac{\int_{R_1-R_2}^{R_1+R_2} [V_1(b)+V_2(b)]^2 d^2b + \int_0^{R_1-R_2} \left[\frac{4}{3}\pi R_2^3\right]^2 d^2b}{\left[\int_{R_1-R_2}^{R_1+R_2} [V_1(b)+V_2(b)]\, d^2b + \int_0^{R_1-R_2} \frac{4}{3}\pi R_2^3\, d^2b\right]^2}$$

We also calculated the ratio with the following assumptions:

IV-13 $\sigma_\gamma \propto A(b)$, $\sigma_p \propto V(b)$ and $\sigma_{\gamma p} \propto V(b)A(b)$

The ratio R then becomes:

IV-14
$$R = \frac{\int_0^{R_1+R_2} [V(b)A(b)]\, d^2b}{\left[\int_0^{R_1+R_2} V(b)\, d^2b \int_0^{R_1+R_2} A(b)\, d^2b\right]}$$

Table IV-1 is a list of the results obtained under the different assumptions made. The values of the ratio obtained with the different

TABLE IV-1. Values for the ratio obtained with the assumptions of equations IV-5, IV-11 and IV-13 as compared to the experimental result.

	AREA $(barn)^{-1}$	VOLUME $(barn)^{-1}$	AREA + VOLUME $(barn)^{-1}$	EXP. $(barn)^{-1}$
RATIO	0.903	1.001	0.948	0.6

assumptions are not very different from each other, but they overestimate the experimental results by at least 50%.

While the assumption $\sigma_\gamma \propto A(b)$ is based upon theoretical calculations [Ba 86], the assumption $\sigma_p \propto A(b)$ is somehow ad hoc . In order to establish if the above calculations fail to reproduce the experimental result because of a poor parametrization of the proton cross-section we calculated, the ratio $R_{Z=1}$ in equation IV-15 as a function of the Z=1 isotope angle.

$$\text{IV-15} \qquad R_p(\theta_p) = \frac{\sigma_{Z=1\ Z'=1}(\theta_p)}{\sigma_{Z`=1}\ \sigma_{Z=1}(\theta_{Z=1})}$$

Figure IV-3 and IV-4 show $R_{Z=1}$ for $\theta_{Z`=1} = 60°$ and $\theta_{Z`=1} = 120°$ respectively. The value of $R_{Z=1}$ is constant over the angular range studied and the mean value is fairly close to the value of 0.6 $barn^{-1}$ found in the gamma ray-charged particle case. The experimental value is again overestimated by at least 50%. This result, since an estimated half of the Z=1 isotope data is represented by protons, seems to indicate that the suggested parametrization is not indeed a very good approximation. Energy constraints in the emission of the second particle could cause a reduction in the number of coincidences observed which would in this case be a function of the fragment energy. No such energy dependence is, though, observed experimentally at least in the γ-c.p. case.

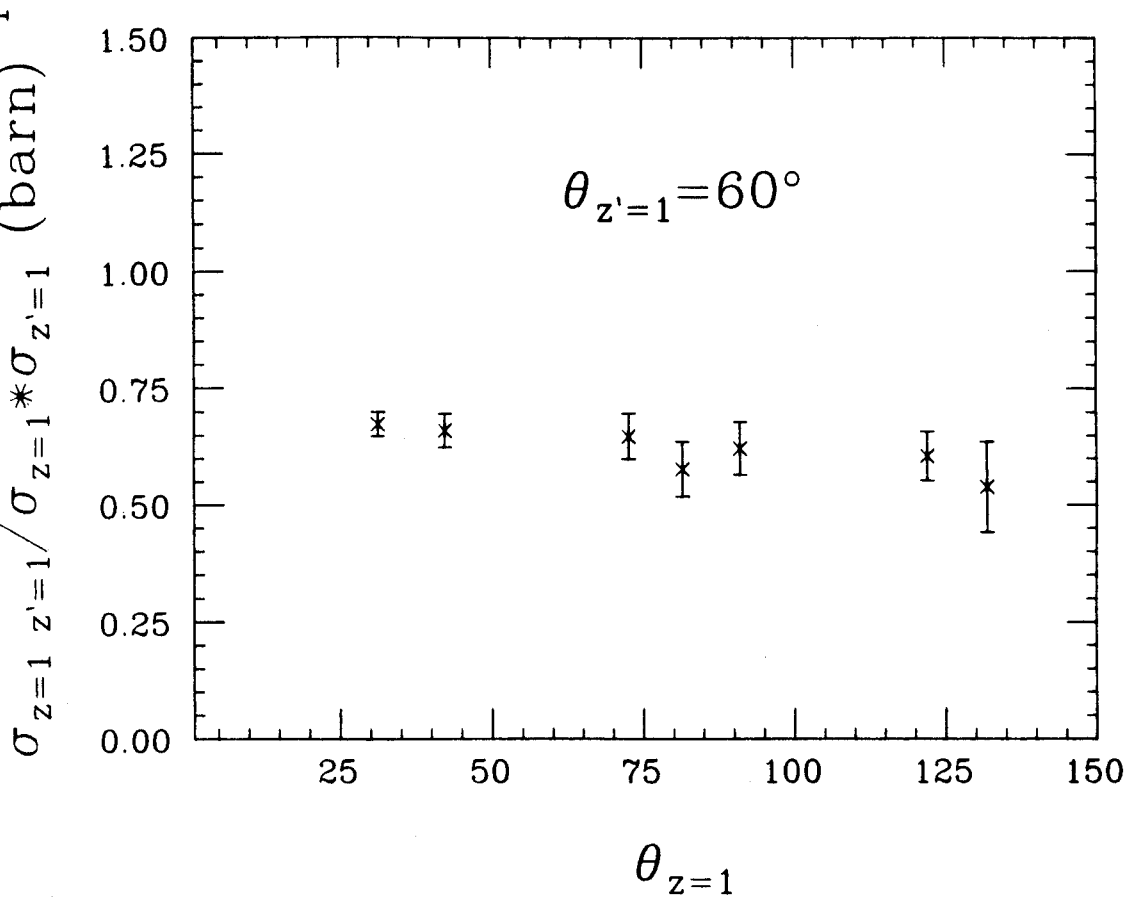

Figure IV-3 $R_{Z=1}(\theta_{Z=1})$ versus $\theta_{Z=1}$ for $\theta_{Z'=1}=60°$.

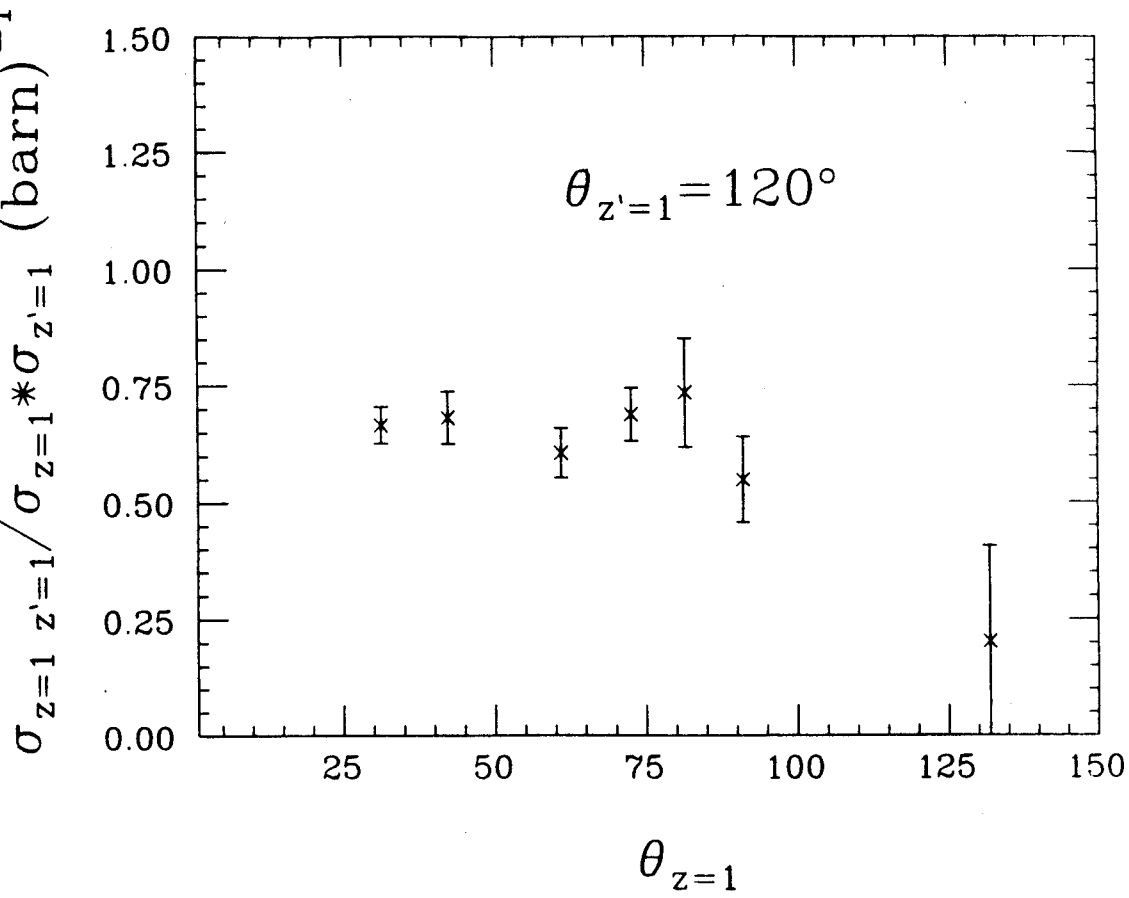

Figure IV-4 $R_{Z=1}(\theta_{Z=1})$ versus $\theta_{Z=1}$ for $\theta_{Z'=1}=120°$.

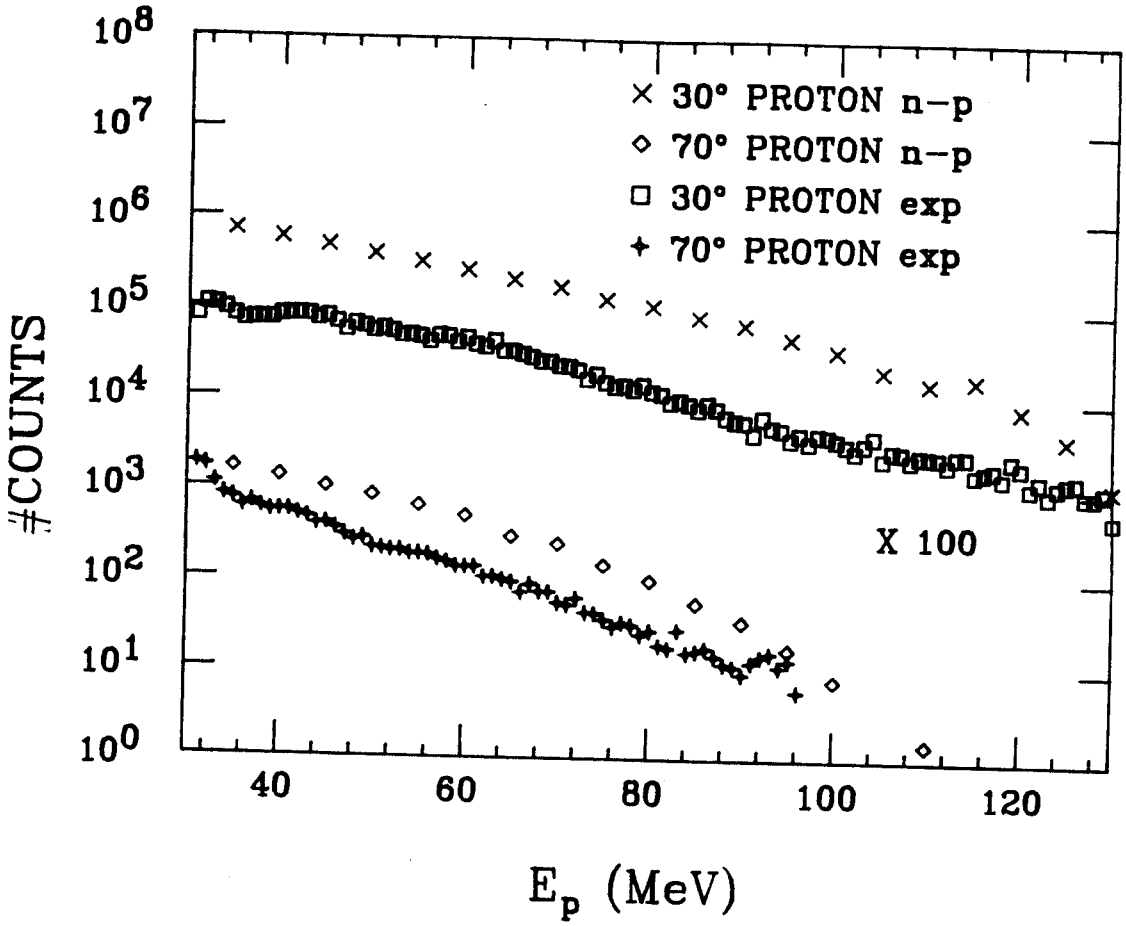

Figure IV-5 Proton spectra at 30 and 70°: experimental and n-p model.

B. n-p BREMSSTRAHLUNG MODEL.

We wrote a Monte Carlo code to simulate the gamma-ray emission by a n-p bremsstrahlung process since this is one of the mechanisms proposed to explain the inclusive gamma-ray data. We used the code to study the ratio of the coincidence cross section to the product of the singles cross sections as a function of the gamma-ray and proton angle and energy. What follows is a brief description of the model, the results obtained with it and their comparison with the experimental results. The inputs of the program are: the number of n-p collisions to be studied and the experimental beam energy.

The three components of the proton and neutron momenta are randomly chosen to be inside a cube of side $2*p_{fermi}$ centered around zero in such a way that the magnitude of each momentum is smaller than the Fermi momentum. The additional velocity associated with one of the particles being part of the beam (either the proton or the neutron) is added to obtain the total momentum of each particle. After a collision, in the center of mass of the n-p system, one of the hadronic directions is chosen randomly (isotropic scattering) and the direction of the second hadron is such that the total momentum is conserved. The gamma-ray kinetic energy is randomly picked to be between 0 and the maximum kinetic energy available in the center of mass. The gamma-ray emission probability, based on equation II-2, is then calculated. If a gamma ray is emitted, half of its energy is subtracted from both the neutron and the proton energy. In the lab frame the transformed momenta of the

neutron and proton are checked for Pauli blocking. If the momentum of the particle coming from the beam lies inside the projectile Fermi sphere or if the momentum of the target particle lies inside a non moving Fermi sphere, the event, even if it produced a gamma ray, is rejected. The Fermi energy is then subtracted from the energy of both particles. The outputs of the program are the direction, θ and ϕ, and the energy for both the proton and the gamma ray (if produced).

The first concern was to see if, with the n-p model, we could reproduce the correct angular distribution and energy dependence of both gamma rays and proton singles. The exponential decrease with energy and the slope of the proton spectra are well reproduced by the model as shown in Figure IV-5. While the agreement for the angles between 30 and 90° is fairly good, for larger angles, the model underpredicts the experimental results (Figure IV-6). The poor agreement at back angles is attributed to target fragments which are not included in the model.

The exponential decrease with energy and the slope of the gamma-ray spectra at 60 and 120° are well reproduced by the model as shown in Figure IV-7. The gamma-ray energy-integrated (20 - 128 MeV) angular distribution obtained with the model is compared in Figure IV-8 to the angular distribution obtained in the experiment described in Chapter I. The two data points from the inclusive data of the coincidence experiment are also shown. It is clear that the dipolar character of the gamma-ray emission probability of equation II-3 dominates the angular distribution obtained with the model and while the agreement for the middle angles is reasonably good the forward and backward angles are underpredicted by 40%.

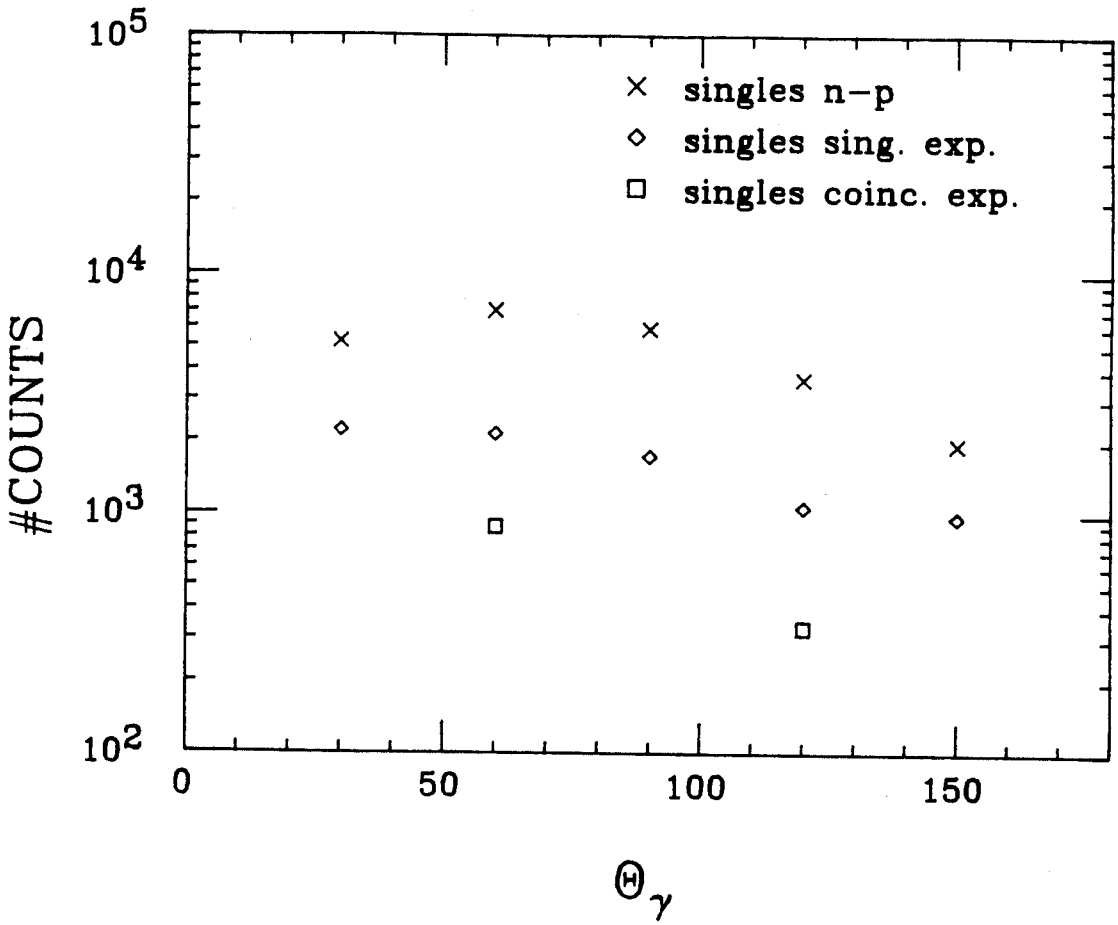

Figure IV-8 Gamma-ray energy-integrated angular distributions: experimental and n-p model results.

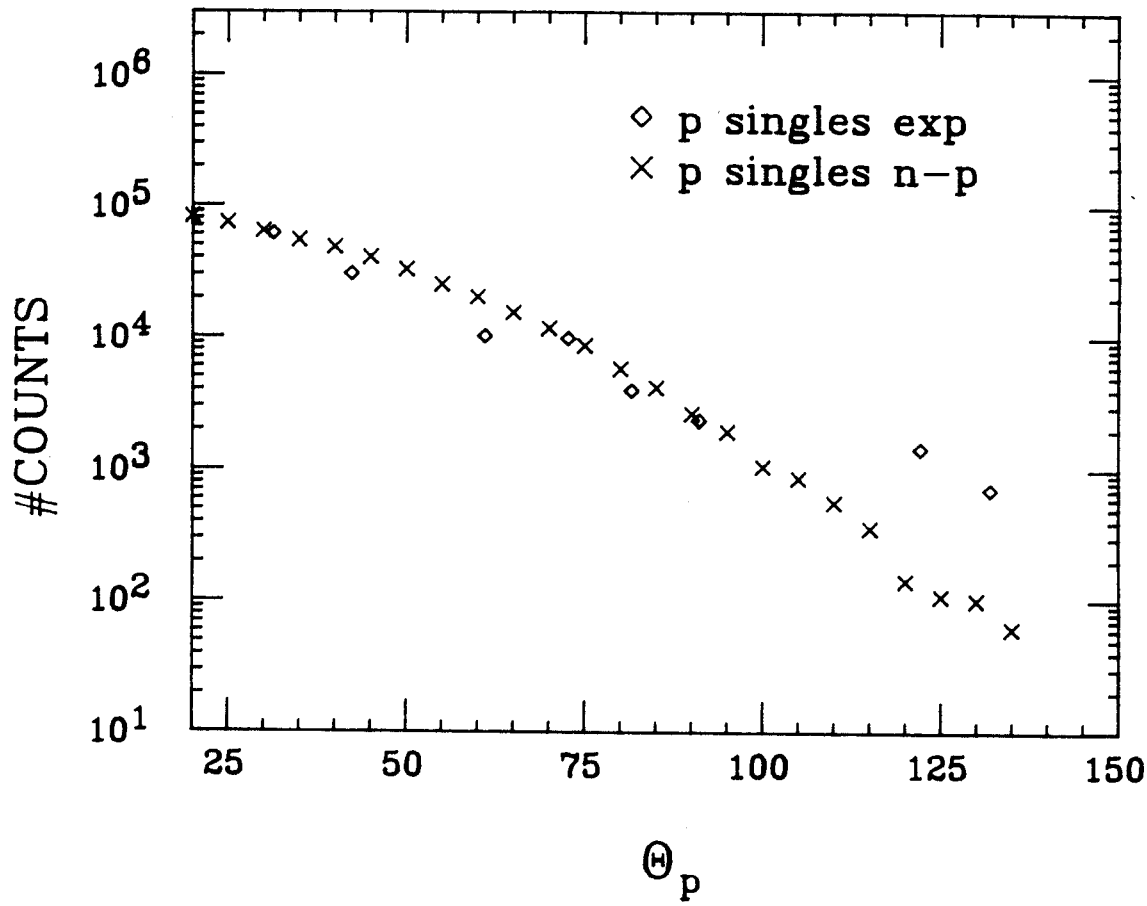

Figure IV-6 Proton energy-integrated angular distribution: experimental and n-p model results.

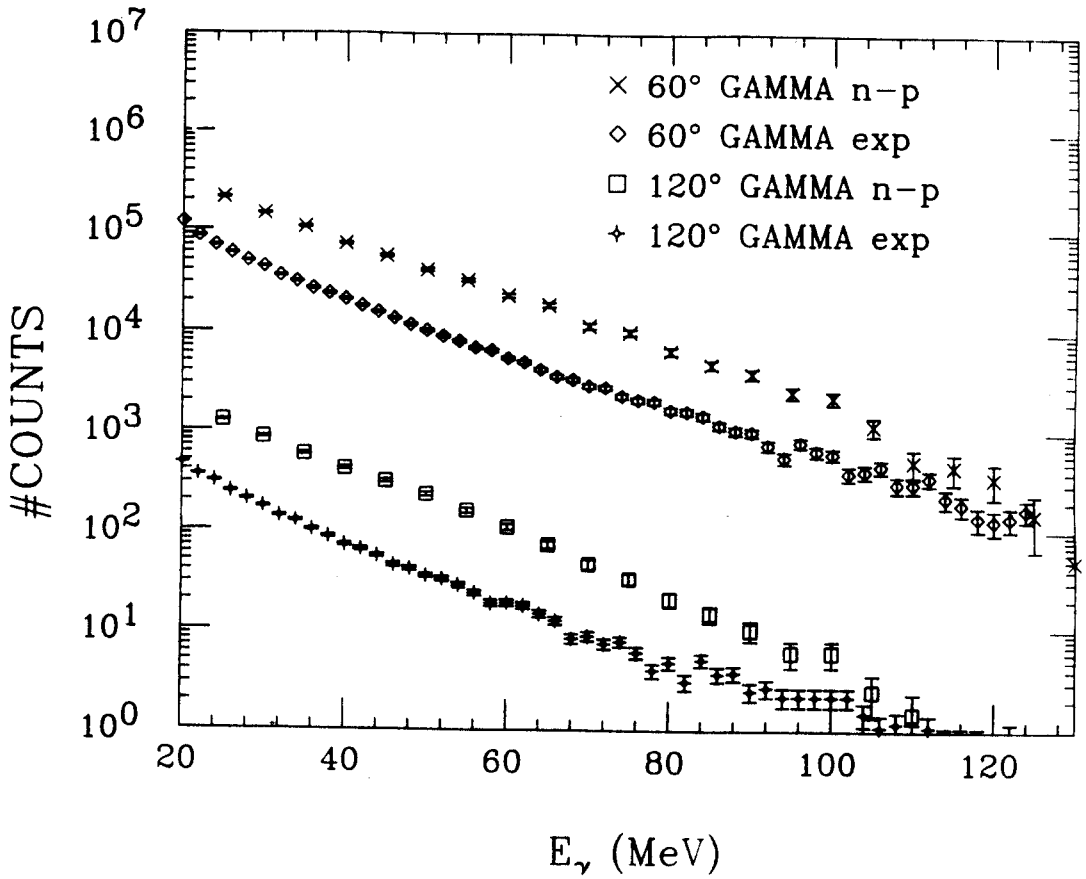

Figure IV-7 Gamma-ray spectra at 60 and 120°: experimental and n-p model results.

Our next step was to calculate the ratio of the coincidence to the product of the singles cross-sections and study it as a function of proton and gamma-ray angle and energy. In the calculations we used the impact parameter distribution, N(b), suggested in reference [Ba 85]

IV-15 $$N(b) \propto A(b)$$

where A(b) is the overlap area between the two nuclei and σ_{geo} is the geometrical cross section. The ratio R is then

IV-16 $$R = \frac{\int A(b)A(b)2\pi b\, db}{\left[\int A(b)2\pi b\, db\right]^2} \quad \frac{n_{\gamma p}}{n_\gamma \quad n_p}$$

where $n_{\gamma p}$, n_γ and n_p are the number, divided by the number of collisions studied, of gamma ray - proton coincidences, gamma rays and protons respectively. From Table IV-1 the ratio can be rewritten as

IV-17 $$R=0.903 \quad \frac{n_{\gamma p}}{n_\gamma \quad n_p}$$

Figures IV-9 through IV-12 show the n-p model results. While the experimental results do not show any appreciable variation with any of the physical quantities studied, the ratios obtained with the n-p model decrease fairly rapidly both when studied as a function of gamma-ray energy and when studied as a function of proton energy. The value of

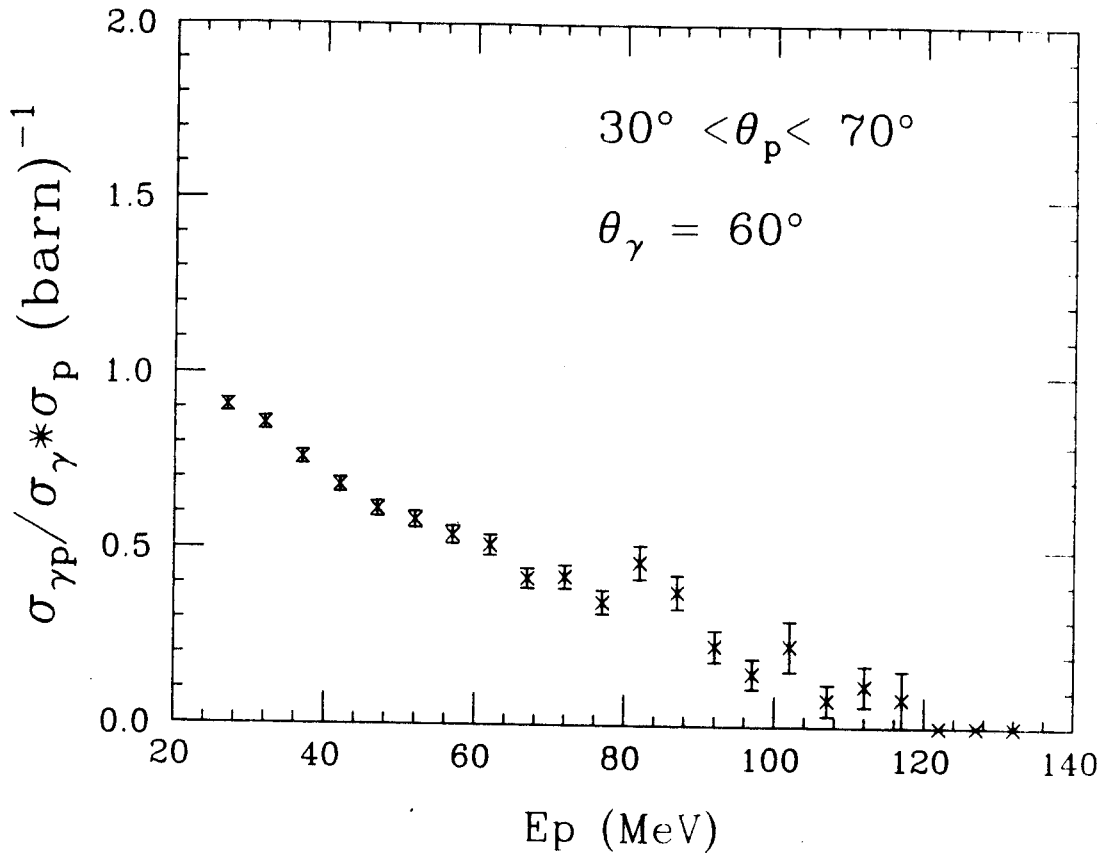

Figure IV-9 Ratio versus E_p for $30 < \theta_p < 70°$ in the n-p model.

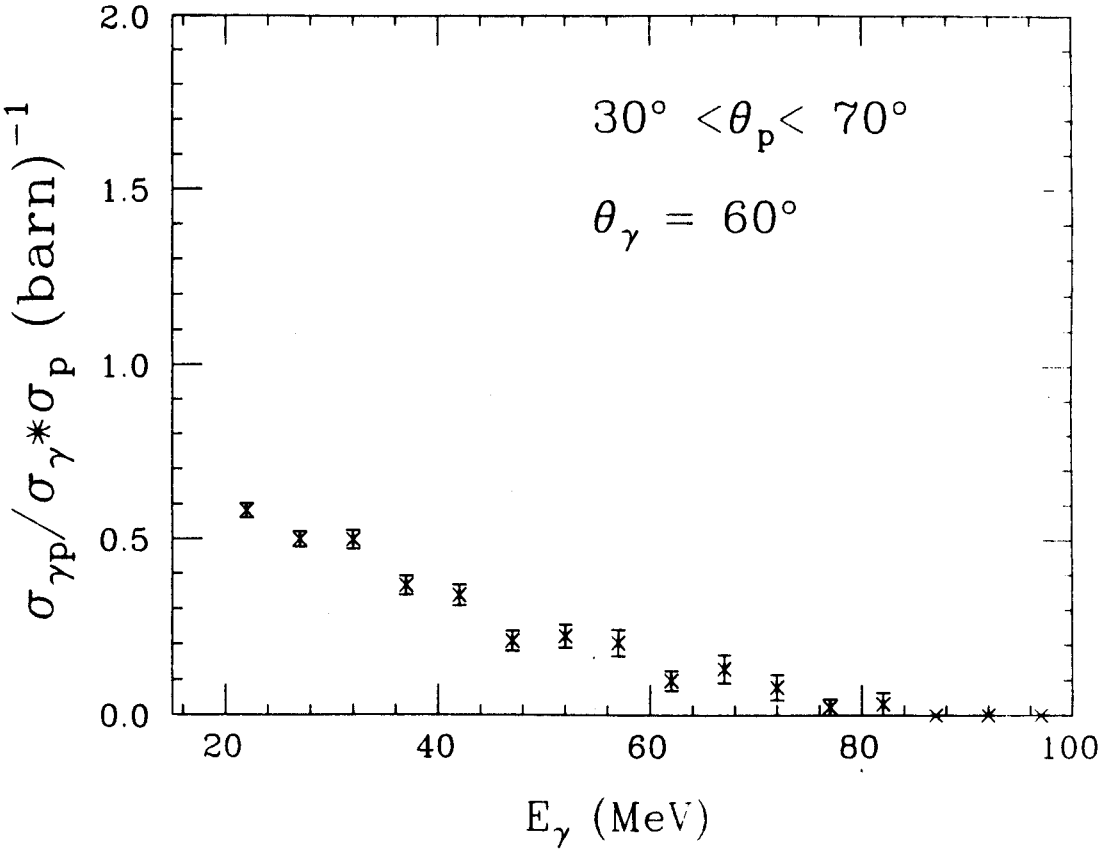

Figure IV-10 Ratio versus E_γ for E_p> 30 MeV in a reference frame moving with velocity equal to β=0.14 (n-p model).

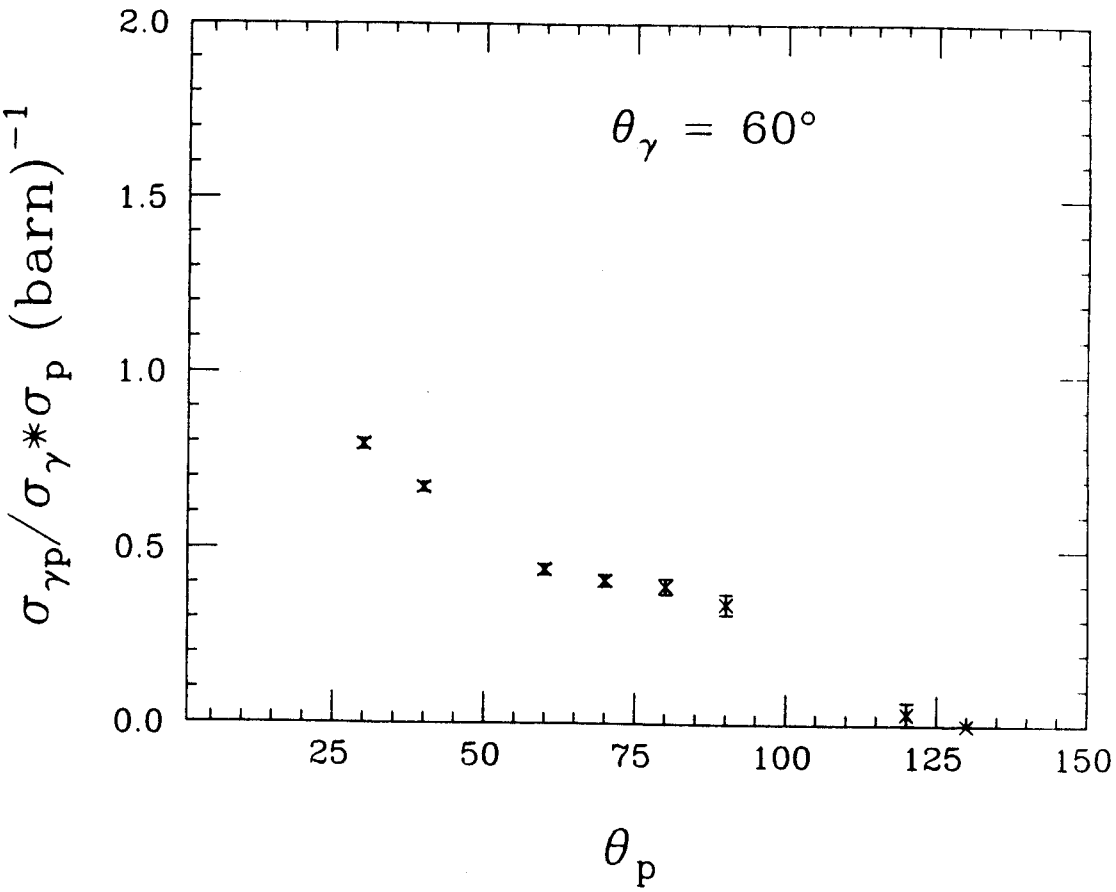

Figure IV-11 Ratio versus Θ_p for gamma rays at 60° in the n-p model.

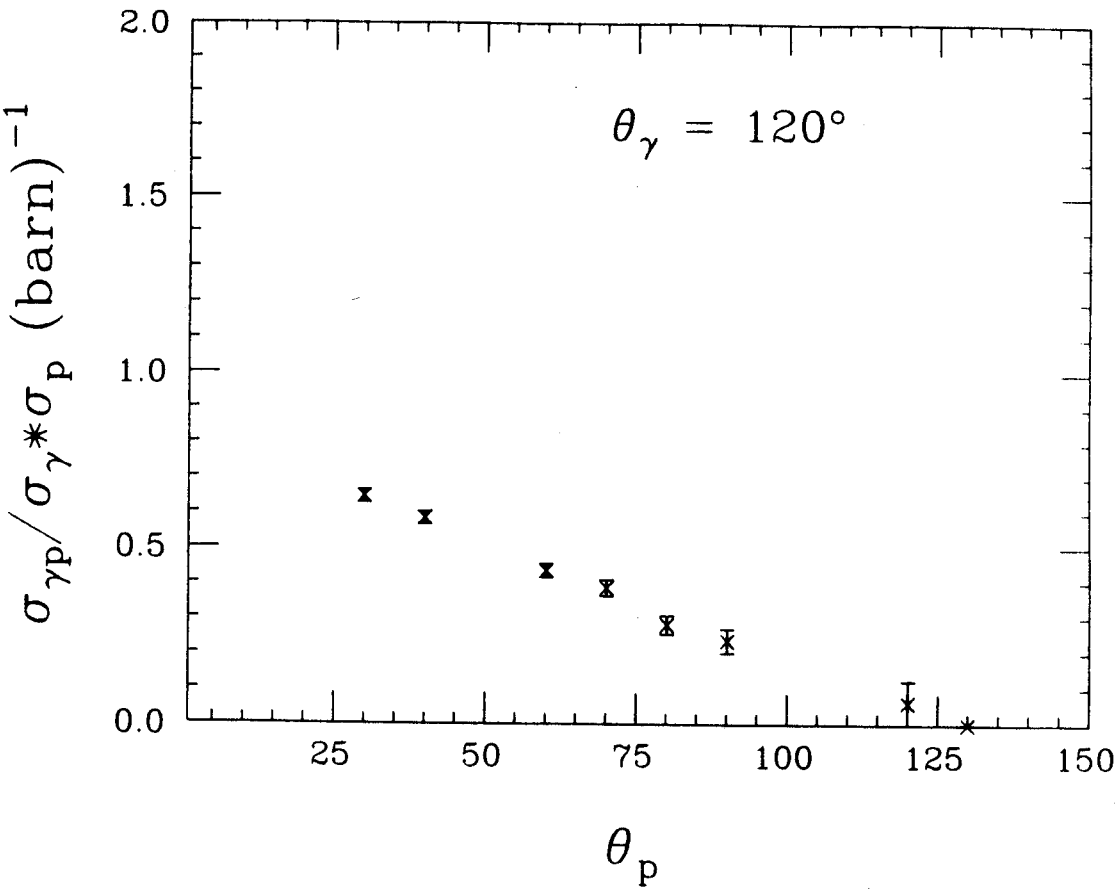

Figure IV-12 Ratio versus Θ_p for gamma rays at 120° in the n-p model.

the ratio studied as a function of proton angle decreases with increasing angle, and for a given proton angle the ratio is higher for D1(60°) than for D2(120°). It seems natural to associate the decreasing behavior of the ratios to the energy constraints implicit to the n-p model. We wondered if our experimental results were not an indication of a more collective process.

D. THERMAL MODEL

In order to mimic a process in which gamma rays are not produced in the first n-p collisions but are instead produced in a later stage of the reaction when the initial energy constrictions have been removed by multiple scatterings, we modify our previous model so that the energies of the proton and neutron are randomly picked from an exponential distribution $y=Ae^{-E/T}$ where A is a constant and T is a parameter often called "temperature". The inputs of the program are: the number of collisions to be studied, the value of the parameter T and the velocity β of the moving thermal source.

As before, we first tested the ability of the model to reproduce qualitatively the features of the singles spectra. Different values of β and T were employed to see how the value of these parameters affected the magnitude and the slope of both gamma-ray and proton spectra. The values β=0.10 and T=16 MeV were found to reproduce well the slope and the angular distribution for protons as shown in Figures IV-13 and IV-14. However, a value of T higher than 16 MeV is needed to reproduce better the gamma-ray spectra slope as shown in Figure IV-15. The

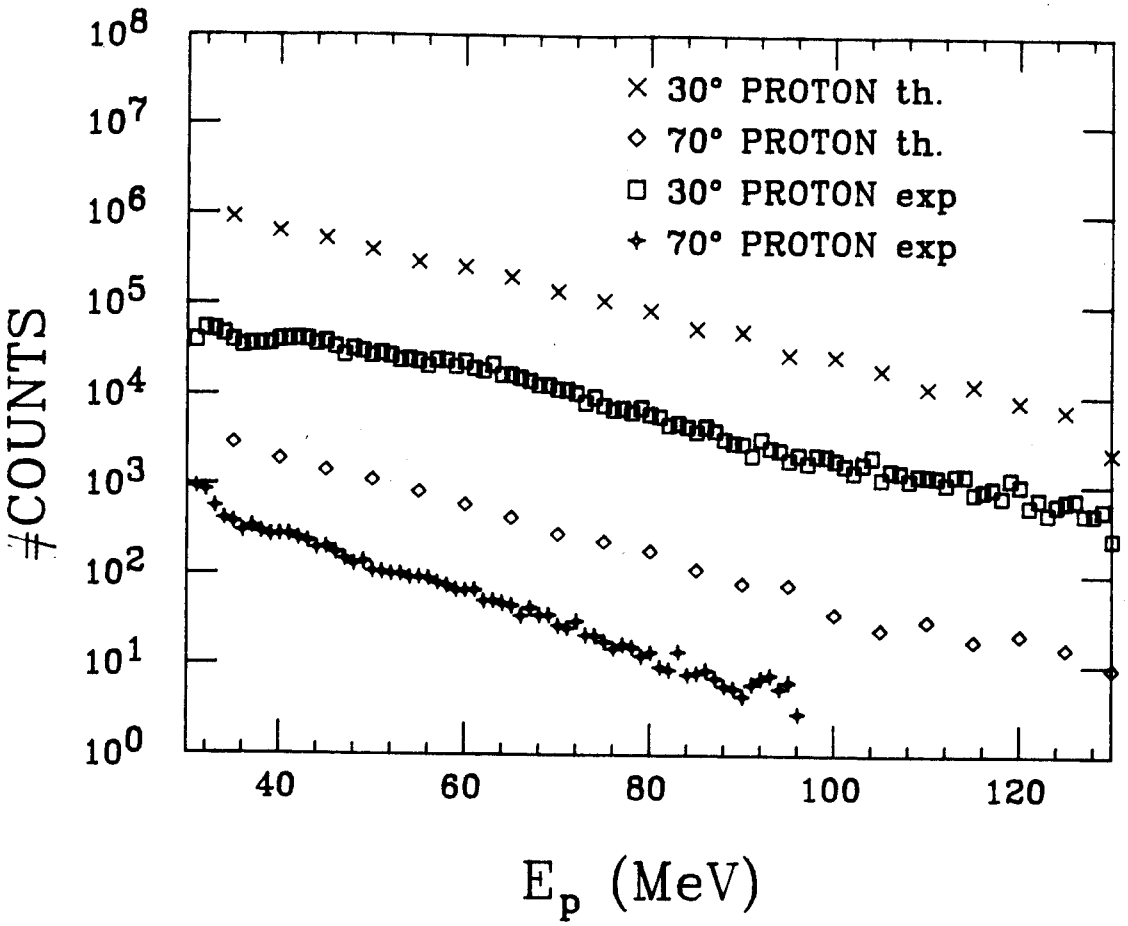

Figure IV-13 Proton spectra at 30 and 70°: experimental and thermal model results.

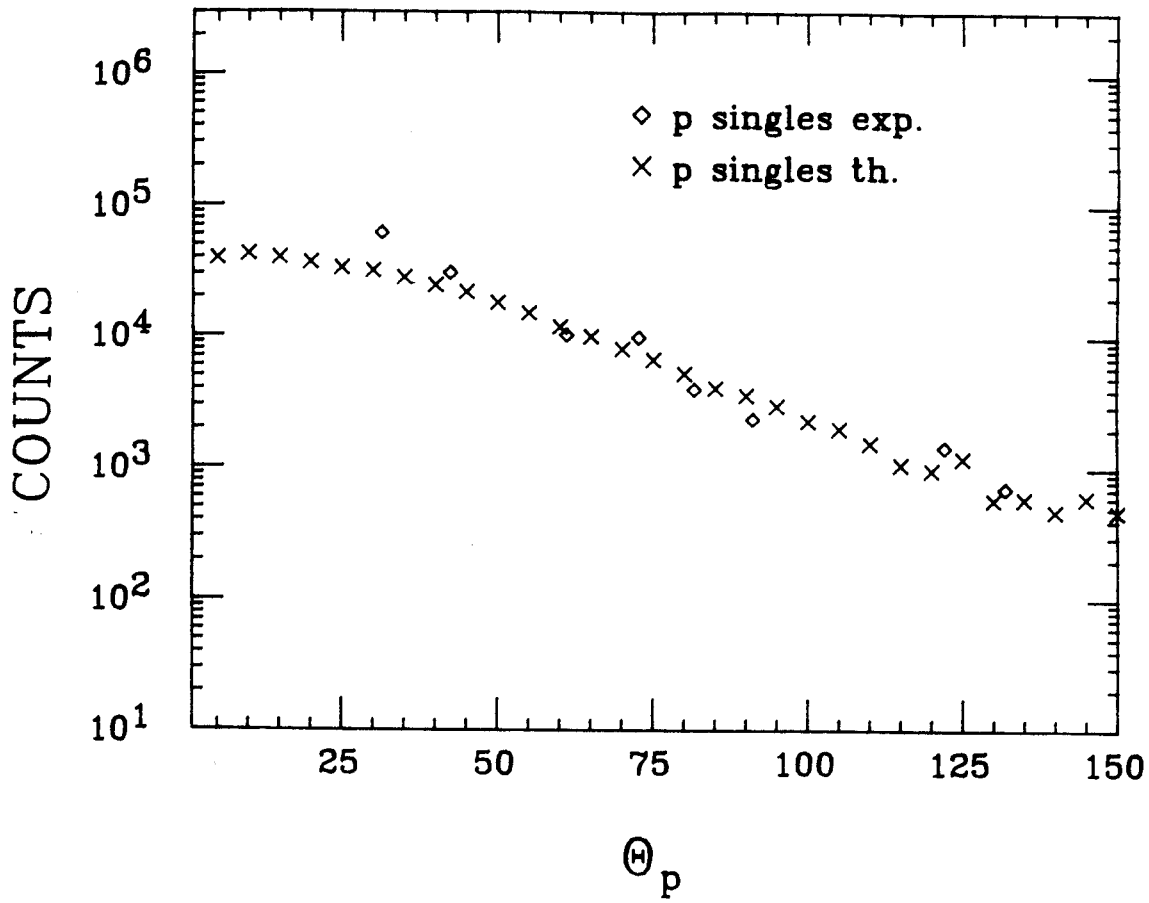

Figure IV-14 Proton energy-integrated angular distribution: experimental and thermal model results.

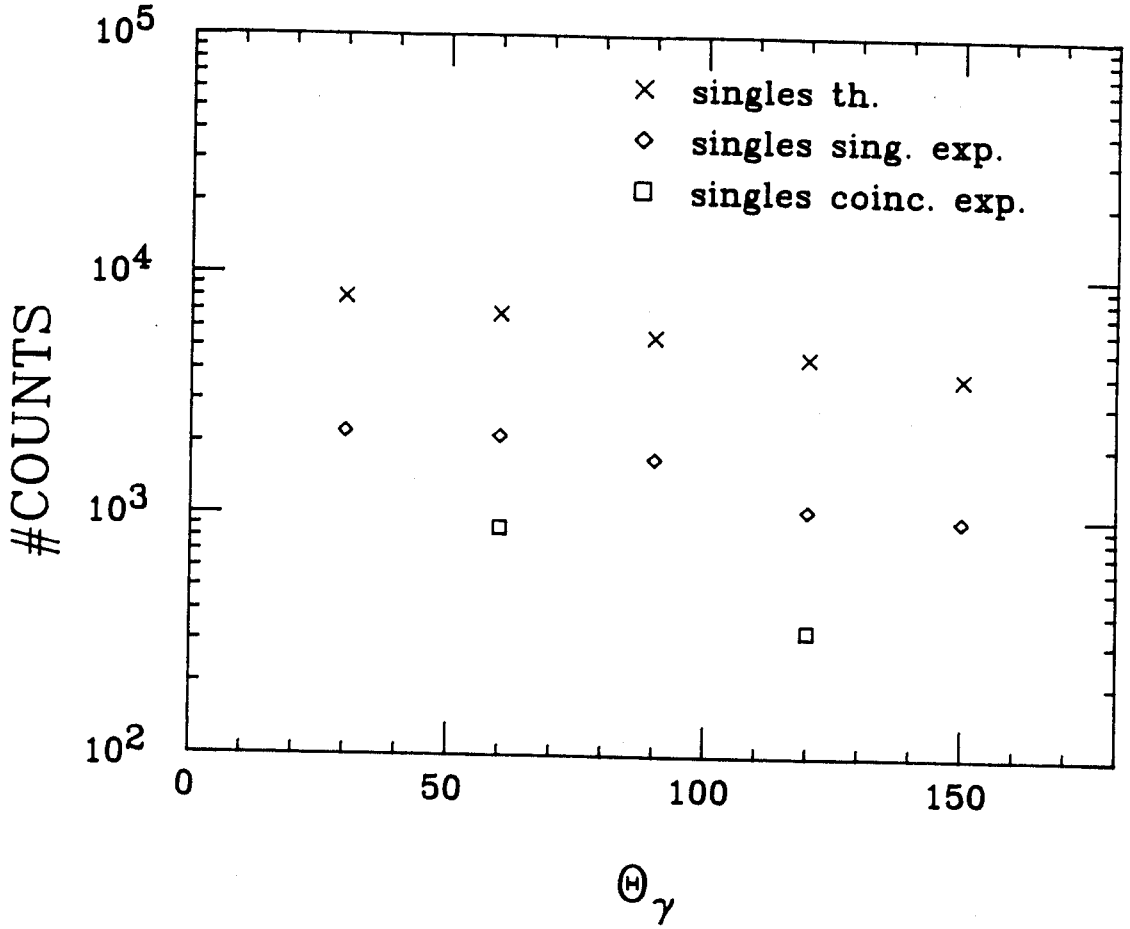

Figure IV-16 Gamma-ray energy-integrated angular distributions: experimental and thermal model results.

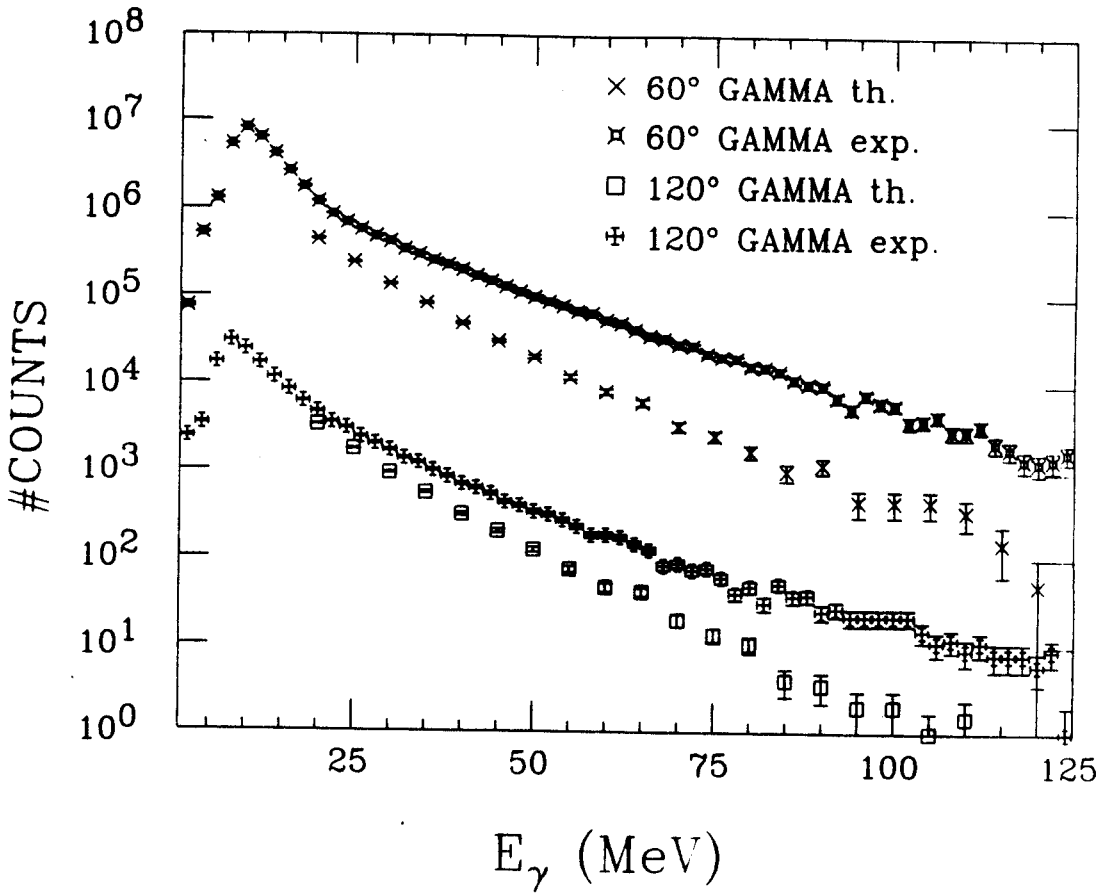

Figure IV-15 Gamma-ray spectra at 60 and 120°: experimental and thermal model results.

obtained gamma-ray angular distribution is in good agreement with the experimental results as shown in Figure IV-16.

The best value of the parameter β, 0.10, is smaller than the experimental value 0.14 which we found by transforming both the singles proton spectra and the spectra of protons in coincidence with gamma rays in a frame were the distribution is isotropic. The high value of T needed to fit the proton spectra could be justified since it represents the "temperature" of the proton source at a very early stage. Further interactions of the protons with matter after the first stage, should make the exponential slope steeper and might reproduce the lower experimental values of T.

With these limitations in mind, we went ahead and calculated the ratios. Figure IV-17 shows the ratio calculated as a function of proton energy for protons emitted in a solid angle equivalent to the sum of the solid angles covered by the four most forward charged particles detectors. The low probability of producing an energetic gamma ray (both the neutron and the proton have to be picked from the high-energy tail of the exponential spectra) increased dramatically the number of collisions needed to obtain adequate statistics to calculate a ratio as a function of gamma-ray energy. Due to the enormous amount of computer time needed, we were not able to obtain enough counts to establish the behavior of the ratio as a function of gamma-ray energy for proton energies above 30 MeV in the moving frame as in the experimental result. Figure IV-18 shows the ratio as a function of gamma-ray energy for proton energies above 20 MeV in the laboratory. In Figure IV-19 and IV-20 the ratio is studied as a function of proton angle for gamma rays detected at 60° (D1) and for gamma rays detected at 120° (D2). The

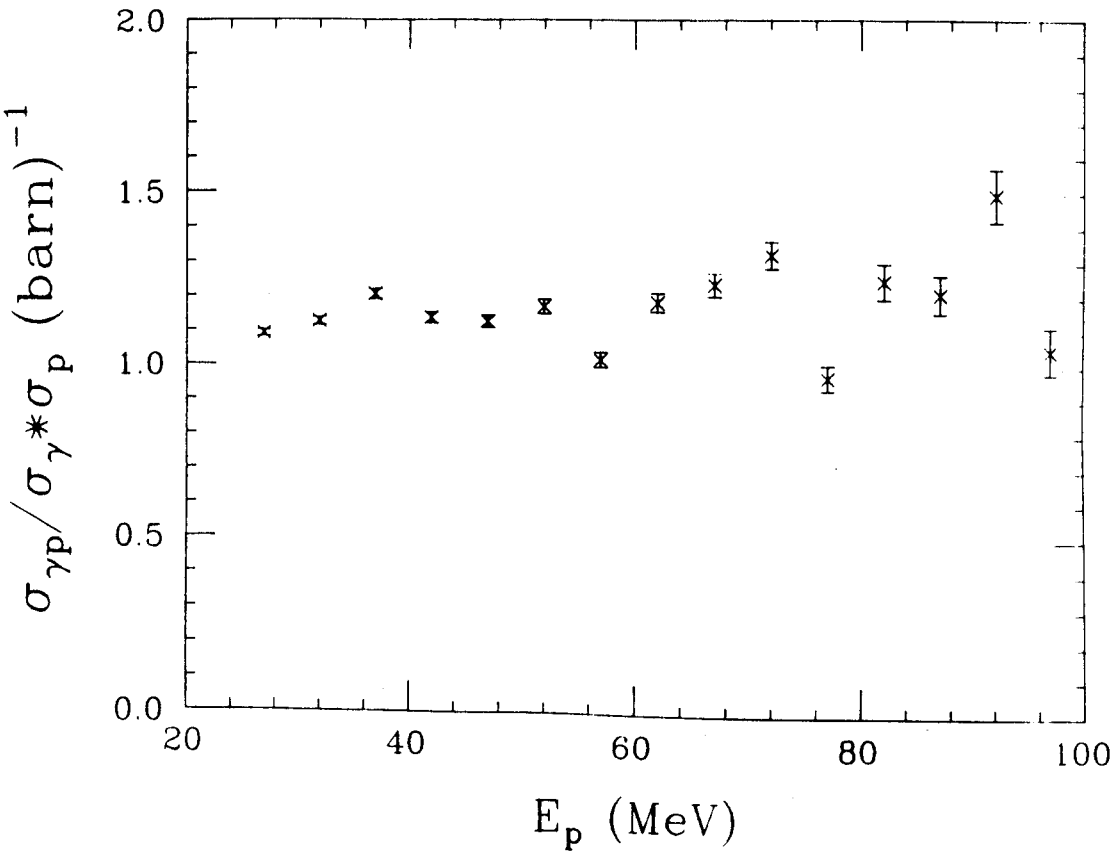

Figure IV-17 Ratio versus E_p for $30 < \theta_p < 70°$ in the thermal model.

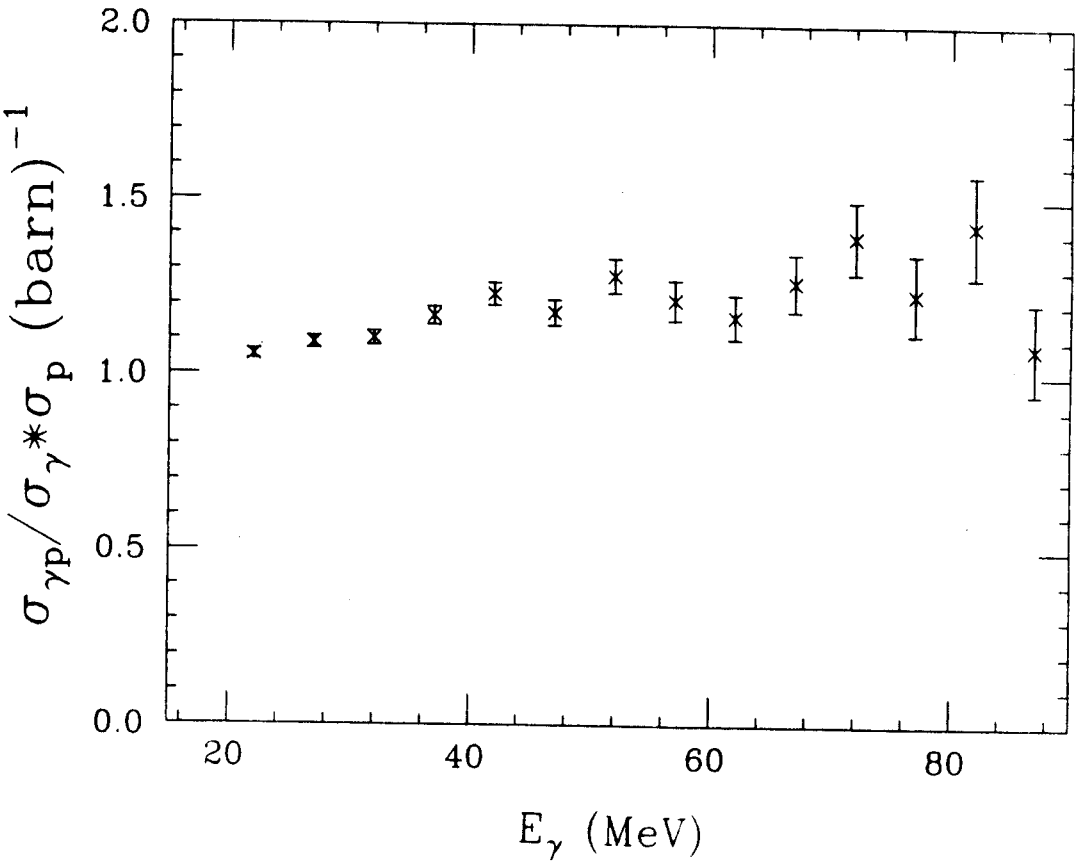

Figure IV-18 Ratio versus E_γ for E_p> 20 MeV in the lab (thermal model).

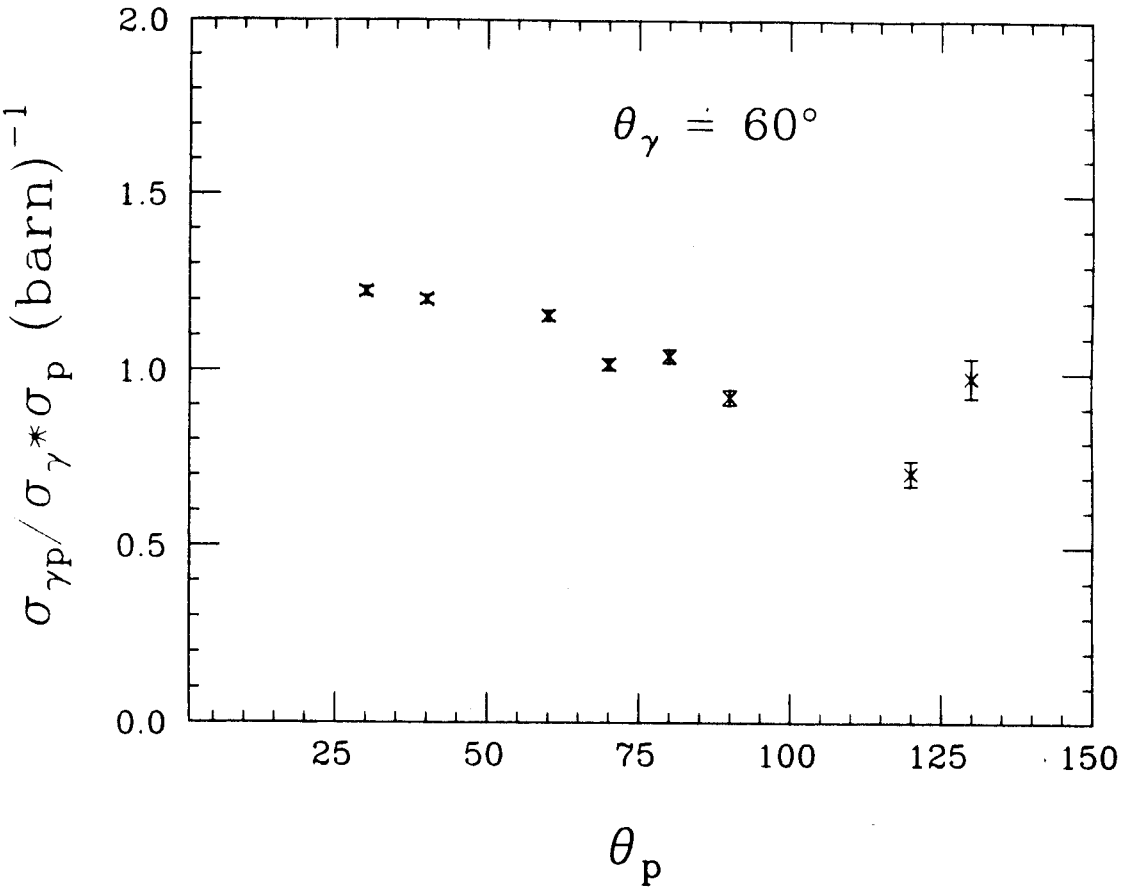

Figure IV-19 Ratio versus Θ_p for gamma rays at 60° in the thermal model

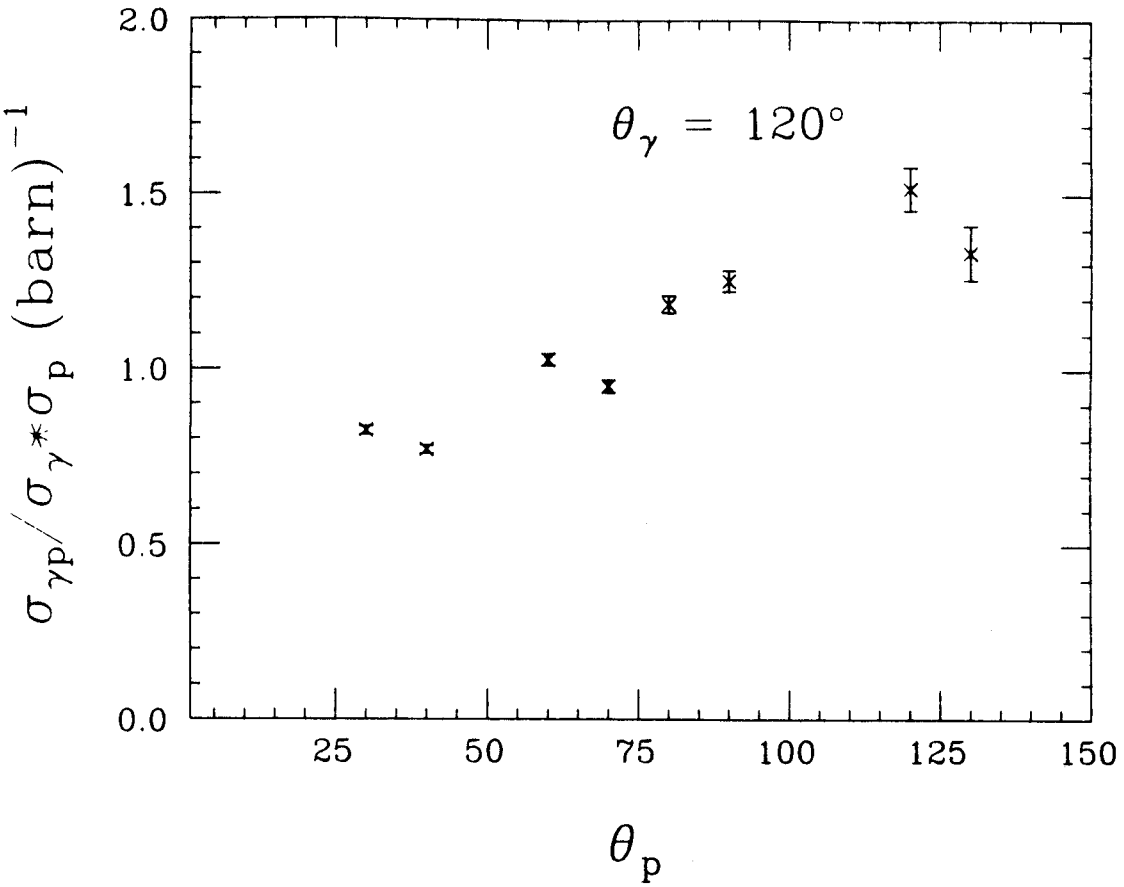

Figure IV-20 Ratio versus Θ_p for gamma rays at 120° in the thermal model.

features of these two angular distributions are due to the strong correlation between the directions of the gamma ray and the proton in in the denominator $(1 - q \cdot \beta_f)$ of the equation II-2 used to represent the gamma-ray emission probability. If θ,ϕ and θ',ϕ' are used to indicate respectively the gamma ray direction and the proton direction, then the denominator can be rewritten as

IV-18 $$1 + \beta[\sin\theta\sin\theta'\cos(\phi-\phi') + \cos\theta\cos\theta']$$

After averaging over ϕ and ϕ'(this was done with the results of the simulations to improve the statistics) it becomes

IV-19 $$1 + \beta\cos\theta\cos\theta' \quad \text{or for } \theta=60° \quad 1 + 0.87\beta\cos\theta'$$
$$\theta=120° \quad 1 - 0.87\beta\cos\theta'$$

The monotonic increase of the function $\cos\theta$ in the $0,\pi$ range explains qualitatively the behavior of the angular distributions in Figures IV-19 and 20.

The different behavior of the angular distributions obtained with the n-p simulation is probably due the smaller amount of energy available in the collision and to the presence of Pauli blocking.

C. CORRELATED AND UNCORRELATED COINCIDENCE

A fundamental problem in any coincidence experiment lies in being able to distinguish between coincidences of particles produced in the

same event and the so called "accidental coincidences" of particles produced in separate events but detected within the same experimental time-acceptance window. In our coincidence experiment the "accidental" rate was determined by measuring the number of coincidences in adjacent cyclotron rf bursts and it was found to be about 20% of the total coincidence rate.

To connect the results of the two Monte Carlo simulation to the experimental results in the following we will call a "correlated coincidence" the coincidence between a gamma ray and the proton that produced it and an "uncorrelated coincidence" the coincidence between a gamma ray and one of the protons produced in the same reaction but not responsible for the photon emission.

While is extremely unlikely that two gamma rays might be produced in the same reaction since the cross section is of the order of 1 mbarn, the production of more than one proton should be investigated. No experimental results regarding the proton multiplicity for beam energies close to 40 MeV/n, are presently available. Lacking a direct experimental result, we used the following procedure in the attempt to estimate the mean proton multiplicity. With our n-p bremsstrahlung simulation program we can find the number of protons emitted in the solid angle $\Delta\Omega$ for each energy interval ΔE for a reaction with a beam energy of 40 MeV/n. The double differential cross-section can be written as

$$\text{IV-20} \qquad \frac{d^2\sigma}{dE\, d\Omega} = \frac{\sigma_{geo}}{\Delta E \;\; \Delta\Omega} \frac{n(\Delta E, \Delta\Omega)}{N} \cdot m$$

IV-22 $$P_{\gamma p} = P_\gamma P_p \quad \text{or} \quad \frac{P_{\gamma p}}{P_\gamma \; P_p} = 1$$

The ratio of the coincidence cross section to the product of the singles cross sections, if multiplied by the geometrical cross section, represents the ratio of probabilities as in equation IV-22. If we add the contribution of the uncorrelated coincidences to the results of the n-p bremsstrahlung (equation IV-23) or to the results of the thermal simulation (equation IV-24) the obtained quantities can be directly compared to the experimental results.

IV-23 $$R_{n-p} \cdot \frac{1}{4} + \frac{3}{4\,\sigma_{geo}}$$

IV-24 $$R_{th} \cdot \frac{1}{4} + \frac{3}{4\,\sigma_{geo}}$$

Figures IV-22 through IV-25 show how the addition of the uncorrelated-coincidence contribution changes the results obtained with the two models. Both sets of results are now very close to the experimental values, but the ratios obtained with the n-p bremsstrahlung are still characterized by a small slope while the ratios obtained with thermal model are flatter, much like the experimental results. A higher mean proton multiplicity would decrease the slope of the n-p results but would also increase the absolute value of the ratios.

where $\sigma_{geo} = \pi[1.2 \cdot (A_{Zn}^{1/3} + A_N^{1/3})]^2$ fm^2 is the geometrical cross-section, m is the average proton multiplicity and N is the number of collisions studied. A comparison between the cross-section in equation IV-20 and the experimental double differential cross-section at 90° allows the determination of m (Figure IV-21). The ratio of the experimental cross section to the cross section in equation IV-18 gives a value of m equal to 3.55. The same procedure applied to the thermal model results gave a value for m of 3.10.

As a second method to estimate the mean proton multiplicity we considered that the proton cross-section σ_p can be written as

IV-21 $$\sigma_p = \sigma_{geo} \cdot m.$$

We parametrized our experimental proton double differential cross section at 90° with a function of the form $Ae^{-\beta E}$ where A and β are parameters and E is the energy. Integrating this function between 0 and infinity and multiplying it by 4π gives a rough value of σ_p The value of m obtained with this method was 4.8.

From the above estimates, approximately three fourths of our experimental coincidences would be due to uncorrelated coincidences. For an uncorrelated coincidence, the probability of observing a gamma ray in coincidence with a proton is simply the product between the probability of observing a gamma ray and the probability of observing a proton as in equation IV-22

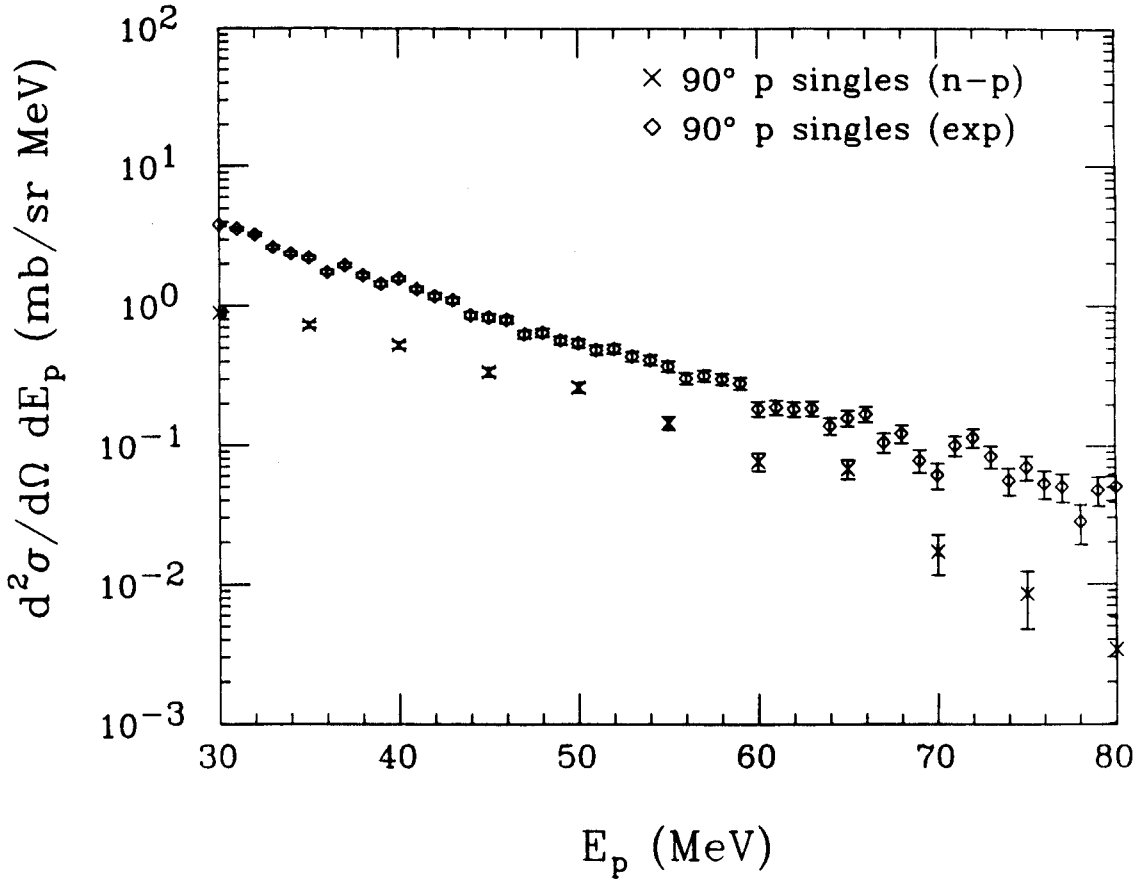

Figure IV-21 Comparison between the experimental and the n-p model results for the determination of the mean proton multiplicity m.

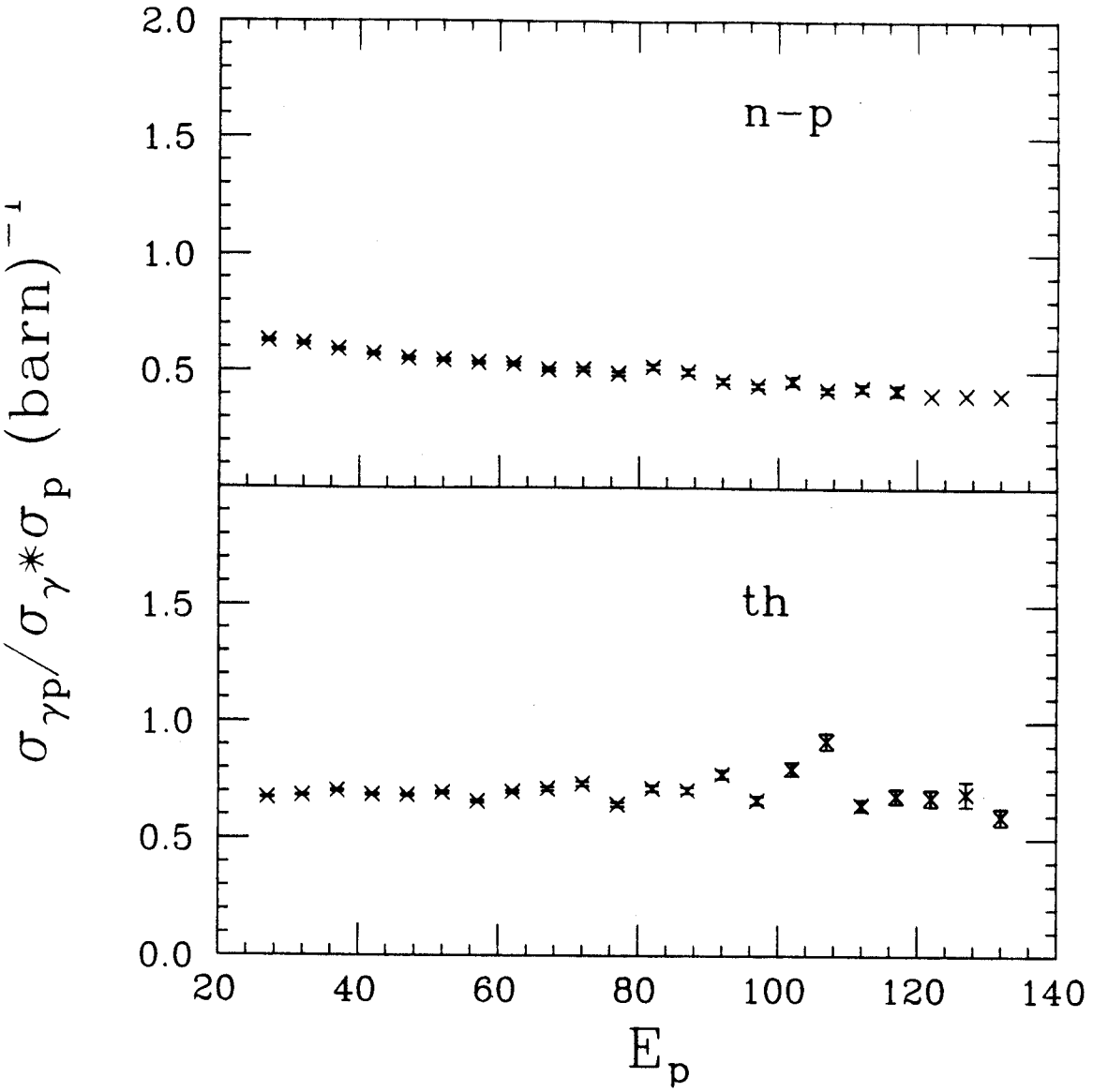

Figure IV-22 Ratio versus E_p in the n-p and in the thermal model after the corrections for the uncorrelated coincidences.

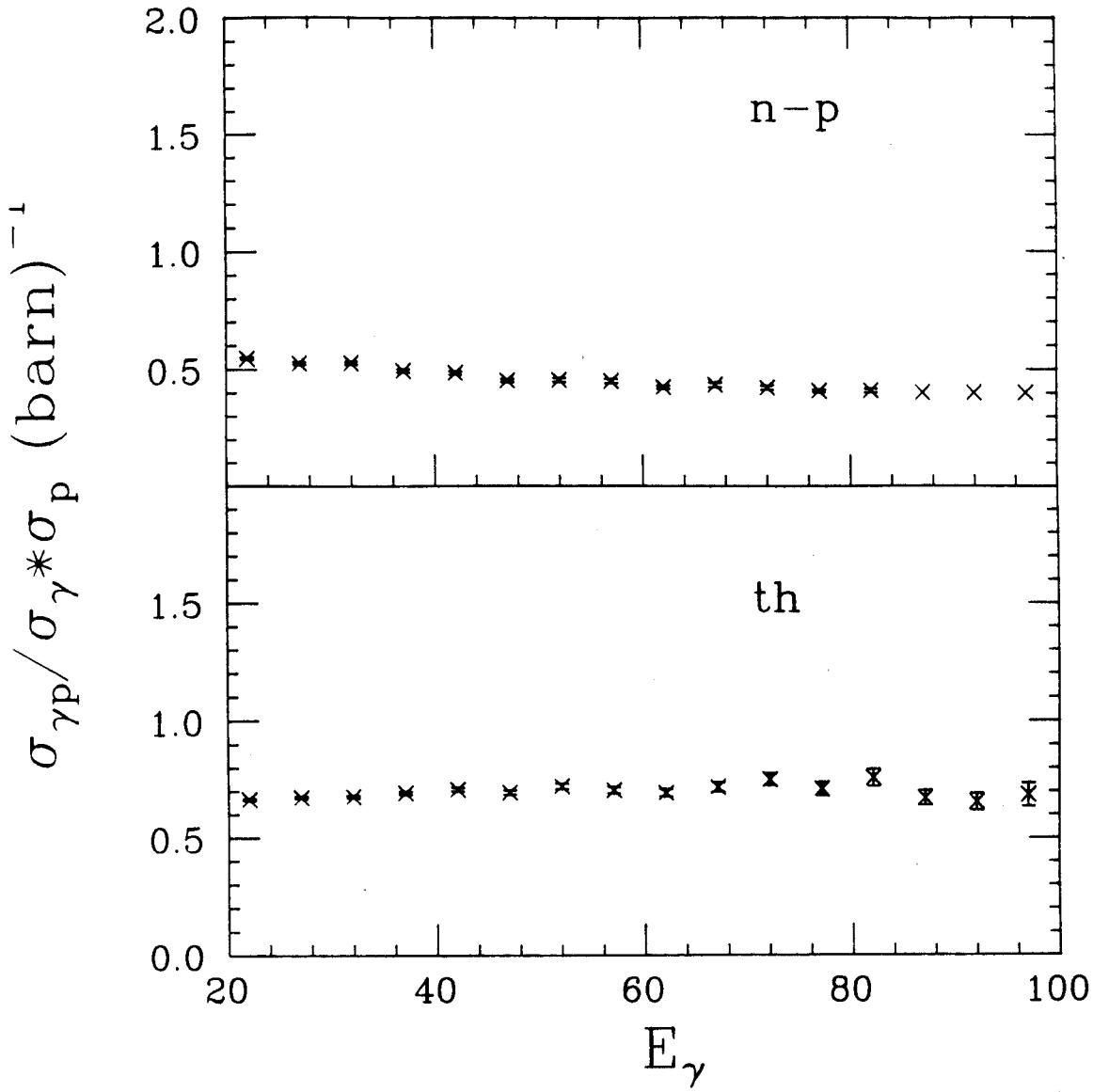

Figure IV-23 Ratio versus E_γ in the n-p and in the thermal model after the corrections for the uncorrelated coincidences.

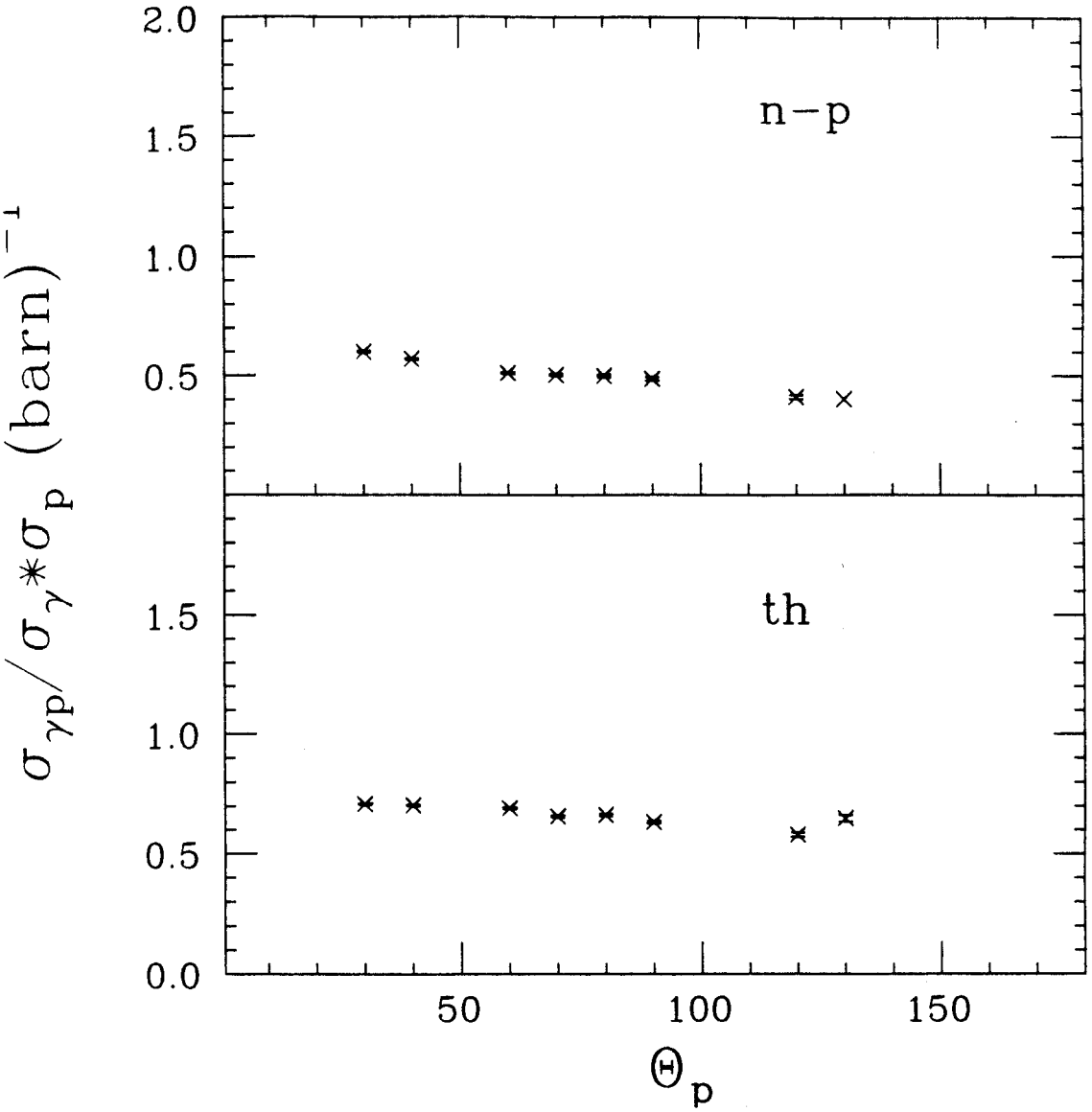

Figure IV-24 Ratio versus θ_p for gamma rays at 60° in the n-p and in the thermal model after the corrections for the uncorrelated coincidences.

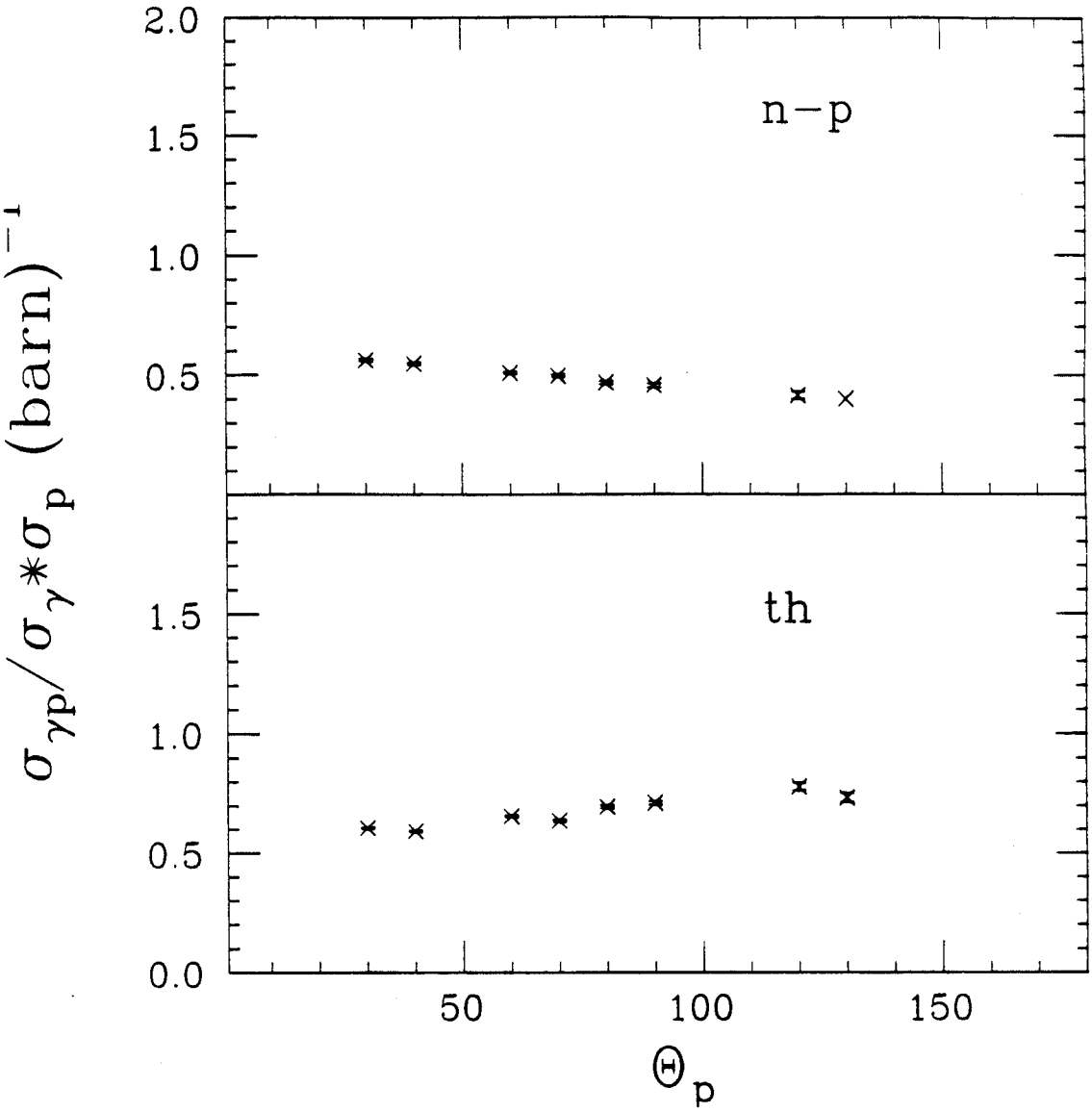

Figure IV-25 Ratio versus θ_p for gamma rays at 120° in the n-p and in the thermal model after the corrections for the uncorrelated coincidences.

SUMMARY AND CONCLUSIONS

The energy spectra of the high-energy gamma rays produced in the reactions N + C, Zn and Pb at 20, 30 and 40 MeV/n decrease exponentially with energy. The double differential cross sections were parametrized for $E_\gamma > 35$ MeV with a function of the form $Ae^{-E/\tau}$. The value of the parameter τ is almost independent of the target used and ranges from 8 to 14 MeV for beam energies between 20 and 40 MeV/n.

The angular distributions are all slightly forward peaked. The ratio $\sigma(30°)/\sigma(150°)$ at 40 MeV/n is equal to 2.35 for Pb, 2.28 for Zn and 3.14 for C. An isotropic emission from a moving source was considered and the gamma-ray emission was found to be nearly isotropic in a frame moving with velocity close to the nucleon-nucleon center of mass velocity.

The total cross section at 90° slowly increases with target mass and beam energy from 0.02 mb for N + C at 20 MeV/n to 0.64 mb for N + Pb at 40 MeV/n.

The theories proposed to explain the origin of the photons in this energy range, such as first collision n-p bremsstrahlung and statistical emission, all do a reasonably good job in reproducing the experimental features. In order to provide a testing ground for these theories we studied the coincidences between high-energy gamma rays and light charged particles (Z=1) in the reaction N + Zn at 40 MeV/n.

A qualitative comparison between inclusive proton spectra and exclusive spectra of protons in coincidence with gamma rays did not show any marked difference. The same kind of result was obtained by comparing the gamma-ray singles spectrum with the spectra of gamma rays

in coincidence with protons at several proton angles. We then studied the ratio of the gamma ray - proton cross section to the product of the proton and gamma-ray cross sections as a function of proton angle, gamma-ray angle (only 60° and 120°), gamma-ray energy and proton energy. The value of the ratio was found to be independent of all of the above variables, within the experimental uncertainty, with an approximate value of 0.6 barn^{-1}. Multiplying this value by the geometrical cross section, σ_{geo}=1.86 barn, produces a value of 1.12. The ratios are then just 12% above the value of 1 characteristic of coincidence probability of independent events.

Two Monte Carlo codes were written to simulate the gamma-ray production as a product of first chance n-p collision and as a product of secondary collisions respectively. To connect the simulation results to the experimental results we investigated the possibility of "uncorrelated coincidences", i.e. coincidences between a gamma ray and one of the protons produced in the same reaction but not responsible for the photon emission. We estimated the mean proton multiplicity at 40 MeV to be about 4 per collision. With the assumption that 3/4 of the experimental coincidences are "uncorrelated" we were able to obtain simulation results suitable for comparison with the experimental data.

The most striking characteristic of the ratios obtained with the first collision model is a slow decrease in energy. This behaviour is expected to be a consequence of the limited amount of energy available in the system. A lower value of the mean proton multiplicity would make this effect more visible and a coincidence experiment using light systems might help to completely rule out first chance collision as the main mechanism in the gamma-ray production.

While the results obtained with the second model appear to be in overall better agreement with the experimental results, it should also be pointed out that, due to the enormous amount of computer time needed, the conditions applied to obtain them are different from the ones used both in the analysis of the experimental results and in the first chance simulation.

The charged-particle multiplicity associated with the emission of a gamma ray and the charged-particle multiplicity associated with the emission of a charged particle were studied to obtain information about the impact-parameter dependence of the gamma-ray production. The gamma - charged particle multiplicity M=1 (a Z=1 charged particle in coincidence with a gamma ray) was found to be only 10% higher than the charged particle multiplicity M=2 (a Z=1 particle in coincidence with a Z=1 charged particle). Higher multiplicities could not be compared due both to an insufficient statistics in the gamma - charged particle multiplicity and to a large uncertainty in the higher orders of the charged particle-charged particle multiplicity. On the limited basis of the multiplicity result, the gamma ray and the light charged particle production appear to share a very similar impact parameter dependence. A similar experiment where the gamma-ray detector can be substituted with a phoswich and the scale down factors are removed could provide a more precise comparison of the two multiplicities and extend it to higher orders.

LIST OF REFERENCES

A

[Al 86] N. Alamanos, P. Braun-Munzinger, R. F. Freifelder, P. Paul, J. Stachel, T.C. Awes, R. L. Ferguson, F. E. Obenshain, F. Plasil, and G. R. Young, Phys. Lett. 173 B, 392 (1986).

B

[Ba 86a] W. Bauer, W. Cassing, U. Mosel, and M. Tohyama, Nucl. Phys. A456, 159 (1986).

[Ba 86b] W. Bauer, G. F. Bertsch, W. Cassing, and U. Mosel, Phys. Rev C 34, 2127 (1986).

[Ba 87] W. Bauer, T. S. Biro, W. Cassing, U. Mosel, K. Niita, A. L. De Pauli, G. F. Bertsch preprint.

[Be 81] G. F. Bertsch and J. Cugnon, Phys. Rev. C 24, 2514 (1981).

[Be 85a] K. Beard, W. Benenson, C. Block, E. Kashy, J. Stevenson, D. J. Morrissey, J. van der Plicht, B. Sherrill, and J. S. Winfield, Phys. Rev. C 32, 1111 (1985).

[Be 85b] K. Beard Ph. D. thesis, unpublished.

[Be 87] R. Bertholet, M. Kwato Njock, M. Maurel, E. Monnard, H. Nifenecker, P. Perrin, J. A. Pinston, F. Schussler, D. Barneoud, submitted to Nuc. Phys.

[Bl 81] Blann, Phys. Rev. C 23, 205 (1981).

[Bo 87] A. Bonasera, L.Csernai, and B. Schurmann, preprint (1987).

[Bo 87] A. Bonasera, M. di Toro and C. Gregoire, preprint.

[Br 73] V. R. Brown and J. Franklin, Phys. Rev. C 8, 1706 (1973).

[Bu 82] M. P. Budiansky, S. P. Ahlen, G. Tarle', and P. B. Price, Phys. Rev. Lett. 49, 361 (1982).

C

[Cs 84] L. Csernai, Magyar Fizikai Folyoirat 32, 231 (1984).

E

[Eg 66] J. A. Edgington and B. Rose, Nucl. Phys 89, 523 (1966).

[Ei 60] R. M. Eisberg, D. R. Yennie and D. H. Wilkinson, Nucl. Phys. 18, 338 (1960).

F

[Fo 87] D. Fox, D. A. Cebra, Z. M. Koenig, P. Ugorowski, and G. D. Westfall, Phys. Rev. C 33, 1540 (1987).

G

[Gr 84] E. Grosse LBL-16281.

[Gr 86] E. Grosse, P.Grimm, H. Heckwolf, W. F. J. Mueller, H. Noll, A. Oskarson, H.Stelzer, and W. Roesch, Europhysics Lett. 2, 9 (1986).

[Gu 87] C. Gossett, Fourth Gull Lake Nuclear Physics Conference.

H

[He 87] N. Herrmann, R. Bock, H. Emling, R. Freifelder, A. Gobbi, E. Grosse, K. D. Hildenbrand, R. Kulessa, T. Matulewicz, F. Rami, R. S. Simon, H. Stelzer, J. Wessels, P. R. Maurenzig, A. Olmi, A. A. Stefanini, W. Kuhn, V. Metag, R. Novotny, M. Gnirs, D. Pelte, P. Braun-Munzinger, L. G. Moretto, GSI preprint.

[Hi 87] R. Hingmann, W. Kuhn, V. Metag, R. Muhlahans, R. Novotny, A. Ruckelshausen, W. Cssing, B. Haas, J. P. Vivien, A. Boullay, H. Delagrange, H. Doubre, C. Gregoire, Y. Schutz, Phys. Rev. Lett. 58, 759 (1987).

K

[Ka 77] J. I. Kapusta, Phys. Rev C 15, 1580 (1977).

[Kw 86] M. Kwato Njock, Phys. Lett. 175B, 125 (1986).

[Ko 85] C. M. Ko, G. Bertsch, and J. Aichelin, Phys. Rev. C31, 2324 (1985).

N

[Ni 85] H. Nifenecker and J. P. Bondorf, Nucl. Phys. A 442, 478 (1985).

[Na 86] K. Nakayama and G. F. Bertsch, Phys. Rev. C 34, 2190 (1986).

[Ne 85] W. R. Nelson, Hideo Hirayama, and D. W. O. Rogers, SLAC-265 UC-32 (1985).

[Ne 87] D. Neuhauser and S. E. Koonin, Nucl. Phys. A 462, 163 (1987).

R

[Re 87a] A. Remington, M. Blann, G. F. Bertsch, Phys. Rev. C 35, 1720 (1987).

[Re 87b] A. Remington, M. Blann, G. F. Bertsch preprint.

S

[St 86] J. Stevenson, K. B. Beard, W. Benenson, J. Clayton, E. Kasky. A. Lampis, D. J. Morrissey, M. Samuel, R. J. Smith, C. L. Tam, and J. S. Winfield. Phys. Rew. Lett. 57, 555 (1986).

[St 88] Stevenson et al., in preparation.

V

[Va 85] D. Vasak, Berndt Muller and Walter Greiner,J. Phys. G: Nucl. Phys. 11, 1309 (1985).

W

[We 76] G. D. Westfall, J. Gosset, P.J. Johansen, A. M. Poskanzer, W. G. Meyer, H. H. Gutbrod, A. Sandoval, and R.Stock, Phys. Rev. Lett. 37, 1202 (1976).